

University of Warwick institutional repository: <http://go.warwick.ac.uk/wrap>

A Thesis Submitted for the Degree of PhD at the University of Warwick

<http://go.warwick.ac.uk/wrap/58204>

This thesis is made available online and is protected by original copyright.

Please scroll down to view the document itself.

Please refer to the repository record for this item for information to help you to cite it. Our policy information is available from the repository home page.

Library Declaration and Deposit Agreement

1. STUDENT DETAILS

Please complete the following:

Full name: Andrew Neil Ferguson

University ID number: 0303921

2. THESIS DEPOSIT

2.1 I understand that under my registration at the University, I am required to deposit my thesis with the University in BOTH hard copy and in digital format. The digital version should normally be saved as a single pdf file.

2.2 The hard copy will be housed in the University Library. The digital version will be deposited in the University's Institutional Repository (WRAP). Unless otherwise indicated (see 2.3 below) this will be made openly accessible on the Internet and will be supplied to the British Library to be made available online via its Electronic Theses Online Service (EThOS) service.

[At present, theses submitted for a Master's degree by Research (MA, MSc, LLM, MS or MMedSci) are not being deposited in WRAP and not being made available via EThOS. This may change in future.]

2.3 In exceptional circumstances, the Chair of the Board of Graduate Studies may grant permission for an embargo to be placed on public access to the hard copy thesis for a limited period. It is also possible to apply separately for an embargo on the digital version. (Further information is available in the *Guide to Examinations for Higher Degrees by Research*.)

2.4 *If you are depositing a thesis for a Master's degree by Research, please complete section (a) below. For all other research degrees, please complete both sections (a) and (b) below:*

(a) Hard Copy

I hereby deposit a hard copy of my thesis in the University Library to be made publicly available to readers immediately.

I agree that my thesis may be photocopied. YES

(b) Digital Copy

I hereby deposit a digital copy of my thesis to be held in WRAP and made available via EThOS.

Please choose one of the following options:

My thesis can be made publicly available online. YES

3. GRANTING OF NON-EXCLUSIVE RIGHTS

Whether I deposit my Work personally or through an assistant or other agent, I agree to the following:

Rights granted to the University of Warwick and the British Library and the user of the thesis through this agreement are non-exclusive. I retain all rights in the thesis in its present version or future versions. I agree that the institutional repository administrators and the British Library or their agents may, without changing content, digitise and migrate the thesis to any medium or format for the purpose of future preservation and accessibility.

4. DECLARATIONS

(a) I DECLARE THAT:

- I am the author and owner of the copyright in the thesis and/or I have the authority of the authors and owners of the copyright in the thesis to make this agreement. Reproduction of any part of this thesis for teaching or in academic or other forms of publication is subject to the normal limitations on the use of copyrighted materials and to the proper and full acknowledgement of its source.
- The digital version of the thesis I am supplying is the same version as the final, hard-bound copy submitted in completion of my degree, once any minor corrections have been completed.
- I have exercised reasonable care to ensure that the thesis is original, and does not to the best of my knowledge break any UK law or other Intellectual Property Right, or contain any confidential material.
- I understand that, through the medium of the Internet, files will be available to automated agents, and may be searched and copied by, for example, text mining and plagiarism detection software.

(b) IF I HAVE AGREED (in Section 2 above) TO MAKE MY THESIS PUBLICLY AVAILABLE DIGITALLY, I ALSO DECLARE THAT:

- I grant the University of Warwick and the British Library a licence to make available on the Internet the thesis in digitised format through the Institutional Repository and through the British Library via the EThOS service.
- If my thesis does include any substantial subsidiary material owned by third-party copyright holders, I have sought and obtained permission to include it in any version of my thesis available in digital format and that this permission encompasses the rights that I have granted to the University of Warwick and to the British Library.

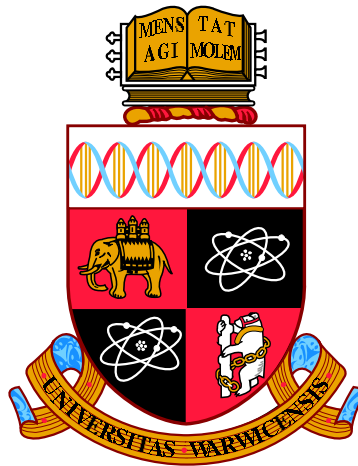
5. LEGAL INFRINGEMENTS

I understand that neither the University of Warwick nor the British Library have any obligation to take legal action on behalf of myself, or other rights holders, in the event of infringement of intellectual property rights, breach of contract or of any other right, in the thesis.

Please sign this agreement and return it to the Graduate School Office when you submit your thesis.

Student's signature: Andrew Neil Ferguson

Date: 25th September 2013



Production Mechanisms of Intense Events

by

Andrew Neil Ferguson

Thesis

Submitted to the University of Warwick

for the degree of

Master of Philosophy

School of Engineering

October 2012

THE UNIVERSITY OF
WARWICK

Contents

List of Tables	iv
List of Figures	v
Acknowledgments	xii
Declarations	xiii
Abstract	xiv
Nomenclature	xv
Chapter 1 Introduction	1
1.1 Production Mechanisms of Intense Events	1
Chapter 2 Background and Motivation	4
2.1 Introduction	4
2.2 Euler Equations	5
2.3 The Navier Stokes Equations	5
2.3.1 Strain	6
2.3.2 Vorticity Equations	6
2.4 Vieillefosse	7
2.5 Mathematical Preliminaries	8
2.5.1 Cayley-Hamilton Theorem	9
2.6 Moments	10
2.7 Alternative Consideration	11
2.8 The Restricted Euler Model	12
2.9 Ashurst	14

2.10	Cantwell	15
2.11	Deriving the RQ equations	17
2.12	Closure problem	19
Chapter 3	Turbulence Simulations	27
3.1	Introduction	27
3.2	Turbulence Preliminaries	27
3.3	Direct Numerical Simulation	28
3.4	Navier Stokes DNS	29
3.4.1	CFL	31
3.4.2	Velocity-Vorticity form of NSE	31
3.5	Fourier Transformation	32
3.6	Pseudo-spectral Method	33
Chapter 4	Visualisation	34
4.1	Computational Data	34
4.1.1	Energy Spectra	35
4.2	Energy Transfer	36
4.2.1	Global Time Evolution Diagnostics	38
4.2.2	Maximum of Vorticity	40
4.2.3	Dissipation	40
4.2.4	Reynolds Number	42
4.3	Flow Visualisation	42
4.4	Summary	46
Chapter 5	Validation	52
5.1	RE Validation One	52
5.2	RE Validation Two	53
5.3	Probability Distributions	53
5.4	R-Q Phase Space	56
5.4.1	Conditioned Distributions	56
5.5	Summary	60
Chapter 6	Pressure Hessian	67
6.1	Calculating \mathbf{p} and \mathbf{P}	69

6.2	Discussion	69
6.2.1	Isotropy and Pressure Decomposition	70
6.2.2	Evolution Equation Derivation	71
6.3	Conditional Mean Trajectories	72
6.4	Underlying Physics	75
6.5	Summary	83
Chapter 7 3D Phase Space		84
7.1	Decomposing R	85
7.1.1	Distribution	86
7.2	(Q, R_S, R_ω) Evolution	87
7.2.1	\mathbf{Q} Evolution	87
7.2.2	\mathbf{R}_ω Evolution	93
7.2.3	\mathbf{R}_S Evolution	94
7.3	Pressure Hessian	94
7.4	Summary	107
Chapter 8 Conclusions		110
8.1	Evidence for a Model	112
8.2	Role of the Intense Events	112
8.3	Further Work	114

List of Tables

4.1	This is a table of key quantities taken from calculations A, B and C.	35
7.1	This table compares the values of r , z_r and the 95% confidence interval for r at key times for runs B and C.	95
7.2	The values of β_Q , 95% Confidence Interval and Hypothesis Test result for figures 7.4 and 7.5	95
7.3	This table compares the values of r , β_Q , β'_Q and β''_Q for run B.	102
7.4	A comparison between β_Q and β_Q^{Scaled} for run B.	102
7.5	Correlation coefficients for runs B and C for R_ω at key times. r is the standard correlation coefficient, r_- is the correlation coefficient in the region $\frac{dR_\omega}{dt} _{Restricted} < 0$ and r_+ is the correlation coefficient in the region $\frac{dR_\omega}{dt} _{Restricted} \geq 0$	102
7.6	A comparison between β_{R_ω} and $\beta_{R_\omega}^{Scaled}$ for run B.	104
7.7	This table compares the values of r , $\beta_{R_\omega}^+$, $\beta_{R_\omega}'^+$ for run B. . . .	105

List of Figures

2.1	Trajectories of the second(\mathbf{Q}) and third(\mathbf{R}) invariants of the velocity gradient tensor \mathbf{A}	19
2.2	An illustration of the deformation map between the initial configuration and deformed configuration of a material body. . . .	20
2.3	This figure taken from A first course in continuum mechanics [21] which illustrates the role and action of the Cauchy Green Tensor on the reference and deformed configurations.	21
4.1	Three-dimensional kinetic energy spectra for simulation A, normalised by the Kolmogorov microscale and multiplied by $k^{5/3}$, $R_\lambda = 256$ at $t = 0$	36
4.2	Three-dimensional kinetic energy spectra for simulation B, normalised by the Kolmogorov microscale and multiplied by $k^{5/3}$, $R_\lambda = 1018$ at $t = 0$	37
4.3	Three-dimensional kinetic energy spectra for simulation C, normalised by the Kolmogorov microscale and multiplied by $k^{5/3}$, $R_\lambda = 256$ at $t = 0$	37
4.4	Transfer function of three dimensional turbulence as calculated for calculation A(top), B(middle) and C(bottom) over $t=0.1$ to $t=0.9$ in 0.1 increments.	39
4.5	The time dependence of maximum vorticity $ \boldsymbol{\omega} _\infty$ growth for simulations A, B and C.	40
4.6	The dissipation growth for simulations A, B and C.	41
4.7	The Skewness factor evolution is plotted for simulations A, B and C. The expected behaviour of $S_k \rightarrow 0.5$ is observed once the turbulence is fully developed [31] and [14].	42

4.8	The evolution of the Taylor Reynolds number Re_λ for simulations A, B and C across all times.	43
4.9	This is the Vector field of simulation B at $t=0.3$, here we considered a 5000 point subset of the entire flow field, the velocities range from 12.85(red) to 0 (blue). The vectors are scaled by magnitude. On its own the velocity field does not provide any noteworthy features of the flow other than the scale of velocities contained within the flow.	44
4.10	The ratio between the spatial and temporal discretization should be in approximate balance to reduce the likely hood of numerical artefact's populating the flow. The reduction in the Kolmogorov microscale η is plotted (left) and the reduction time stepping Δt is plotted (right)	44
4.11	This figure considers the isosurfaces of vorticity from simulation B at $t=0.8$, $R_\lambda = 380$. The vorticity is conditioned on regions of low (green $ \omega \approx 50$), medium (light blue $ \omega \approx 135$) and high (blue $ \omega \approx 370$) vorticity with the lower isosurfaces partially transparent to see the interior flow.	47
4.12	A slice through the isosurfaces of vorticity from simulation B, $R_\lambda = 380$ at $t = 0.8$. The vorticity is conditioned on regions of low(black $ \omega \approx 20$), medium (blue $ \omega \approx 20$) and high (pale blue $ \omega \approx 130$) vorticity with the regions of high vorticity held within the intermediate structures. For clarity the velocity field have been overlaid with values ranging from 15 (red) to 0 (blue).	48
4.13	Here we have taken a slice through the volume of vorticity isosurfaces at $t=0.9$ from simulation B (left), here the vorticity is conditioned on regions of low (green $ \omega \approx 50$), medium (light blue $ \omega \approx 135$) and high(blue $ \omega \approx 370$) vorticity. The velocity field was then overlaid using a single colour - red (right) . . .	49

4.14	The left image shows the vorticity streamlines at $t=0.6$ from simulation B, the vorticity ranges from 332.5(red) to 0(blue). The right image is a slice through the vorticity isosurfaces with the vorticity streamlines overlaid, in this subsection the vorticity magnitude(red) ranges from 207 to 0 and the streamlines range from 102(red) to 0(blue).	50
4.15	The left image shows the isosurfaces of the strain at $t=0.4$, the strain is divided into three regions orange, yellow and pale yellow with midvalues 47.67, 31.79 and 15.91 respectively. The right image looks at the interaction between vorticity(blue) and the strain(orange). The vorticity has been divided into three regions with midpoints 174.5 (blue), 116.4(light blue) and 58.26 (pale blue), similarly the strain has regions 52.11(red), 34.76(orange) and 17.41(yellow).	50
4.16	This is a representation of the isosurfaces of the enstrophy (blue) and dissipation (red) production terms.	51
5.1	Confirming the constraint that R and Q should be zero over the entire flow. Other moments are included for completeness. . .	54
5.2	In all cases the x axis is time. Upper left: close-up of Figure 5.1 showing the linear approach to zero of these inverses. $\alpha^{-1} = \omega^2/R_\omega$, $(-R_S/3)^{-1/3}$, $(-R_\omega/4)^{-1/3}$, $(S^2)^{-1/2}$ and $(\omega^2)^{-1/2}$. Upper right: Normalised components: $\alpha_N^{-1} = \omega^2/R_\omega$, β and S_N^3 using equation (5.3). Lower left: ratio between the two second ω^2/S^2 and two third order moments, $-R_\omega/R_S$ respectively. As expected, the second order moments approach 2 as the singular time is reached and the third order moments approach $\frac{4}{3}$. Lower right: The ratio between the moments is considered again and this time we include a term analogous to Q, $(2 - \omega^2/S^2)$. The behaviour seen is exactly as expected with the two ratios $(-\omega^2/S^2 + 2, -R_\omega/R_S - 4/3)$ and the new term $(2 - \omega^2/S^2)^{1.5}$ approaching zero in the singular limit.	55

5.3	Typical probability distributions of the normalised triple strain S_N^3 in the full domain and conditioned on the region of maximum vorticity, provided by R M Kerr.	56
5.4	This is the probability distribution of both β and S_N , the intersection is of interest as it allows us to consider the balance between the third order moments R_ω and R_S , provided by R M Kerr.	57
5.5	Typical probability distributions of the normalised β including β conditioned on the region of maximum vorticity, provided by R M Kerr.	57
5.6	The typical R-Q teardrop characterised by R and Q, without breaking down the terms, from $t = 0.5$ from simulation A . . .	58
5.7	RQ sampled by ω^2 in the intervals; [0.4,0.425] (top), [0.5,0.525] (middle), [0.6,0.625] (bottom).	61
5.8	RQ sampled by S^2 in the intervals; [0.4,0.425] (top), [0.5,0.525] (middle), [0.6,0.625] (bottom).	62
5.9	RQ sampled by R_ω in the intervals; [0.4,0.425] (top), [0.5,0.525] (middle), [0.6,0.625] (bottom).	63
5.10	RQ sampled by R_S in the intervals; [0.4,0.425] (top), [0.5,0.525] (middle), [0.6,0.625] (bottom).	64
5.11	RQ sampled by α in the intervals; [0.4,0.425] (top), [0.5,0.525] (middle), [0.6,0.625] (bottom).	65
5.12	RQ sampled by I_4 in the intervals; [0.4,0.425] (top), [0.5,0.525] (middle), [0.6,0.625] (bottom).	66

6.1	A typical restricted Euler (RE) trajectory for reference for all the following figures showing trajectories of points in the R-Q phase space. In this figure the vectors show the strength and direction of the Lagrangian RE time derivatives (6.14) of Lagrangian points in physical space for dataset A at time $t = 0.5$, essentially the same data as used for scatter plots in figures 5.7b, 5.8b, 5.9b, 5.10b, and 5.12b and is included in Figure 6.2. In RE, the dominant path of trajectories is clock-wise about $(R, Q) = (0, 0)$ for $Q > 0$, converging on the Vieillefosse discriminant (6.31) in the lower right quadrant.	76
6.2	R-Q trajectories of Lagrangian points of the second and third invariants of the velocity gradient tensor within the interval $t = [0.0, 0.3]$, from dataset A a) left image is where we have neglected the effects of the deviatoric pressure Hessian, and b) the right image is the full flow.	76
6.3	R-Q trajectories of Lagrangian points of the second and third invariants of the velocity gradient tensor within the interval $t = [0.3, 0.4]$, from dataset A a) left image is where we have neglected the effects of the deviatoric pressure Hessian, and b) the right image is the full flow.	77
6.4	R-Q trajectories of Lagrangian points of the second and third invariants of the velocity gradient tensor within the interval $t = [0.4, 0.5]$, from dataset A a) left image is where we have neglected the effects of the deviatoric pressure Hessian, and b) the right image is the full flow.	77
6.5	R-Q trajectories of Lagrangian points of the second and third invariants of the velocity gradient tensor within the interval $t = [0.5, 0.7]$, from dataset A a) left image is where we have neglected the effects of the deviatoric pressure Hessian, and b) the right image is the full flow.	77
6.6	The left images are taken from dataset B and the right images are taken from dataset C. (Top) $t=0.3$, (Second) $t=0.4$, (third) $t=0.5$ and (last) $t=0.6$	78
6.7	Three-dimensional topologies in the R-Q plane, taken from [47]	79

6.8	Here the interaction region between the strain and vorticity is realised from simulation A at time $t = 0.5$. Here The top image is a visualisation of the total vorticity and strain interaction within the periodic domain, the middle image is the subset of the same domain containing the interaction region. The final image is a refined view with varying levels of opacity for both the strain and vorticity. The vorticity magnitude is divided into three regions; blue $ \omega \approx 152$, light blue $ \omega \approx 102$, pale blue $ \omega \approx 152$. Similarly the strain magnitude is divided into three coloured sections, brown $ \mathbf{S} \approx 47$, red $ \mathbf{S} \approx 31$, orange $ \mathbf{S} \approx 16$. Please note that the ribs are a resolution effect in the graphic caused by only sampling every other point.	82
7.1	Comparison of $\frac{d\mathbf{Q}}{dt} _{Hessian}$ against $\frac{d\mathbf{Q}}{dt} _{Restricted}$	88
7.2	Comparison of $\frac{d\mathbf{R}\omega}{dt} _{Hessian}$ against $\frac{d\mathbf{R}\omega}{dt} _{Restricted}$	88
7.3	Comparison of $\frac{d\mathbf{R}\mathbf{S}}{dt} _{Hessian}$ against $\frac{d\mathbf{R}\mathbf{S}}{dt} _{Restricted}$	95
7.4	The above images compare the relationship between the isotropic assumption for the pressure Hessian and the full pressure Hessian in the evolution equation for the second invariant \mathbf{Q} from Simulation B from $t=0.3$ (top) until $t=0.6$ (bottom).	96
7.5	The above images compare the relationship between the isotropic assumption for the pressure Hessian and the full pressure Hessian in the evolution equation for the second invariant \mathbf{Q} from Simulation C from $t=0.3$ (top) until $t=0.6$ (bottom).	97
7.6	The above images compare the relationship between the isotropic assumption for the pressure Hessian and the full pressure Hessian in the evolution equation for $\mathbf{R}\omega$ from Simulation B from $t=0.3$ (top) until $t=0.6$ (bottom).	98
7.7	The above images compare the relationship between the isotropic assumption for the pressure Hessian and the full pressure Hessian in the evolution equation for $\mathbf{R}\omega$ from Simulation C from $t=0.3$ (top) until $t=0.6$ (bottom).	99

7.8	The above images compare the relationship between the isotropic assumption for the pressure Hessian and the full pressure Hessian in the evolution equation for $\mathbf{R_S}$ from Simulation B from $t=0.3$ (top) until $t=0.6$ (bottom).	100
7.9	The above images compare the relationship between the isotropic assumption for the pressure Hessian and the full pressure Hessian in the evolution equation for $\mathbf{R_S}$ from Simulation C from $t=0.3$ (top) until $t=0.6$ (bottom).	101
7.10	(top) A comparison between run B and run C is made for the value of β_Q . (middle) A 6^{th} order polynomial is fitted to β_Q for run B. (bottom) A 6^{th} order polynomial is fitted to β_Q for run C.	103
7.11	The top plot is Run B at $t = 0.5$, here we compare $\frac{dQ}{dt}(t) _{Restricted}$ and $\frac{dQ}{dt}(t) _{Hessian}$ (top) against $\frac{dQ}{dt}(t) _{Hessian}$ and $\frac{dQ}{dt}(t) _{Scaled}$ (bottom) observing a reduction in the slope of the distribution, that it $\frac{dQ}{dt}(t) _{Scaled}$ closer to $\frac{dQ}{dt}(t) _{Hessian}$	104
7.12	The top plot is Run B at $t = 0.6$, here we compare $\frac{dQ}{dt}(t) _{Restricted}$ and $\frac{dQ}{dt}(t) _{Hessian}$ (top) against $\frac{dQ}{dt}(t) _{Hessian}$ and $\frac{dQ}{dt}(t) _{Scaled}$ (bottom) observing a reduction in the slope of the distribution bringing $\frac{dQ}{dt}(t) _{Scaled}$ closer to $\frac{dQ}{dt}(t) _{Hessian}$	105
7.13	(top) A comparison between run B and run C is made for the value of $\beta_{R_\omega^+}$. (middle) A quadratic is fitted to $\beta_{R_\omega^+}$ for run B. (bottom) A quadratic is fitted to $\beta_{R_\omega^+}$ for run C.	106
7.14	The above compares the Vieillefosse and Full equation trajectories at $t=0.3$ for dataset B. Here the paths appear to be much more regimented in the Vieillefosse assumption, with the full equations showing the swirling interactions we would expect from a developing flow.	108
8.1	The global helicity, H for calculation A.	113

Acknowledgments

Throughout my time at Warwick University I have made some true friends, most of whom I would not have the pleasure of meeting if I had not undertaken a Ph.D. However the following people deserve a special mention; Paul Clifford, Jason Laurie, Dana Elam, Sebastian Pinski, Amar Parmar and not forgetting Ahmed Al-Makky without whom, working in a room with no windows would have been unbearable. Additionally, I would like to thank Jason and Dana for offering me a place to sleep when I travelled down in the final year of my Ph.D.

I would like to pay special thanks to Robert M. Kerr. Without Bob I would not have had the opportunity or funding to be able to undertake postgraduate study at Warwick; and for this I am eternally grateful. Aside from this, Bob has been essential in my development as a Research Scientist and has never failed in being able to answer any questions I have had. Thank you.

Finally, I would like to dedicate this Thesis to my wife Gemma and son Henry.

Declarations

I wish to declare that this work is my own unless stated otherwise. I state that this thesis has not been submitted for a degree at another university.

Abstract

The Restricted Euler equations, taken from the Vieillefosse model for the velocity gradient tensor, are re-investigated using data from direct numerical simulations of an intense event, rather than using data from forced simulations of homogeneous, isotropic turbulence. The goal is to develop ideas for extensions to turbulence models based on the RE equations that can handle these intense events. With this goal in mind, the new numerical data is compared against the evolution of the RE equations towards a finite time limit and its predictions on how ratios of the RE moments converge. The analysis starts by looking at distributions of the invariants in the R-Q phase space. From this, the analysis then compares the Vieillefosse equations to the full equations and notes that there is a significant change in behaviour around $t = 0.5$. It is suggested that this is associated with a change in flow topology due to the reconnection of vortex tubes in the flow field. To build a higher-order model, more terms from the full RE equations should be used, which is investigated by looking at the co-evolution of the second invariant Q and the third-order moments, R_ω and R_S .

Nomenclature

Abbreviations

RE	Restricted Euler.
ODE	Ordinary Differential Equation.
MFLOPS	Million Floating Point Operations per Second.
VGT	Velocity Gradient Tensor.
DNS	Direct Numerical Simulation.
CGT	Cauchy Green Tensor.
FTS	Full Turbulence Simulation.
CFD	Computational Fluid Dynamics.
LES	Large Eddy Simulation.
RANS	Reynolds Averaged Navier-Stokes.
NSE	Navier-Stokes Equations.
NCAR	National Centre for Atmospheric Research.
DES	Detached Eddy Simulation.
CFL	Courant Friedrich's Levy.
RAM	Random Access Memory.
MPI	Message Passing Interface.
VTK	Visualisation Toolkit.
CMT	Conditional Mean Trajectories.

List of Symbols

\mathbf{u} Velocity.	α Vortex Stretching.
∇ Gradient Operator.	χ Vortex Rotation Rate.
Δ Laplacian.	D Vieillefosse discriminant.
p Pressure field.	Re Reynolds Number.
ν Kinematic Viscosity.	S_k Velocity derivative skewness.
ρ Density.	H Hessian.
ω Vorticity.	B Reference Configuration.
S Strain Tensor.	B' Deformed Configuration.
Ω Vorticity Tensor.	ϕ Deformation Map.
P pressure Hessian.	F Deformation Gradient.
$\frac{D}{Dt}$ Lagrangian Derivative.	N Nonlinear term.
I Identity Matrix (Order 3).	M Diffusion term.
δ_{ij} Kronecker Delta.	D_{ijkl} Drift Coefficient.
A Velocity Gradient Tensor.	W Wiener process.
\otimes Dyadic Product.	h_{ij} Normalised VGT.
S^2 Dissipation.	ϕ^* Pseudo-dissipation.
ω^2 Enstrophy.	\hat{a}^2 Time rate variance.
R_S Dissipation Production.	X Lagrangian point.
R_ω Enstrophy Production.	x Eulerian point.
I_4 Fourth order rotational invariant.	C Cauchy Green Tensor.
Q Second Invariant of the VGT.	dW Gaussian Forcing.
R Third Invariant of the VGT.	L Domain size.
q Quaternion.	η Kolmogorov microscale.
σ_i Pauli Spin Matrices.	ϵ Dissipation rate.
	l Integral Scale.

λ Taylor Microscale.
 Δx Mesh spacing.
 k Wave number.
 $E(k)$ Energy Spectrum.
 $T(k, t)$ Energy Transfer Function.
 $\mathbf{P}(\cdot)$ Probability density function.
 $h(\cdot)$ Helicity density.
 I_i Cayley Hamilton Invariants ($i = 1, 2, 3$).
 s_i Strain eigenvalues ($i = 1, 2, 3$).
 Re_λ Taylor (microscale) Reynolds Number.
 $\|\boldsymbol{\omega}\|_\infty$ L-infinity norm of the vorticity.
 β Normalised middle eigenvalue of the Strain.

Chapter 1

Introduction

1.1 Production Mechanisms of Intense Events

A popular question in fluid dynamics is what is turbulence? Turbulence in the modern world is generally used to describe periods of rapidly changing conditions such as those experienced in the financial markets. However to date we do not have a full and complete description of what turbulence is, we can describe a turbulent flow but we can not rigorously define what turbulence is. As you walk in the wind, you will leave a turbulent wake in your shadow, the motions of clouds are governed by the mixing flow within their boundaries. Turbulence is an essential part of life on earth, which possibly goes some way to explaining why no rigorous formulation has been derived.

What we intend to discuss in this thesis are the key components of turbulence within the inertial range. In order to do this we will be examining the role of the velocity gradient tensor numerically using Robert Kerr's pseudospectral code. The study of the pressure term and specifically the pressure Hessian has far reaching real world applications, particularly in the study of Aeroacoustics. Lighthill showed that the source term for the generation of sound in the Lighthill equations' is the second order partial derivative of the pressure, which creates a quadrupole source term for aerodynamic sound [1]. We would like to develop a method of simplifying the study of turbulent flows through the investigation of the key invariants of the velocity field, their growth and the effect of the pressure Hessian. To achieve this we will be considering the

following topics:

- Chapter 2: Background and Motivation

We will look at the production mechanisms of intense events within a developing turbulent flow. To do this we need to look at what others have done to address the issue of closing the incompressible Navier Stokes equations (NSE). We start by reviewing the work on the Restricted Euler (RE) equations as published by Vieillefosse [2], and conclude the literature review through the consideration of the relatively recent work by Chevillard & Meneveau [3] where they use the Cauchy Green Tensor to provide a closure for the pressure and viscous terms of the Navier Stokes Equations.

- Chapter 3: Direct Numerical Simulation

Following on from the literature review we consider how DNS is used to generate a turbulent flow, and briefly describe the methods used within Robert M. Kerr's pseudospectral code summarising the potential pit falls of DNS.

- Chapter 4: Computational Method

Here we will discuss the simulations used for the later analysis and present the three-dimensional energy spectra of each simulation. We then look at ways of visualising the flow using the VisIt visualisation package and the VTK file format.

- Chapter 5: Validation

The Vieillefosse RE equations are examined, after which we briefly review the work of Ashurst et al [4] and Kerr [5]. The focus shifts to the behaviour of the individual moments within the R-Q plane.

- Chapter 6: The pressure Hessian

The pressure Hessian \mathbf{P} is the second order tensor comprised of the second order partial derivatives of the pressure. We discuss the possible method of calculating the pressure Hessian and explain how it can be decomposed into a local and non local component through the solution of the Poisson equation for \mathbf{P} in terms of the velocity gradient tensor \mathbf{A} .

We plot the trajectories of the isotropic and full equations, and compare this with previous work.

- Chapter 7: 3D Phase Space

The 3D phase space (Q, R_ω, R_S) was introduced by Lüthi [6], here we look at the comparisons that can be drawn by considering the trajectories of the Vieillefosse and full equations in the 3D phase space before suggesting how the current RE equations can be improved. In essence this reaffirms the results of Chapter 6.

- Chapter 8: Conclusions and Further Work

Finally we reflect on what has been observed and consider possible extensions and applications of this study.

Chapter 2

Background and Motivation

2.1 Introduction

Scientists worldwide have been trying to unlock the secrets of Turbulence for hundreds of years, starting with Archimedes (287 BC-212 BC) up until the relatively recent derivation of the Navier-Stokes equations in 1845 [7]. Since then slowly but surely we are uncovering new turbulent phenomena. The advancement of massively parallel supercomputers; and increased competition and collaboration between researchers in the field, will hopefully one day lead to a definition of turbulence.

This thesis will consider the development of intense structures within a developing turbulent flow, we will begin our journey with the work of Vieillefosse [8] who suggested a simplified model of the Euler equation. We will then follow the contributions of other researchers until we arrive at the current understanding of turbulence.

The fundamental problem with any research into fluid flow, is the inability to measure a flow without causing an effect within the flow. There are many methods in the Computational Fluid Dynamics toolbox that allow the identification of structures and relationships that would be difficult to observe and measure accurately experimentally. The more sophisticated CFD methods are expensive, they require extensive computational resources and time to interpret the results. When modelling the Navier Stokes or Euler equations, a

closed set of equations is required in order to generate results. Further research into turbulence requires that these models are improved. We initially restrict our interest to the Vieillefosse closure and the early pioneers of numerical turbulence research.

The interaction of the various velocity derivatives is a key topic throughout this thesis. A greater understanding of velocity derivatives, particularly with regard to the development and dissipation of turbulent structures has the potential to create advances in fields such as Aeroacoustics.

In 1982 Vieillefosse published work on a closure for the Navier Stokes equations, this work observed a divergence of the vorticity in finite time for the inviscid equations [8]. An understanding of the energy transfer between the small and the large scales of turbulence is key to developing a comprehensive understanding of turbulence in general.

2.2 Euler Equations

The Euler equations for an incompressible homogeneous fluid are:

$$\frac{\partial \mathbf{u}}{\partial t} + \mathbf{u} \cdot \nabla \mathbf{u} = -\frac{1}{\rho} \nabla p, \quad \text{with} \quad \nabla \cdot \mathbf{u} = 0, \quad (2.1)$$

where \mathbf{u} is the velocity, $\mathbf{u} \cdot \nabla \mathbf{u}$ represents the advection of the velocity throughout the flow, p is the pressure and ρ is the fluid density. The incompressibility condition $\nabla \cdot \mathbf{u} = 0$ works to preserve the fluid volume.

2.3 The Navier Stokes Equations

The Navier Stokes Equations for an incompressible flow are:

$$\frac{\partial \mathbf{u}}{\partial t} + \mathbf{u} \cdot (\nabla \mathbf{u}) = -\frac{1}{\rho} \nabla p + \nu \nabla^2 \mathbf{u}, \quad (2.2)$$

along with the incompressibility condition:

$$\nabla \cdot \mathbf{u} = 0. \quad (2.3)$$

Here the variables are defined as in the Euler equation, there is the extra consideration of the viscosity ν .

Considering the incompressible Navier Stokes equations at high Reynolds number, one can assume that for short times the viscosity in the Navier Stokes equations can be neglected, and the fluid velocity will satisfy the Euler equations. At high Reynolds numbers the energy is distributed within a range of scales, the inertial range. This distribution is not affected by viscosity to a first approximation.

2.3.1 Strain

The strain rate tensor \mathbf{S} is defined as:

$$\mathbf{S} = S_{ij} = \frac{1}{2} \left(\frac{\partial u_i}{\partial x_j} + \frac{\partial u_j}{\partial x_i} \right). \quad (2.4)$$

The evolution of the strain can be determined as follows:

$$\frac{D\mathbf{S}}{Dt} = -\mathbf{S}\mathbf{S} - \frac{1}{4}\boldsymbol{\omega} \otimes \boldsymbol{\omega} + \frac{1}{4}\mathbf{I}|\boldsymbol{\omega}|^2 - \mathbf{P}, \quad (2.5)$$

where $\mathbf{P} = P_{ij} = \frac{\partial^2 P}{\partial x_i \partial x_j}$ is the pressure Hessian. Please also note that \otimes is the dyadic product.

2.3.2 Vorticity Equations

The vorticity highlights where vortex stretching originates from. Taking the curl of the Euler equation (2.1) and applying the following identity:

$$[(\boldsymbol{\omega} \cdot \nabla)u]_i = \omega_j u_{i,j} = \frac{1}{2}(u_{i,j} + u_{j,i})\omega_j = S_{ij}\omega_j = (S\boldsymbol{\omega})_i, \quad (2.6)$$

the inviscid vorticity form of the Euler equation is obtained, note that $\nabla \times \nabla \mathbf{u} = 0$ and $\nabla \times \nabla p = 0$:

$$\frac{D\boldsymbol{\omega}}{Dt} = \mathbf{S}\boldsymbol{\omega}, \quad (2.7)$$

where $\frac{D}{Dt} = \partial_t + \mathbf{u} \cdot \nabla$ is the material time derivative.

Alternatively, if one was to take the curl of the Navier-Stokes equation (2.2) the three-dimensional vorticity evolution equation can be obtained. If one applies the incompressibility condition to the following vector identity:

$$\nabla \times (\mathbf{u} \cdot \nabla \mathbf{u}) = \mathbf{u} \cdot \nabla (\nabla \times \mathbf{u}) - (\nabla \times \mathbf{u}) \cdot \nabla \mathbf{u} + (\nabla \cdot \mathbf{u})(\nabla \times \mathbf{u}). \quad (2.8)$$

Applying the incompressibility condition $\nabla \cdot \mathbf{u} = 0$ and noting that the curl of the pressure gradient is zero, $\nabla \times \nabla p = 0$, equation (2.2) becomes:

$$\frac{\partial \boldsymbol{\omega}}{\partial t} + \mathbf{u} \cdot \nabla \boldsymbol{\omega} = \boldsymbol{\omega} \cdot \nabla \mathbf{u} + \nu \nabla^2 \boldsymbol{\omega}. \quad (2.9)$$

Or, in terms of the material derivative:

$$\frac{D\boldsymbol{\omega}}{Dt} = \boldsymbol{\omega} \cdot \nabla \mathbf{u} + \nu \nabla^2 \boldsymbol{\omega}, \quad (2.10)$$

this is the vorticity equation, note that unlike the equation for the strain evolution, equation (2.5) the vorticity equation does not involve a contribution from the pressure.

2.4 Vieillefosse

Vieillefosse [8] wanted to understand the interactions within a flow, he reformulated the Euler equation into more manageable terms, the Restricted Euler (RE) model. Vieillefosse's particular interest was how the strain and vorticity affected the transfer and dissipation of energy between the large and small scales of fluid motion.

Taking the gradient of the Euler equation and omitting the contribution of pressure term, the gradients of the vorticity and stress as detailed in [2], define a system of 8 first-order ordinary differential equations. The derived quantities

provide a measure of the flow characteristics:

$$\frac{d}{dt}\omega_i = \frac{1}{2}\omega_j u_{ji}. \quad (2.11)$$

Vieillefosse defines u_{ij} as the fluid shear:

$$u_{ij} = \left(\partial_i v_j + \partial_j v_i - \frac{2}{3} \delta_{ij} \partial_l v_l \right), \quad (2.12)$$

and its derivative:

$$\frac{d}{dt}u_{ij} = -\frac{1}{2} \left(u_{ik} u_{kj} - \frac{1}{3} \delta_{ij} u_{kl} u_{lk} \right) - \frac{1}{2} \left(\omega_i \omega_j - \frac{1}{3} \delta_{ij} \omega_k^2 \right). \quad (2.13)$$

The incompressibility condition $u_{11} + u_{22} + u_{33} = 0$ is satisfied identically at all times.

The eight equations are reduced into equations for five primary velocity moments. These equations are investigated by considering linear combinations of the velocity moments. A divergence in finite time is observed, and determined to be dependent on the initial flow configuration. Vieillefosse arrived at similar results to those before him [9], [10], [11].

The eigenvalues of the strain and velocity gradients diverge following an inverse time scale power law dependence t^{-1} , and thus it would appear that the Enstrophy diverges as the square of the inverse time scale t^{-2} . We will discuss this possible power law dependence in Chapter 5.

2.5 Mathematical Preliminaries

In a dynamical system the scalars and vectors describe the magnitude and direction of motion. In two dimensions this is the minimum requirement to visualise the flow field. In three-dimensional space you need the magnitude, direction and orientation of the quantities in order to fully consider their evolution. This requires a brief discussion of tensors. A first order tensor is equivalent to a vector in that it captures magnitude and direction at a given

instant, however the interaction of first order tensors, (the velocity derivatives) is described by nine components. These are represented by second order tensors, which are typically represented as a 3×3 matrix in Euclidean space, $\mathbf{A}_{3 \times 3} \in \mathbb{E}^3$. Second order tensors are associative but not commutative.

We will focus on the evolution of invariant quantities within the flow. The velocity moments and the invariant moments of the pressure Hessian are of particular interest. Considering the rotational invariants of a system is useful as they are independent of a co-ordinate basis. The eigenvalues and eigenvectors are calculated as $(\mathbf{A} - \lambda \mathbf{I}) \mathbf{x} = 0$, where \mathbf{A} is a tensor of order 2, λ is the eigenvalue, \mathbf{I} is the 3×3 identity matrix and \mathbf{x} is the eigenvector. The system has three eigenvectors and by considering the determinant we may introduce the Cayley Hamilton Theorem.

2.5.1 Cayley-Hamilton Theorem

It is well known that any second order tensor \mathbf{S} is a solution of its characteristic polynomial. The characteristic polynomial is defined as:

$$c(\lambda) = \det(\mathbf{S} - \lambda \mathbf{I}) = \lambda^3 - I_1(\mathbf{S})\lambda^2 + I_2(\mathbf{S})\lambda - I_3(\mathbf{S}). \quad (2.14)$$

So, by replacing λ by the tensor \mathbf{S} :

$$c(\mathbf{S}) = \mathbf{S}^3 - I_1(\mathbf{S})\mathbf{S}^2 + I_2(\mathbf{S})\mathbf{S} - I_3(\mathbf{S})\mathbf{I} = 0, \quad (2.15)$$

where λ is the eigenvalue, and \mathbf{I} is the 3×3 identity matrix. The $I_i(\mathbf{S})$ are the first, second and third invariants of \mathbf{S} and can be defined as:

$$\begin{aligned} I_1(\mathbf{S}) &= \text{tr}(\mathbf{S}), \\ I_2(\mathbf{S}) &= \frac{1}{2} \{ (\text{tr} \mathbf{S})^2 - \text{tr}(\mathbf{S}^2) \}, \\ I_3(\mathbf{S}) &= \det(\mathbf{S}). \end{aligned} \quad (2.16)$$

Let the Strain Tensor \mathbf{S} have ordered eigenvalues:

$$s_1 \leq s_2 \leq s_3. \quad (2.17)$$

The trace of \mathbf{S} is then obtained through the use of the incompressibility condition:

$$I_1(\mathbf{S}) = \text{tr}(\mathbf{S}) = s_1 + s_2 + s_3 = 0. \quad (2.18)$$

From this we can look at the second invariant and note that this contains the sum of the cross acting terms only:

$$I_2(\mathbf{S}) = \frac{1}{2} \{ (\text{tr} \mathbf{S})^2 - \text{tr}(\mathbf{S}^2) \} \quad (2.19)$$

$$= \frac{1}{2} \left(\left(\sum s_i \right)^2 - \left(\sum s_i^2 \right) \right) \quad (2.20)$$

$$= \sum_{i \neq j} s_i s_j. \quad (2.21)$$

Finally, the third invariant is simply the determinant, which is the product of the eigenvalues:

$$I_3 = s_1 s_2 s_3. \quad (2.22)$$

It is noteworthy to define:

$$S^2 = \text{tr} \mathbf{S}^2 = s_1^2 + s_2^2 + s_3^2. \quad (2.23)$$

2.6 Moments

The development of the 5 invariants of the Velocity gradient tensor is of interest. Considering the isotropic assumption the invariants are:

$$\mathbf{S}^2, \boldsymbol{\omega}^2, \mathbf{R}\boldsymbol{\omega} \mathbf{R}\mathbf{S}, \text{ and } I_4. \quad (2.24)$$

These velocity moments are the Enstrophy, strain, Enstrophy production, strain production and the fourth order tensor I_4 . I_4 is one of the fourth-order rotationally invariant derivative correlations in isotropic turbulence [12]. The Enstrophy is the square of the vorticity ($\boldsymbol{\omega}$), $\omega^2 = |\boldsymbol{\omega}|^2$, and the growth of Enstrophy is given by $R_\omega = \omega_i S_{ij} \omega_j$ this is obtained when you take material derivative of the Enstrophy. The dissipation is the square of the strain, and can be found as $S^2 = S_{ij} S_{ji} = S_1^2 + S_2^2 + S_3^2$, with the corresponding dissipation production term being given by $R_S = S_{ij} S_{jk} S_{ki} = S_1^3 + S_2^3 + S_3^3$. Finally, Siggia's $I_4 = (\omega_i S_{ij})^2$ [12]. The Vieillefosse equations evolve in the absence of

pressure according to:

$$\frac{d}{dt}\mathbf{S}^2 = -2\mathbf{R}\mathbf{S} - \frac{1}{2}\mathbf{R}\boldsymbol{\omega}, \quad (2.25)$$

$$\frac{d}{dt}\boldsymbol{\omega}^2 = 2\mathbf{R}\boldsymbol{\omega}, \quad (2.26)$$

$$\frac{d}{dt}\mathbf{R}\mathbf{S} = \frac{3}{4}\mathbf{I}_4 + \frac{1}{4}\mathbf{S}^2\mathbf{Q}, \quad (2.27)$$

$$\frac{d}{dt}\mathbf{R}\boldsymbol{\omega} = \mathbf{I}_4 - \frac{2}{3}\boldsymbol{\omega}^2\mathbf{Q}, \quad (2.28)$$

$$\frac{d}{dt}\mathbf{I}_4 = -\frac{4}{3}\mathbf{Q}\mathbf{R}\boldsymbol{\omega}. \quad (2.29)$$

These equations reduce to a pair of ordinary differential equations expressed in terms of Q and R which are derived in equation (2.67). Q and R are defined in terms of the second and third order moments respectively:

$$Q = -\frac{1}{2}\mathbf{S}^2 + \frac{1}{4}\boldsymbol{\omega}^2, \quad (2.30)$$

and

$$R = -\frac{1}{3}\mathbf{R}\mathbf{S} - \frac{1}{4}\mathbf{R}\boldsymbol{\omega}. \quad (2.31)$$

The balance of equations (2.30) and (2.31) is given by the discriminant D :

$$D = \frac{27}{4}R^2 + Q^3. \quad (2.32)$$

Considering $D = 0$:

$$\frac{27}{4}R^2 + Q^3 = 0, \quad (2.33)$$

rearranging gives:

$$R = \left(-\frac{4}{27}Q^3\right)^{\frac{1}{2}}, \quad (2.34)$$

this family of curves is plotted in figure 2.1.

2.7 Alternative Consideration

In 2002 Gibbon [13] decided to approach the Euler equations in terms of quaternions, as an alternative tool in the study of vorticity along Lagrangian

trajectories. A quaternion is a vector scalar component defined as:

$$\mathbf{q} = [a, \mathbf{r}] = a\mathbf{I} - \mathbf{r} \cdot \boldsymbol{\sigma}. \quad (2.35)$$

Where \mathbf{I} is the 2x2 unit matrix and for those familiar with quantum physics; σ_i are the Pauli spin matrices. Quaternions are not commutative but their associativity can be shown. The vorticity becomes a pure quaternion by setting $a = 0$ in equation (2.35), $\mathbf{r} = \boldsymbol{\omega}$.

The Euler equations are reformulated using the following variables:

$$\alpha = \hat{\boldsymbol{\omega}} \cdot (\mathbf{S}\hat{\boldsymbol{\omega}}), \quad \text{where} \quad \hat{\boldsymbol{\omega}} = \frac{\boldsymbol{\omega}}{|\boldsymbol{\omega}|}, \quad \text{and} \quad \boldsymbol{\chi} = \hat{\boldsymbol{\omega}} \times \mathbf{S}\hat{\boldsymbol{\omega}}. \quad (2.36)$$

α and $\boldsymbol{\chi}$ represent the vortex stretching and rotation rates respectively. The evolution of these quantities is derived as follows:

$$\frac{D}{Dt}|\hat{\boldsymbol{\omega}}| = \hat{\boldsymbol{\omega}} \times \boldsymbol{\chi}, \quad (2.37)$$

$$\frac{D\alpha}{Dt} = -\alpha^2 + \boldsymbol{\chi}^2 - \alpha_p, \quad (2.38)$$

$$\frac{D\boldsymbol{\chi}}{Dt} = -2\alpha\boldsymbol{\chi} - \boldsymbol{\chi}_p, \quad (2.39)$$

$$\boldsymbol{\chi}_p = \hat{\boldsymbol{\omega}} \times \mathbf{P}\hat{\boldsymbol{\omega}}, \quad (2.40)$$

$$\alpha_p = \hat{\boldsymbol{\omega}} \cdot (\mathbf{P}\hat{\boldsymbol{\omega}}). \quad (2.41)$$

Reformulating the equations in this manner provides a convenient framework to explore the Lagrangian evolution of vorticity. The growth of the normalised vortex stretching $\frac{D\alpha}{Dt}$ is of particular interest.

2.8 The Restricted Euler Model

The velocity gradient tensor (VGT) is a second order tensor containing all of the spatial first order velocity derivatives defined as:

$$A_{ij} = \frac{\partial u_i}{\partial x_j} = u_{i,j}. \quad (2.42)$$

The velocity gradient tensor can be decomposed into its symmetric and anti-symmetric components. Defining the decomposition as follows $\mathbf{A} = \mathbf{S} + \mathbf{\Omega}$, the strain tensor is the symmetric part:

$$\mathbf{S} = \frac{1}{2}(\mathbf{A}_{ij} + \mathbf{A}_{ji}), \quad (2.43)$$

and the vorticity tensor $\mathbf{\Omega}$ is the antisymmetric part:

$$\mathbf{\Omega} = \frac{1}{2}(\mathbf{A}_{ij} - \mathbf{A}_{ji}). \quad (2.44)$$

Decomposing the VGT into the symmetric and antisymmetric parts, the strain and vorticity starts the discussion of two different interconnected aspects of fluid motion.

Consider the incompressible Euler equation (2.1) in component form where \mathbf{u} is the velocity field and p is the pressure field.

$$\frac{\partial}{\partial x_j} \left(\frac{\partial u_i}{\partial t} + u_k \frac{\partial u_i}{\partial x_k} \right) = - \frac{\partial p}{\partial x_i \partial x_j}, \quad (2.45)$$

then:

$$\frac{\partial}{\partial t} \frac{\partial u_i}{\partial x_j} + \frac{\partial u_k}{\partial x_j} \frac{\partial u_i}{\partial x_k} + u_k \frac{\partial}{\partial x_k} \frac{\partial u_i}{\partial x_j} = - \frac{\partial p}{\partial x_i \partial x_j}, \quad (2.46)$$

rewritten in terms of \mathbf{A} :

$$\frac{\partial}{\partial t} A_{ij} + A_{ik} A_{kj} + u_k \frac{\partial}{\partial x_k} A_{ij} = - \frac{\partial p}{\partial x_i \partial x_j}. \quad (2.47)$$

The incompressibility condition can also be rewritten in terms of the VGT, where summing over repeated indices is assumed:

$$A_{ii} = 0. \quad (2.48)$$

The material derivative applied to equation (2.47) yields:

$$\frac{D}{Dt} A_{ij} = -A_{ik} A_{kj} - \frac{\partial p}{\partial x_i \partial x_j}. \quad (2.49)$$

Equation (2.49) can not be solved without solving the pressure Hessian or finding a suitable assumption for the behaviour of the pressure Hessian. A suitable assumption that allows the equation to be integrated numerically is called a closure.

2.9 Ashurst

The next milestone in understanding the role of velocity gradients in turbulent flow was achieved in the 1980's with the introduction of the C Shaped CRAY-1 Supercomputer. The CRAY-1 was capable of 80 million floating point operations per second (80 MFLOPs) today the latest iPhone runs at approximately 120 MFLOPs. The CRAY-1 was twice as fast as its predecessor the CDC 7600 and it was far more reliable. Robert M Kerr was fortunate enough to obtain access to this machine allowing him to produce his 1985 paper [14] and subsequently the joint work with Ashurst et al [4] published in 1987.

Robert Kerr used 70 hours of computational time on the CRAY-1S supercomputer to produce a 128^3 dataset at $R_\lambda = 83$ of three eddy turnover times. The 1985 paper discusses higher order derivative correlations, in particular the skewness (S_k) and kurtosis. Kerr suggests that turbulence is characterised by extended vortex tubes and strong alignment between vorticity and rate of strain.

The alignment of the vorticity and strain was first studied numerically by Siggia [15] and Kerr [14]. However it wasn't until Kerr [5] and Ashurst et al [4] that the distribution of the alignment of vorticity and strain was studied numerically. Using a 128^3 DNS simulation of isotropic flow with a homogeneous shear flow, the distribution of the alignment between the strain and vorticity was observed [4].

The primary results are for the ordered strain eigenvalues $s_1 \leq s_2 \leq s_3$. The incompressibility condition implies that $\sum_i s_i = 0$. So when $s_2 < 0$, s_2 and s_1 are compressive. The most common alignment of the strain in intense regions is approximately $s_1 : s_2 : s_3 = -4 : 1 : 3$. This represents an element

being pulled in two directions and crushed in the third. β is defined to be the normalised middle eigenvalue, with limits ± 1 and is calculated as:

$$\beta = \frac{\sqrt{6}s_2}{|\mathbf{S}|}, \quad |\mathbf{S}| = \sqrt{s_1^2 + s_2^2 + s_3^2}. \quad (2.50)$$

Regions of active and passive flow are studied using the probability density function for β . This study shows that the peak of the probability density function for β occurs when $\beta = 0.5$.

Tennekkes previously estimated the volume of vortex tubes to be the inverse of the Taylor Reynolds number [16]. Ashurst et al [4] observe that the tube diameter is of the same order as the kurtosis factor, this suggests a larger volume of vortex tubes than had previously been observed. In the active regions β is generally positive. They observe that the intermediate strain eigenvector, corresponding to the eigenvalue s_2 is aligned with the vorticity stretched along that eigenvalue. This can be quantified by taking absolute value of the dot product with the intermediate eigenvalue.

2.10 Cantwell

Cantwell [38] extends the analytical approach of Vieillefosse [2] to the incompressible Navier Stokes equation:

$$\frac{\partial}{\partial t} A_{ij} + A_{kj} A_{ik} + u_k \frac{\partial}{\partial x_k} A_{ij} = -\frac{\partial p}{\partial x_i \partial x_j} + \nu \frac{\partial^2 A_{ij}}{\partial x_k \partial x_k}. \quad (2.51)$$

Taking the trace $A_{ii} = 0$ of equation (2.51), the pressure can be understood in terms of the VGT:

$$A_{kj} A_{jk} = -\frac{\partial p}{\partial x_j \partial x_j}. \quad (2.52)$$

The contribution of the trace/isotropic component from A^2 and the pressure term needs to be removed. This is achieved through the use of Kronecker delta:

$$\delta_{ij} = \begin{cases} 1 & \text{if } i = j \\ 0 & \text{Otherwise} \end{cases} \quad (2.53)$$

Hence, using (2.53) in (2.52) one obtains:

$$A_{ik}A_{kj}\frac{\delta_{ij}}{3} = -\frac{\partial p}{\partial x_i\partial x_j}\frac{\delta_{ij}}{3}, \quad (2.54)$$

subtracting (2.54) from the velocity gradient form of the Navier Stokes equation (2.51) one arrives at the full restricted Euler equation:

$$\frac{\partial}{\partial t}A_{ij} + A_{ik}A_{kj} - (A_{km}A_{mk})\frac{\delta_{ij}}{3} + u_k\frac{\partial}{\partial x_k}A_{ij} = H_{ij} + \nu\frac{\partial^2 A_{ij}}{\partial x_k\partial x_k}, \quad (2.55)$$

where:

$$H_{ij} = -\left(\frac{\partial p}{\partial x_i\partial x_j} - \frac{\partial p}{\partial x_k\partial x_k}\frac{\delta_{ij}}{3}\right), \quad (2.56)$$

finally,

$$\frac{D}{Dt}A_{ij} + A_{ik}A_{kj} - (A_{km}A_{mk})\frac{\delta_{ij}}{3} = H_{ij} + \nu\frac{\partial^2 A_{ij}}{\partial x_k\partial x_k}. \quad (2.57)$$

In order to solve equation (2.57) a suitable closure for the pressure and viscous terms must be chosen. Remember also that the term A^2 contains the non local part of the pressure Hessian. H_{ij} contains the viscous diffusion of the velocity gradients and the cross derivatives of the pressure field.

Cantwell's intent was to explore the secrets of the sub scale region. In this region the velocity gradients dominate the flow, his work focuses on the condition that $H_{ij} = 0$. Referencing Chong Perry and Cantwell (1990) [17] he applies the nomenclature for the second and third invariants of the Cayley Hamilton equation as suitable quantities to determine the flow topology.

Before we consider the derivation of R and Q for the RE model, the Poisson equation for the pressure shows that the pressure Hessian is related to the square of the velocity gradient tensor as observed in equation (2.52). The equation for the VGT evolution (2.57) indirectly includes the anisotropic part of the pressure Hessian when $H_{ij} = 0$. The effect this has on the flow is undetermined at this point, although it is something we hope to explore.

2.11 Deriving the RQ equations

The nomenclature of (P,Q,R) used to identify the first, second and third invariants of a 3D flow field was introduced by Chong, Perry and Cantwell 1990 [17] where they undertake a general classification of three-dimensional flow fields.

Applying Cayley Hamilton to A , denoting the eigenvalues as λ_i we have:

$$\lambda^3 + P\lambda^2 + Q\lambda + R = 0. \quad (2.58)$$

Following on from Chong et al [17], the first \mathbf{P} , second \mathbf{Q} and third \mathbf{R} invariants of the velocity gradient tensor are defined as:

$$\begin{aligned} \mathbf{P} &= A_{ii} = 0, \\ \mathbf{Q} &= -\frac{1}{2}A_{ij}A_{ji} = -\frac{1}{2}\mathbf{S}^2 + \frac{1}{4}\boldsymbol{\omega}^2, \\ \mathbf{R} &= -\frac{1}{3}A_{im}A_{mk}A_{ki} = -\frac{1}{3}\mathbf{R}\mathbf{S} - \frac{1}{4}\mathbf{R}\boldsymbol{\omega}. \end{aligned} \quad (2.59)$$

The first invariant is never referred to as \mathbf{P} , for one it would cause confusion with the pressure and in real terms it is the incompressibility condition. The aim is to understand the development of structures within a turbulent flow. How can the evolution equations for the second and third invariants of the VGT be obtained?

Post multiplying equation (2.57) by A_{ij} :

$$\frac{d}{dt}(A_{in}A_{nj}) + 2A_{in}A_{nk}A_{kj} - \frac{2}{3}(A_{km}A_{mk})A_{ij} = A_{in}H_{nj} + H_{in}A_{nj}, \quad (2.60)$$

taking the trace:

$$\frac{d}{dt}(-2Q) - 6R - \underbrace{\frac{2}{3}(A_{km}A_{mk})A_{ii}}_{=0} = 2A_{in}H_{ni}, \quad (2.61)$$

tidying up:

$$\frac{d}{dt}Q = -3R - A_{in}H_{ni}. \quad (2.62)$$

Similarly, R can be found:

$$\begin{aligned} \frac{d}{dt}(A_{iq}A_{qn}A_{nj}) + 3A_{iq}A_{qn}A_{nk}A_{kj} - (A_{mn}A_{nm})A_{iq}A_{qj} = \\ A_{in}A_{nk}H_{kj} + A_{in}H_{nk}A_{kj} + H_{in}A_{nk}A_{kj}, \end{aligned} \quad (2.63)$$

applying Cayley Hamilton to reduce the fourth-order product:

$$\begin{aligned} \frac{d}{dt}(A_{iq}A_{qn}A_{nj}) + 3(-PA_{in}A_{nk} - QA_{ik} - R\delta_{ik})A_{kj} \\ -(A_{mn}A_{nm})A_{iq}A_{qj} = A_{in}A_{nk}H_{kj} + A_{in}H_{nk}A_{kj} + H_{in}A_{nk}A_{kj}, \end{aligned} \quad (2.64)$$

taking the trace and using equation (2.59):

$$\begin{aligned} \frac{d}{dt}(-3R) - 3QA_{ik}A_{ki} - (-2Q)A_{iq}A_{qi} = \\ 3A_{in}A_{nk}H_{ki}, \end{aligned} \quad (2.65)$$

tidying up gives:

$$\frac{d}{dt}R = \frac{2}{3}Q^2 - A_{in}A_{nk}H_{ki}. \quad (2.66)$$

Applying the assumption $H_{ij} = 0$; separation of variables is used to obtain an equation that represents the path a particle dependant of course on the initial condition. If we plot this for a variety of initial conditions a family of curves is obtained. This is achieved as follows:

$$\frac{d}{dt}Q = -3R, \quad (2.67)$$

$$\frac{d}{dt}R = \frac{2}{3}Q^2, \quad (2.68)$$

$$dR = \frac{2}{3}Q^2dt \quad \text{and} \quad dQ = -3Rdt, \quad (2.69)$$

$$\int RdR = \int -\frac{2}{9}Q^2dQ \implies R^2 = -\frac{4}{27}Q^3 + C. \quad (2.70)$$

$$(2.71)$$

Hence,

$$R^2 + \frac{4}{27}Q^3 = C. \quad (2.72)$$

Cantwell also observes the alignment result of Ashurst et al [4], through the discussion of the VGT \mathbf{A} evolution. Further analysis is required of the interaction between the various invariant moments of \mathbf{H} . Cantwell is responsible for the nomenclature of R-Q dynamics by his use of Q and R for the second and third invariants applied to this problem. Now we will see that this system of equations has been studied extensively by many research groups [3], [18], [19] and [20]. Our focus lies with the behaviour of the pressure Hessian but this will be discussed in Chapter 6.

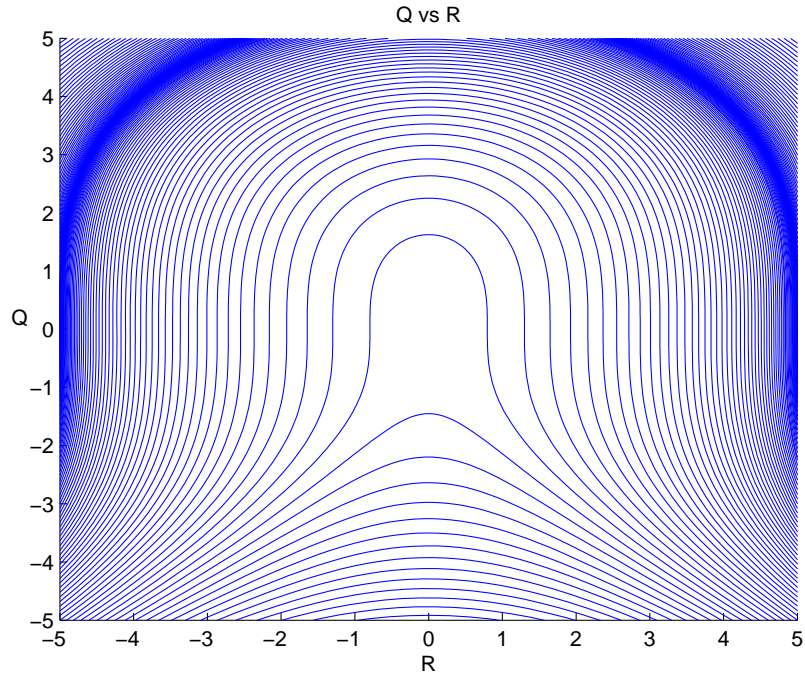


Figure 2.1: Trajectories of the second(Q) and third(R) invariants of the velocity gradient tensor \mathbf{A} .

2.12 Closure problem

The objective is to obtain a model that is to good approximation the Navier Stokes equations without resulting to a full calculation method such as direct numerical simulation. We have considered the early attempts to solve the restricted Euler equations numerically, with a simple isotropic closure for the pressure Hessian.

When we discuss particles, we typically think of the Eulerian representation, where a particle is expressed in terms of Cartesian co-ordinates. Hence the position \mathbf{x} of particle \mathbf{A} at time t is considered. Whereas the Lagrangian representation considers the material property of a particle as it moves through the fluid.

The initial reference configuration $\mathbf{B} \subset \mathbb{R}^3$ where $\mathbf{X} \in \mathbf{B}$ is the reference position of a particle. Then the deformed/spatial representation $\mathbf{B}' \subset \mathbb{R}^3$ where $\mathbf{x} \in \mathbf{B}'$ is the deformed position. This allows the deformation map ϕ to be defined:

$$\phi : \mathbf{B} \rightarrow \mathbf{B}' \quad (2.73)$$

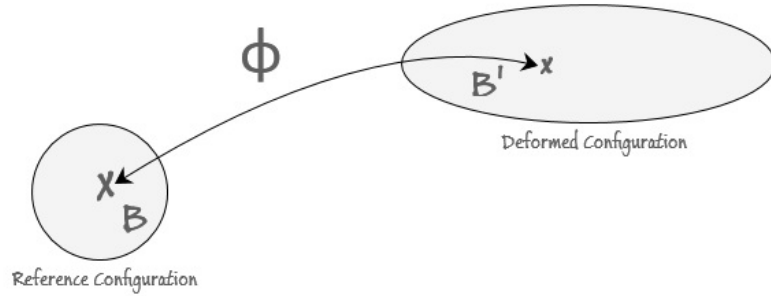


Figure 2.2: An illustration of the deformation map between the initial configuration and deformed configuration of a material body.

The displacement of the particle from its starting location to final position can be defined as:

$$\mathbf{u}(\mathbf{X}) = \phi(\mathbf{X}) - \mathbf{X} \quad (2.74)$$

From which the deformation gradient $\mathbf{F}(\mathbf{X})$ follows:

$$\mathbf{F}(\mathbf{X}) = \nabla \phi(\mathbf{X}) = \frac{\partial \phi(\mathbf{X})}{\partial X_i} \mathbf{e}_i \quad (2.75)$$

Here e_i represents the co-ordinate frame. This allows the Cauchy Green tensor \mathbf{C} and its inverse \mathbf{C}^{-1} to be defined as:

$$\mathbf{C} = \mathbf{F}\mathbf{F}^T \quad (2.76)$$

$$\mathbf{C}^{-1} = \mathbf{F}^{-T}\mathbf{F}^{-1} \quad (2.77)$$

The Cauchy Green Tensor (CGT) contains information about the stretching of the material only, whereas the deformation gradient contains mixed information on the nature of the rotations and stretches.

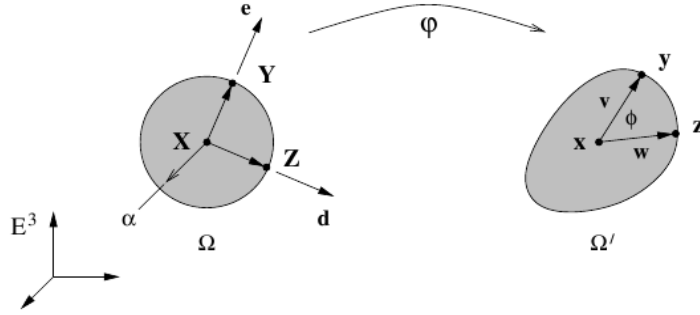


Figure 2.3: This figure taken from A first course in continuum mechanics [21] which illustrates the role and action of the Cauchy Green Tensor on the reference and deformed configurations.

Starting from Vieillefosse [8]; Girimanji and Pope [20] discuss whether a suitable model can be derived in a Lagrangian frame of reference that would give results comparable to direct numerical simulation. In 1989 they were motivated by limitations and cost of computational resource.

They ran a 128^3 simulation to compare their new model against. Their idea was to normalise the components of the Navier-Stokes Equation to develop a diffusion model for the normalised velocity gradient tensor, whilst retaining the full nonlinear term and only modelling the anisotropic pressure and viscous terms. The diffusion of the normalised velocity gradient tensor A^* can

be shown to be a stochastic differential equation:

$$dA_{ij} = A_{ij}(t + dt) - A_{ij}(t) \quad (2.78)$$

$$= [-N_{ij} + M_{ij}]dt + D_{ijkl}dW_{kl} \quad (2.79)$$

Here M and D represent the drift and diffusion terms respectively, N is the non-linear term and W is a Wiener process. The authors' ensure that the velocity gradient tensor still satisfies the kinematic constraints and the log normality of the pseudo-dissipation. They obtain a complex full model and two simplified models T1 and T2. The pseudo-dissipation is defined as $\phi = \nu \frac{\partial u_i}{\partial x_j} \frac{\partial u_i}{\partial x_j}$ and physically it represents energy transfer between the turbulent scales. For brevity, T2 is:

$$dh_{ij} = \left[- \left(N_{ij} - h_{ij} \frac{h_{lm} N_{lm}}{\phi^*} \right) - h_{ij} \left(\frac{7}{2} \hat{a}^2 + \frac{\ln \phi^*}{2\tau} \right) \right] dt + D_{ijkl} dW_{kl} \quad (2.80)$$

Where \mathbf{h} is the normalised velocity gradient tensor and \hat{a}^2 is the time rate variance. This model considers the action of the nonlinear term including the pseudo dissipation, the second term acts to preserve the log normality of the pseudo dissipation. The diffusion term is a model of the relationship between the time rate variance \hat{a}^2 and pseudo dissipation fluctuating in time due to the action of the Wiener process. This model contains a small number of quantities that must be determined computationally and as such this provides a distinct advantage when resources and computational power are at a high premium.

Girimanji and Pope compare the three models to the full turbulence simulation (FTS) to form a conclusion on the suitability and fit of a diffusion model for the velocity gradient tensor. Their results indicate that the model is reasonably successful, there is good correlation between the single time statistics of the scalar invariants. This method appears to show good promise for the development of other Lagrangian models for the evolution of the velocity gradient tensor.

Pumir, Shairman and Chertkov [19], look at the problem from another perspective. The previous attempts at explaining the understanding the local flow geometry and its evolution have all been from a somewhat classical view. The authors consider a tetrad. The tetrad is a 4 point model based on a coarse grained velocity gradient tensor defined over a region \mathbf{B} , with characteristic length scale R (i.e. the large energy containing eddies of size R).

$$A_{ab} = \int_{\mathbf{B}} d\mathbf{r} \partial_a \mathbf{v}_b(\mathbf{r}) \quad (2.81)$$

$$A_{ab} = (\xi^{-1})_i^a v_i^b - \frac{\delta_{ab}}{3} \text{tr}(\xi^{-1} \mathbf{v}) \quad (2.82)$$

How does this tetrahedron shaped fluid parcel develop and are any constraints applied to the flow? Their idea is based on the fact that the velocity field can be decomposed into a rapidly changing component modelled as Gaussian noise plus a slower component controlled by the interactions of eddies. They are attempting to decompose the velocity field so that the random motion and quantitative process can be studied separately:

$$v_i^a = \underbrace{\xi_i^b A_{ab}}_I + \underbrace{u_i^a}_{II} \quad (2.83)$$

A set of equations analogous to the standard evolution of the velocity gradient tensor are obtained [19].

$$\frac{d}{dt} A_{ab} + A_{ab}^2 - \underbrace{\Pi_{ab} \text{tr} A_{ab}^2}_{III} = \eta_{ab} \quad (2.84)$$

$$\frac{d}{dt} \xi_i^a - \xi_i^b A_{ab} = u_i^a \quad (2.85)$$

$$\Pi_{ab} = \frac{k_i^a k_i^b}{\text{tr} \mathbf{k} \mathbf{k}} \quad (2.86)$$

Where ξ is the matrix of triad vectors, $\mathbf{K} = \xi^{-1}$ and η is a random matrix, Note that Π_{ab} is a measure of the tetrad anisotropy.

In equation (2.84), you can see that the local component of the pressure field is $\Pi \text{tr} A^2$. Finally, the LHS of equation (2.84) is analogous to equation

(2.49), where η_{ab} introduces random forcing and the modelled contribution of the self-stretching term. Thus the tetrad evolution is fully defined [19]. The results of Vieillefosse can be recovered when $\Pi = \frac{1}{3}$. This paper is successful, it provided a new method of closing the Navier Stokes equation, with reasonable correlation to the results of DNS and experimentalists.

Yi and Meneveau [18] use the Cauchy Green tensor to describe the evolution of the deformation tensor. This is another method of investigating the physics of small scale turbulence.

The authors observe how spheres are deformed by compression and stretching to form ellipsoids, and as such the evolution is extremely similar to that of the velocity gradient tensor for short times. Their study provides an analytical solution.

$$\frac{DF_{ij}}{Dt} = F_{ik}a_{kj}, \quad (2.87)$$

where a_{kj} is the local component of the VGT. Here the focus is on how the material elements deform from spheres to ellipsoids, straight from the definition of \mathbf{F} .

The mapping from a spatial representation to a material frame is provided by:

$$|\delta \mathbf{X}|^2 = \delta \mathbf{x} \mathbf{C}^{-1} \delta \mathbf{x}^T \quad (2.88)$$

The use of the CGT to facilitate an investigation into the dynamics of small scale turbulence is new. Meneveau continued this work with Chevillard [3], where they produced a new stochastic model based on this work.

Their intent was to create a framework from which the statistical and geometric structure of turbulence can be investigated more thoroughly. They assume that the Lagrangian pressure Hessian is isotropic given that the flow has developed sufficiently to justify loss of information from previous times.

$$\frac{\partial^2 p}{\partial x_i \partial x_j} = \frac{\partial}{\partial x_i} \left(\frac{\partial p}{\partial x_j} \right) = \frac{\partial}{\partial x_i} \left[\left(\frac{\partial X_n}{\partial x_j} \right) \frac{\partial p}{\partial X_n} \right] \approx \frac{\partial X_m}{\partial x_i} \frac{\partial X_n}{\partial x_j} \frac{\partial^2 p}{\partial X_m \partial X_n} \quad (2.89)$$

Applying the inverse Cauchy Green tensor:

$$\frac{\partial^2 p}{\partial x_i \partial x_j} = \frac{1}{3} C_{ij}^{-1} P_{kk} \quad (2.90)$$

The compression and stretching of the Eulerian pressure Hessian is considered through the use of the inverse Cauchy Green tensor. The authors suggest this is a reinterpretation of the tetrad model. Although similar to other models, by capturing the effect of recent deformations the results should be closer to the true Hessian.

$$\frac{\partial^2 p}{\partial x_i \partial x_j} = -\frac{C_{ij}^{-1}}{C_{qq}^{-1}} A_{nm} A_{mn}. \quad (2.91)$$

Through the consideration of the time scale, they arrive at:

$$\nu \frac{\partial^2 A_{ij}}{\partial X_i \partial X_j} = \frac{-1}{T} \frac{C_{mm}^{-1}}{3} A_{ij}. \quad (2.92)$$

Finally, by using (2.91) and (2.92) they obtain the following stochastic differential equations where dW is a Gaussian forcing term.

$$dA = \left(-A^2 + \frac{Tr(A^2)}{Tr(C_\Gamma^{-1})} C_\Gamma^{-1} - \frac{Tr(C_\Gamma^{-1})}{3} A \right) dt + dW, \quad (2.93)$$

where $C_\Gamma = e^{\Gamma \mathbf{A}} e^{\Gamma \mathbf{A}^T}$ is the stationary Cauchy Green Tensor, and I think that Γ is the Kolmogorov time scale [3].

The authors solve the above equation numerically, providing comparison with previously published results such as the log normality of the pseudo dissipation, the classic RQ teardrop and the alignment of the intermediate eigenvalue of the strain tensor with the vorticity. Chevillard, Meneveau, Biferale and Toschi [22] look to extend this model with particular focus on the terms required to close the equation.

In summary, we have considered the work of many authors and their contribution to understanding small scale turbulence and the associated events created through the interaction of various invariants. What has yet to be seen is a thorough investigation of the true pressure Hessian, in particular its effect

on the dynamics and development of the Navier Stokes equation.

Chapter 3

Turbulence Simulations

3.1 Introduction

Direct Numerical Simulations (DNS) for the solution of the Navier Stokes equations is discussed. The study of turbulent flow is dominated by three species of computational model. The popular choices despite various conceptual difficulties in their implementation are Large Eddy Simulation (LES) and Reynolds Averaged Navier Stokes (RANS). LES is generally used for complex unstructured grids with irregular geometries whereas RANS is popular in motor sport. The simplicity afforded by the implementation of Direct Numerical Simulation(DNS) is overshadowed by the significant computational cost when simulating a flow even when studying simple geometries. DNS does not require a turbulent closure model and is of higher order accuracy than other mainstream methods. There are other types of CFD methods for non-turbulent problems these will not be discussed here.

3.2 Turbulence Preliminaries

When discussing turbulence several quantities are frequently discussed and are mentioned here for completeness. The Reynolds number Re was derived by Osbourne Reynolds in 1893. It was derived by the non dimensionalisation of the Navier Stokes equation.

$$Re = \frac{uL}{\nu} \tag{3.1}$$

Where: u is the velocity magnitude, L is a length scale and finally ν is the kinematic viscosity. The Reynolds number can be interpreted as the ratio between the inertial and viscous forces within the fluid. The common example when introducing Reynolds number is the consideration of the flow around a cylinder, and the turbulent flow achieved when the critical Reynolds number is exceeded.

Turbulent structures are continually undergoing fluid deformations at a variety of length scales. The size of the large scale eddies is called the integral scale L and the scale of velocity fluctuations is characterised by the Kolmogorov scale η , defined by the viscosity ν and the energy dissipation ϵ :

$$\eta = \left(\frac{\nu^3}{\epsilon} \right)^{\frac{1}{4}}. \quad (3.2)$$

The Kolmogorov scale is the characteristic size of the smallest dissipative eddies. The range of scales between the Kolmogorov scale and integral scale is called the inertial subrange: $\eta \ll r \ll L$. There is another commonly used length scale, the Taylor microscale λ :

$$\lambda^2 = \frac{u^2}{\left\langle \frac{\partial u_1}{\partial x_1} \right\rangle^2}. \quad (3.3)$$

This length scale lies within the inertial subrange $\eta \ll \lambda \ll L$. Direct Numerical Simulations frequently refer to Taylor Reynolds Number R_λ , as a measure of the interaction between large and small scales.

3.3 Direct Numerical Simulation

Direct Numerical Simulation (DNS) is a turbulence research tool capable of being utilised as a numerical experiment where the scientist has precise control over the initial conditions; this is not possible in an wind tunnel experiment. This allows insight into the turbulent flows dependence on the initial condition as well as access to the entire flow field in a way completely unobtainable by any physical experiment. However as with any form of numerical calculation you

must ensure that the method is suitable for the intended application as wrong choices can be very expensive in terms of physical time and computational resources. The main areas of concern for a DNS experiment are accuracy, storage requirements and the post computational analysis of the generated data which may need to be done alongside the calculation. DNS is attractive as you simply march the Navier Stokes equations (NSE) forward in time with a suitable time stepping regime such as third order Runge-Kutta from the initial condition.

A brief look at the origins of DNS

The birth of DNS was at National Centre for Atmospheric Research (NCAR) in 1972. The first calculation was performed on a 32^3 mesh with $R_\lambda = 35$ by Orszag and Patterson [23] in the same year. Where the Taylor-Reynolds number is defined as: $R_\lambda = \frac{u\lambda}{\nu}$. Rogallo [24] extended the work of Orszag and Patterson to homogeneous turbulence whilst at NASA Ames. If we compare the Orszag and Patterson 32^3 computation to today's largest simulation by Kaneda at 4096^3 [25], the latter has $\frac{4096^3}{32^3} = (2^7)^3 = 2^{21}$ times more data points at each realisation. As computing resources became more mainstream more calculations were done on homogeneous isotropic turbulence with periodic boundary conditions such as Siggia 64^3 (1981) [12], Kerr 128^3 (1985) [14], Jimenez et al 512^3 (1993) [26], and finally Kaneda 4096^3 (2004) [25].

3.4 Navier Stokes DNS

DNS can be defined simply as a computational method for calculating the solution to the complete Navier Stokes Equations in which all the length and time scales, including the smallest energy containing eddies are fully recovered without any turbulence closure model.

The home of DNS is still within the problem upon which it was created as a research tool. The current application of DNS in turbulence research has been in the realisation of the Navier Stokes equations solved for a finite Reynolds number up to a mesh size of 4096^3 on the Earth simulator, Japan. No one at

the time of writing has successfully run a 8192^3 simulation.

In a CFD toolbox you have the 'black box' commercial CFD packages, these are not freely available in academia, user computational models with various turbulent closure models and DNS. To reach cutting-edge Reynolds numbers only spectral methods can give high accuracy over large domains, commercial codes predominantly use finite difference, finite volume or finite element methods with no or little adaptivity and as such researchers use spectral or pseudo-spectral DNS.

To ensure the DNS is resolved the mesh spacing must be of the order of the Kolmogorov scale $\mathcal{O}(\eta)$ where $\eta = \left(\frac{\nu^3}{\epsilon}\right)^{1/4}$ that is, $\Delta x \sim \eta$ and only then will it be capable of resolving the smallest dynamically important scales of turbulence. However as $\eta \rightarrow 0$, $Re_L \rightarrow \infty$ hence the spatial resolution must be increased; $\Delta x \rightarrow \eta$ in order to resolve the smallest eddies.

Numerical discretization of the Navier-Stokes equations leads to the introduction of numerical errors. However, these errors can be predicted and controlled to provide reliable trustworthy results. The advantage over other models is avoiding the need for a turbulence closure model hence, removing any possible error introduced by forcing the flow at some arbitrary length scale or the appearance of non-physical effects propagating throughout the flow.

3D DNS calculations are typically computed in a cube, a simple set up is where the cube is periodic in all directions. As this periodic box grows, the number of variables at any given time grows by 2^3 for a factor of 2 refinement in each direction. The analysis and storage of large simulations is becoming increasingly difficult primarily due to the sheer volume of data outputted by a DNS code. For example a 2048^3 simulation requires approximately 2TB of physical disk space. This is too much data to try and process on a standard desktop. This makes the analysis awkward; to cope with large volumes of data researchers take the regions of interest within the flow and analyse these.

Currently high Reynolds number DNS simulations are not feasible, we would need a high resolution, 8196^3 or greater and currently this would only be achieved on a simple mesh. Typically, when a high Reynolds number simulation is required one would use RANS as is the case in formula one. Other intermediate methods can be configured to produce meaningful results; such as Large Eddy Simulations (LES) and Detached Eddy Simulations (DES).

3.4.1 CFL

The CFL condition was introduced in 1928 by Courant, Friedrich's and Levy. The condition is applied to ensure numerical convergence of hyperbolic partial differential equations. The dimensionless condition $\frac{\mathbf{u} \cdot \Delta t}{\Delta x} < C$ considers the ratio of the scalar product between the velocity u , and the time step Δt to the grid spacing Δx . The primary use of the CFL condition is in explicit time-marching schemes with a variable time step.

3.4.2 Velocity-Vorticity form of NSE

The velocity-vorticity form of the NSE is defined as:

$$\frac{\partial \mathbf{u}(\mathbf{x}, t)}{\partial t} = \mathbf{u}(\mathbf{x}, t) \times \boldsymbol{\omega}(\mathbf{x}, t) - \nabla \pi(\mathbf{x}, t) + \nu \nabla^2 \mathbf{u}(\mathbf{x}, t), \quad (3.4)$$

where $\nabla \pi$ contains the non linear term, and is obtained by taking the advection term to the left hand side, grouping it with the pressure and using the following vector identity $\nabla(\mathbf{u} \cdot \mathbf{u}) = 2\mathbf{u} \cdot \nabla \mathbf{u} + 2\mathbf{u} \times \boldsymbol{\omega}$.

$$\pi(\mathbf{x}, t) = \mathbf{p}(\mathbf{x}, t) + \frac{1}{2} (\mathbf{u}(\mathbf{x}, t))^2. \quad (3.5)$$

However, this equation is more useful in Fourier space. Calculating equation (3.4) in Fourier space simplifies the calculation and storage requirements of the simulation. To impose reality in physical space we must have: $\hat{\mathbf{v}}(-\mathbf{k}, t) = \hat{\mathbf{v}}^*(\mathbf{k}, t)$, here $*$ represents the complex conjugate and $\hat{\cdot}$ the Fourier transform. This approach halves the storage requirement as we only need to consider the positive contributions, due to symmetry. Furthermore the derivatives can be calculated exactly by multiplying by the wavenumber, whereas in physical

space we would need to use a discrete method to calculate the derivative. However the primary reason we take the Velocity-Vorticity form of the Navier Stokes equation over the original equation is that the advection term is difficult to compute in Fourier Space as it requires the computation of a convolution. To overcome this we use Fourier transforms.

3.5 Fourier Transformation

The analytic Fourier transform and its inverse for a complex periodic function with period 2π are defined as:

$$\hat{u}(\mathbf{k}) = \int_0^{2\pi} u(\mathbf{x}) e^{-i\mathbf{k}\cdot\mathbf{x}} d\mathbf{x} \quad (3.6)$$

$$u(\mathbf{x}) = \frac{1}{(2\pi)^3} \int_{-\infty}^{\infty} \hat{u}(\mathbf{k}) e^{i\mathbf{k}\cdot\mathbf{x}} d\mathbf{k} \quad (3.7)$$

Taking equation (3.4) and applying the Fourier transform, we find that the time derivative and Laplacian are trivial to transform, however the cross product is not.

$$\frac{\partial \hat{\mathbf{u}}(\mathbf{k}, t)}{\partial t} = \widehat{(\mathbf{u} \times \boldsymbol{\omega})}(\mathbf{k}, t) - \mathbf{k} \hat{\pi}(\mathbf{k}, t) - \nu \mathbf{k}^2 \hat{\mathbf{u}}(\mathbf{k}, t) \quad (3.8)$$

Taking the divergence of (3.4) and then applying the Fourier transform:

$$\nabla \cdot \widehat{(\mathbf{u} \times \boldsymbol{\omega})}(\mathbf{k}, t) = \mathbf{k} \cdot \mathbf{k} \hat{\pi}(\mathbf{k}, t), \quad (3.9)$$

$$\mathbf{k} \cdot \widehat{\mathbf{u} \times \boldsymbol{\omega}}(\mathbf{k}, t) = \mathbf{k}^2 \hat{\pi}(\mathbf{k}, t), \quad (3.10)$$

$$\hat{\pi}(\mathbf{k}, t) = \frac{\mathbf{k} \cdot \widehat{\mathbf{u} \times \boldsymbol{\omega}}(\mathbf{k}, t)}{\mathbf{k}^2}, \quad (3.11)$$

hence the Fourier transformed result is:

$$\frac{\partial \hat{\mathbf{u}}(\mathbf{k}, t)}{\partial t} = \hat{\boldsymbol{\alpha}}(\mathbf{k}, t) - \nu \mathbf{k}^2 \hat{\mathbf{u}}(\mathbf{k}, t) \quad (3.12)$$

Where:

$$\hat{\boldsymbol{\alpha}}(\mathbf{k}, t) = \widehat{\mathbf{u} \times \boldsymbol{\omega}}(\mathbf{k}, t) - \mathbf{k} \frac{\left(\mathbf{k} \cdot \widehat{\mathbf{u} \times \boldsymbol{\omega}}(\mathbf{k}, t) \right)}{\mathbf{k}^2} \quad (3.13)$$

So now we have (3.12) as the equation we integrate in the numerical model.

3.6 Pseudo-spectral Method

The approach taken here, is referred to as a pseudo-spectral method. The primary difference between this approach and spectral methods is the computational cost of the method. For instance if we compute a 1D Fourier transform completely in Fourier space we would need to undertake N complex addition and N complex multiplications, this gives a cost of N^2 , scaling this to three-dimensions gives a cost of N^6 . In real terms, if we have a finite element scheme we only need N^3 operations, so something that takes 10 hours to run would take 100 hours in a full spectral scheme. However computation of derivatives in spectral space is exact, and this offers significant improvement in accuracy but the increased accuracy of a spectral solver must be offset against the increased computational time cost.

The compromise is the pseudo-spectral method. We know that the linear parts are computed easily and relatively cheaply in Fourier space whereas they are time consuming and costly in physical space, the nonlinear term is particularly expensive to compute in Fourier space as it requires $\mathcal{O}(N^3)$ wave number operations, and a further $\mathcal{O}(N^3)$ sums at each wavenumber. The total cost of calculating the non linear term is $\mathcal{O}(N^6)$. This is a significant number of computations, in physical space however, one only needs to multiply the velocity with the velocity gradient. The compromise is to compute the linear terms in Fourier space and nonlinear terms in physical space with the help of a fast Fourier transform (FFT). The FFT costs $N \log_e N$ as opposed to the N^2 operations required in the 1D case; scaling this to 3D we require only $(N \log_e N)^3$ operations compared to N^6 previously required.

As such the pseudo-spectral method requires less computational time than a full spectral method with a greater level of accuracy when compared to a discrete method.

Chapter 4

Visualisation

4.1 Computational Data

Three 512^3 data sets were generated using Robert M. Kerr’s pseudo-spectral DNS code using periodic boundary conditions. The FORTRAN code is parallelised using MPI. Whilst at the University of Warwick I was fortunate enough to have access to Francesca, a 960 core high bandwidth, low latency Linux cluster with 1.92 TB RAM. For the primary simulations we requested 16 cores and 16GB of RAM, for the graphics output we saved the data at every eighth mesh point so that graphics could be produced on a desktop computer.

The three sets of data are named A, B and C. From these data sets we will perform our analysis. There are modest differences between A and B, run A was the benchmark simulation and run B was run at a lower viscosity than A but with the same initial condition to produce a higher Reynolds number flow. Finally C, was run by swapping the initial modes of the first initial condition used in A and B to produce a different initial condition. Note that the pseudospectral method truncates a third of the wavenumbers in each direction.

The calculations were completed on a $[0, 2\pi]^3$ computational domain with periodic boundary conditions in each direction with $512 \times 512 \times 512$ mesh points. The key points of interest about each simulation are summarised table 4.1.

Variable	Simulation		
	A	B	C
Grid Resolution	512^3	512^3	512^3
L	2π	2π	2π
ν	0.0125	0.003125	0.0125
R_λ	110	380	115
η	0.0242	0.0107	0.0245
λ	0.499	0.411	0.514
k_{max}	45	141	46

Table 4.1: This is a table of key quantities taken from calculations A, B and C.

4.1.1 Energy Spectra

Energy spectra provide a useful comparison between numerical isotropic homogeneous turbulence and turbulence theory. We concern ourselves with the inertial sub range, within this range one would expect to see a $k^{-5/3}$ regime. This is observed for the later times in figures 4.1, 4.2 and 4.3. The $k^{-5/3}$ regime stems from Kolmogorov’s first universality assumption, which states that at very high, but not infinite Reynold’s numbers, all the small-scale statistical properties are uniquely and universally determined by the integral scale l , the mean energy dissipation rate ϵ and the viscosity ν [27]. The Kolmogorov scale is the size of the smallest resolved scale in a turbulent flow defined as:

$$\eta = \left(\frac{\nu^3}{\epsilon} \right)^{\frac{1}{4}}. \quad (4.1)$$

The energy spectrum of the inertial subrange is defined as:

$$E(k) = \alpha \epsilon^{2/3} k^{-5/3}. \quad (4.2)$$

In runs A and B a smooth initial condition is studied, the initial energies are:

$$E(k, 0) = 0 \quad k \geq 4, \quad E(k, 0) = C \quad k < 4 \quad (4.3)$$

This is the same initial condition as used in Herring and Kerr [28]. To generate Run C the odd and even modes were swapped to give the same initial

energy spectrum as run A as seen in figure 4.3. The viscosities were set at $\nu = 0.0125, 0.003125, 0.0125$ for runs A, B and C respectively.

Figures 4.1, 4.2 and 4.3, show the normalised three dimensional kinetic energy spectrum across the simulation time span. All three simulations exhibit the behaviour expected for a well resolved simulation, they have an exponentially decaying tail and at the high wave numbers there is no or negligible turn up. At intermediate wavenumbers all tend towards a $k^{-5/3}$ energy spectrum at late times, with dataset B, the larger Reynolds number case, overshooting the $-5/3$ expectation more than the others.

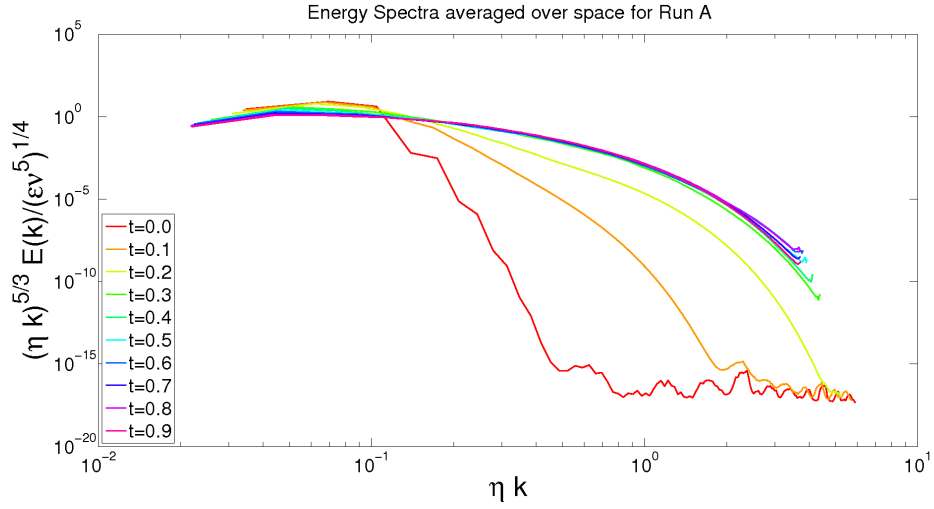


Figure 4.1: Three-dimensional kinetic energy spectra for simulation A, normalised by the Kolmogorov microscale and multiplied by $k^{5/3}$, $R_\lambda = 256$ at $t = 0$.

4.2 Energy Transfer

From equation (3.12) an equation for the kinetic energy transfer can be derived. Grouping the linear terms to the LHS and the non linear terms to RHS. We obtain the kinetic energy transfer function $T(k, t)$, this contains all the non

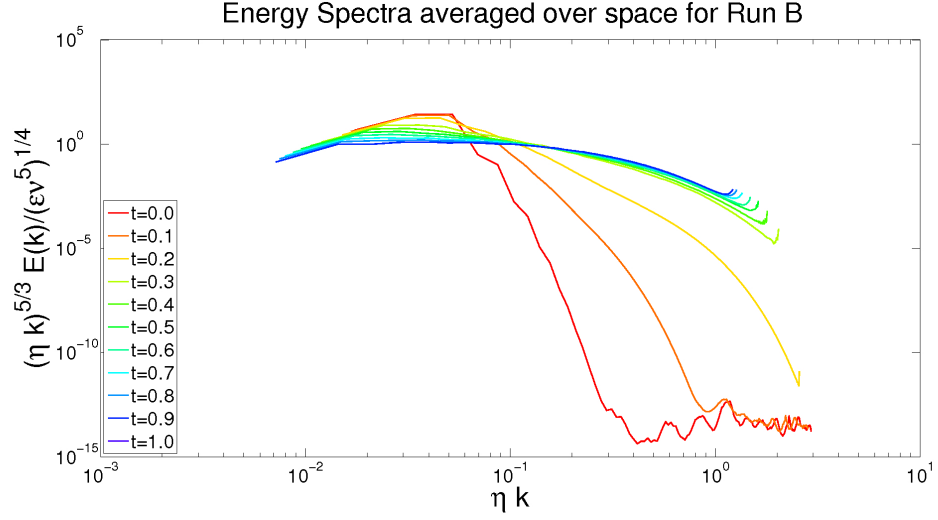


Figure 4.2: Three-dimensional kinetic energy spectra for simulation B, normalised by the Kolmogorov microscale and multiplied by $k^{5/3}$, $R_\lambda = 1018$ at $t = 0$.

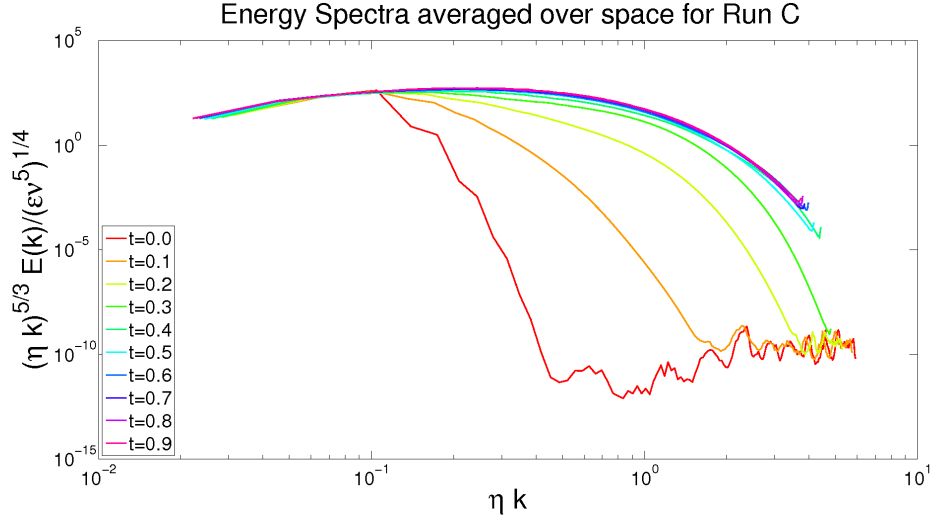


Figure 4.3: Three-dimensional kinetic energy spectra for simulation C, normalised by the Kolmogorov microscale and multiplied by $k^{5/3}$, $R_\lambda = 256$ at $t = 0$.

linear terms and their associated interaction:

$$\left(\frac{\partial}{\partial t} + 2\nu k^2 \right) E(k, t) = T(k, t). \quad (4.4)$$

The derivation of equation (4.2) can be found in [29]. This equation is analogous to the physical space Karman-Howarth equation. $T(k, t)$ is a useful function, it allows the flow of energy through the wave numbers to be visualised. At low wavenumbers $T(k, t) < 0$, and at high wavenumbers $T(k, t) > 0$, it can be shown that large-scale energy is removed and passed down to the small scales, so that the integral $\int_0^\infty T(k, t) dk = 0$, this shows that the nonlinear term conserves energy as it is transferred across scales, leading to the energy balance equation:

$$\frac{d}{dt} \int_0^\infty E(k, t) dk + 2\nu \int_0^\infty k^2 E(k, t) dk = 0. \quad (4.5)$$

In figure 4.4 we observe the expected behaviour by comparing the energy transfer spectra of calculations A, B and C for all times. For intermediate times transfer moves through spectrum towards high wavenumbers in a coherent manner, with the negative part extracting energy from the low wavenumbers and the positive part at the high wavenumbers accepting this energy before it is dissipated by viscosity.

4.2.1 Global Time Evolution Diagnostics

This subsection shows the time evolution of the dissipation, skewness, maxima of vorticity, Kolmogorov scale and Taylor microscale Reynolds number.

The pseudo-spectral code uses a third order Runge-Kutta method for time advancement, the variable step size is obtained through the use of the CFL condition set to 1.5. The CFL condition requires that the ratio of velocity and time step to the mesh size remains constant. This is illustrated in figure 4.10 showing that as the Kolmogorov scale η decreases, the variable time step Δt does as well.

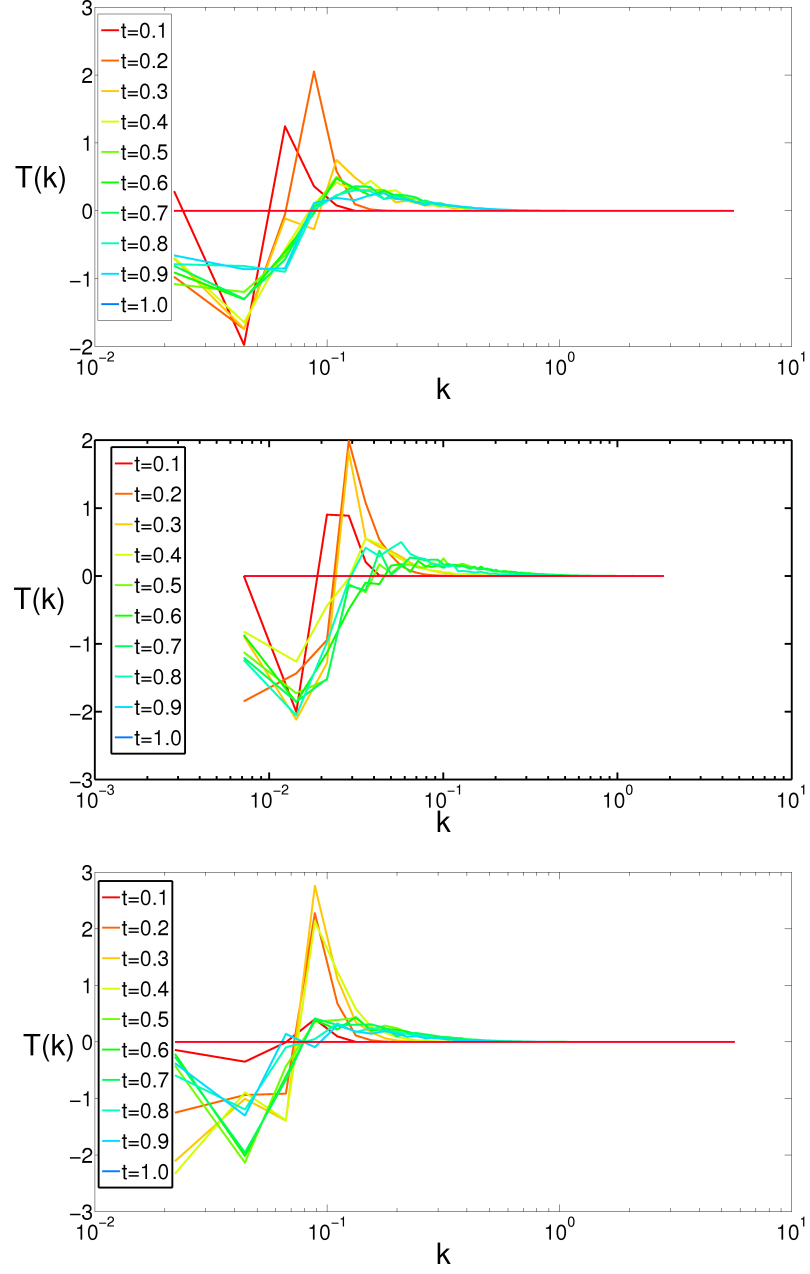


Figure 4.4: Transfer function of three dimensional turbulence as calculated for calculation A(top), B(middle) and C(bottom) over $t=0.1$ to $t=0.9$ in 0.1 increments.

4.2.2 Maximum of Vorticity

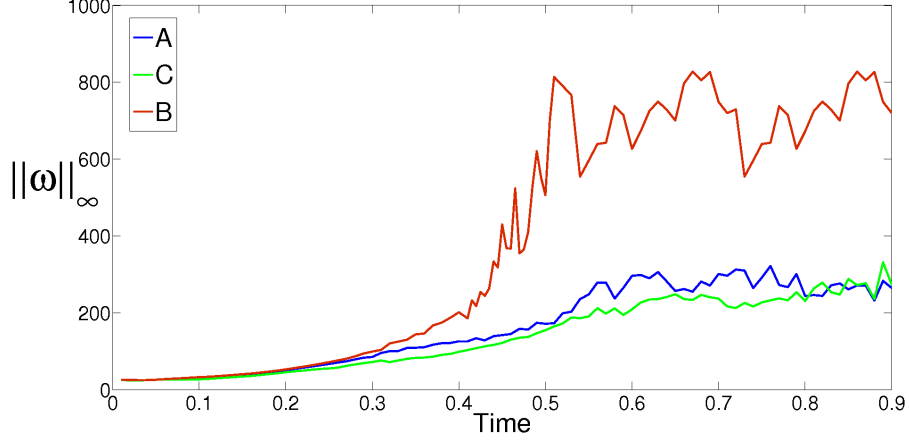


Figure 4.5: The time dependence of maximum vorticity $||\omega||_\infty$ growth for simulations A, B and C.

In figure 4.5 the time dependence of maximum vorticity has been plotted. The maximum vorticity $||\omega||_\infty$ is the L^∞ norm of the vorticity:

$$||\omega||_\infty = \max\{|\omega_1|, |\omega_2|, \dots, |\omega_n|\}. \quad (4.6)$$

Here we observe steady growth in the region $T < 0.4$ before an abrupt increase in the growth of $||\omega||_\infty$ until the first peak at $t \approx 0.5$ for simulation B. This is consistent with what was observed by Holm and Kerr [30].

4.2.3 Dissipation

The dissipation ϵ for homogeneous turbulence can be defined in terms of the strain tensor S and the viscosity ν , $\epsilon = \nu \int S_{ij} S_{ij} dV$. We already know that the energy is transferred between the scales from figure 4.4, how would one expect the dissipation to behave?

In a typical cascade the large scale motions transfer energy to the small scales, leading to a significant growth in the dissipation. Eventually the dissipation saturates. The dissipation growth is illustrated in figure 4.6

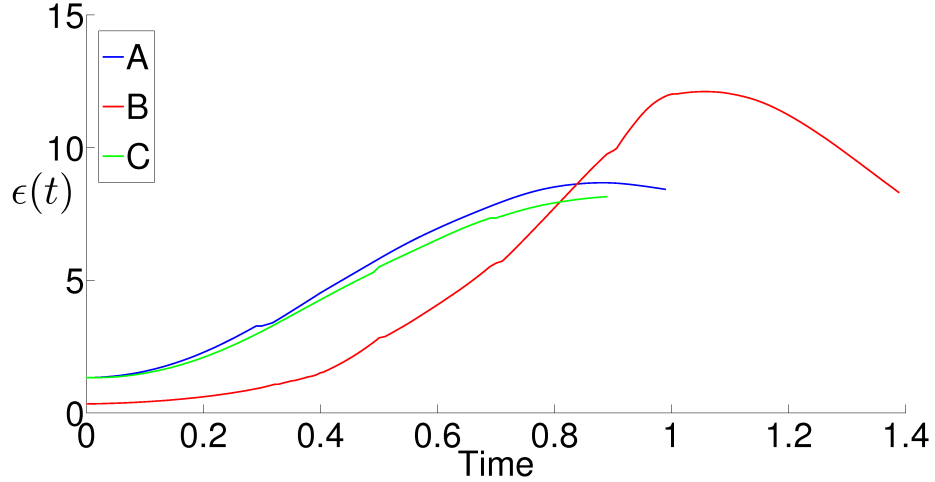


Figure 4.6: The dissipation growth for simulations A, B and C.

Simulations A and C exhibit very similar rates of change with both simulations appearing to reach the same saturation level around the same time. This is reassuring, however we needed to run simulation B slightly longer as it has not quite reached its peak at $t = 1.0$, however the curve does level out and is as expected. Similar growth in energy dissipation is seen for a Taylor-Green vortex at multiple Reynolds numbers in [27].

Skewness

A quantity we have yet to discuss is the velocity derivative skewness S_k . The Skewness is defined as:

$$S_k(t) = \left\langle \left(\frac{\partial u}{\partial x} \right)^3 \right\rangle \left\langle \left(\frac{\partial u}{\partial x} \right)^2 \right\rangle^{-3/2}. \quad (4.7)$$

The Skewness factor for fully developed turbulence has been found to be 0.5, shown experimentally in [31] and numerically using DNS by Kerr [14]. Further to these works Q. Jian [32] examined the asymptotic limit of equation (4.7) with R_λ dependence showing that as $R_\lambda \rightarrow \infty$, $S = 0.515$. With these three results in mind; it is reassuring observe this behaviour in figure 4.7. Kerr [28] notes that as $S_k \rightarrow 0.5$, the enstrophy continues to grow and the dissipation

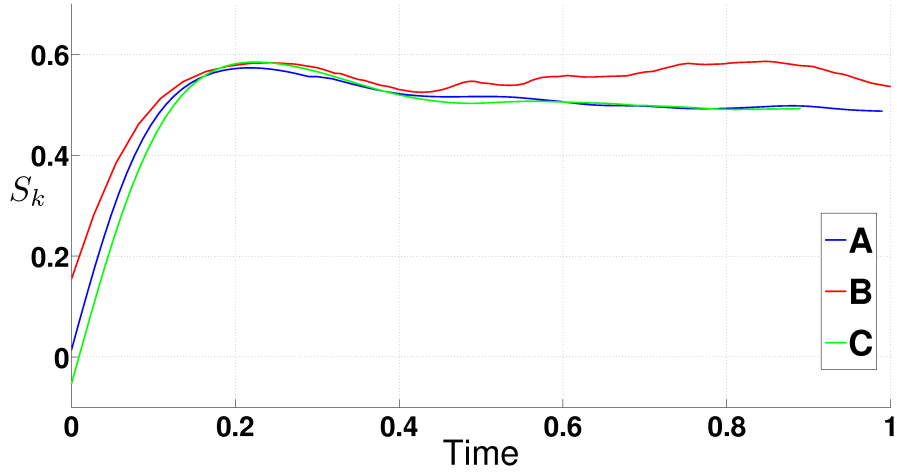


Figure 4.7: The Skewness factor evolution is plotted for simulations A, B and C. The expected behaviour of $S_k \rightarrow 0.5$ is observed once the turbulence is fully developed [31] and [14].

increases to its saturation level and it is during this time that the vortex tubes start to appear.

4.2.4 Reynolds Number

In figure 4.8, the evolution of the Taylor Reynolds number is plotted. The Taylor Reynolds number $Re_\lambda = \frac{u\lambda}{\nu}$, drops off as $t \rightarrow T_{max}$, the reason for this, is the growth of the dissipation $\epsilon(t) < \epsilon(T_{max})$. It is well known that $\lambda^2 = 15\nu u^2 \epsilon^{-1}$. Since λ is dependent on the inverse dissipation, as the dissipation increases one would expect to see a drop in λ for fixed ν and u . The velocity field u is increasing but the rate of velocity growth is insufficient to counteract ϵ^{-1} hence the reduction in Re_λ as the flow develops.

4.3 Flow Visualisation

The following graphics are produced using the VisIt Visualisation Tool, this is an open source visualisation package developed by Lawrence Livermore National Laboratory. This is a very powerful visualisation tool, provided you have your data in a readable format. The format chosen was the visualisa-

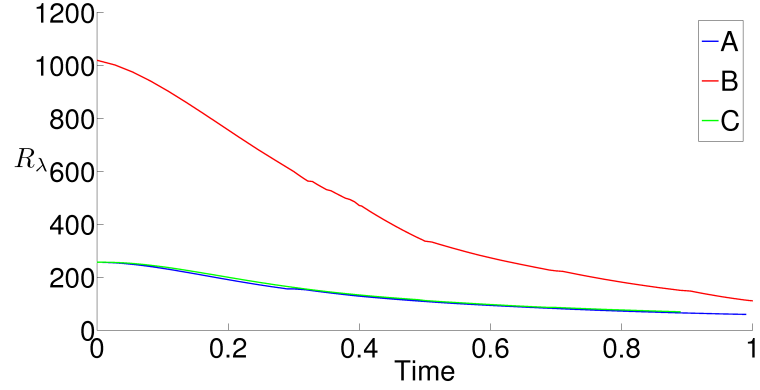


Figure 4.8: The evolution of the Taylor Reynolds number Re_λ for simulations A, B and C across all times.

tion toolkit (VTK) format, this legacy format is very simple to use, and was achievable with only minor output amendments to the pseudo-spectral code. We needed to output a header and data file from the graphics output routine and then we generate any scalar, vector or tensor to be read in to VisIt. Additionally, the VTK format chosen has the option of a rectilinear grid, this fits the method in which the data is saved perfectly. The data is saved plane by plane along the vertical axis. The next step was to write some code that quickly pulls together the various components so that I can visualise the velocity and vorticity fields or indeed any other surface of interest.

The evolution of the five turbulence invariants and their associated interaction is of interest. We will consider the velocity field and then discuss the isosurfaces of vorticity and strain including their interaction before considering the evolution of the third order moments, the enstrophy and dissipation production.

The motivation behind visualising the fluid flow is the identification of areas of intense activity and their evolution. The development of significant events and subsequent dissipation within the flow field can be observed. These structures are called *Coherent Structures* and are defined as follows: 'A coherent structure is a connected, large-scale turbulent fluid mass with a phase-correlated

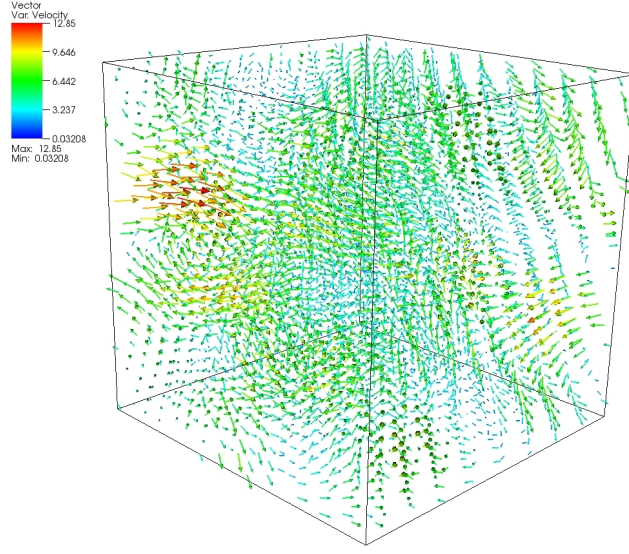


Figure 4.9: This is the Vector field of simulation B at $t=0.3$, here we considered a 5000 point subset of the entire flow field, the velocities range from 12.85 (red) to 0 (blue). The vectors are scaled by magnitude. On its own the velocity field does not provide any noteworthy features of the flow other than the scale of velocities contained within the flow.

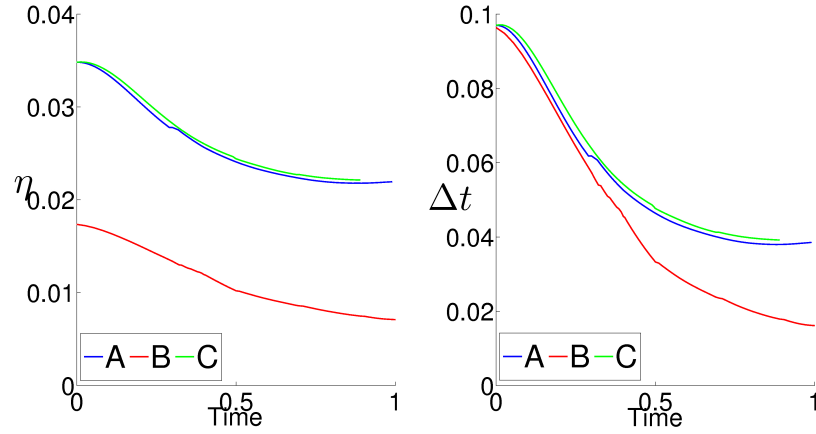


Figure 4.10: The ratio between the spatial and temporal discretization should be in approximate balance to reduce the likely hood of numerical artefact's populating the flow. The reduction in the Kolmogorov microscale η is plotted (left) and the reduction time stepping Δt is plotted (right)

vorticity over its spatial extent' [33].

Figure 4.9 shows that velocity is not a strong indicator of coherent structures, but it does provide an overview of regions that are possibly connected. Note that in a periodic boundary condition there are no boundaries.

Whilst the velocity field is not best suited for this type of analysis, we can pose the questions: what quantities could possibly provide additional insight into turbulent flow? The strain and vorticity are obvious contenders for further investigation. Since they are simply the symmetric and antisymmetric components of the velocity gradient tensor and as such the dynamics of three-dimensional turbulence are governed by their interaction. One example of vorticity strain interaction is the preferred alignment of the vorticity with the intermediate strain eigenvalue as discussed in [4] and [14]. Hence the structures one would expect to observe include tubes, sheets, vortex rings and perhaps structures typically found in shear and channel flows such as hairpin vortices [34].

Figure 4.11 shows regions of low vorticity that are locally connected by isosurfaces, with intense vorticity regions within them. To obtain more detail figure 4.12 overlays a velocity field on top of single contours of the vorticity and strain.

Another possible method of visualising these surfaces would be to take a slice through the vorticity isosurfaces and consider a single plane of isosurfaces and the relationship between the velocity field and the isosurfaces as shown in figure 4.13. Again if we slice through the domain of isosurfaces and select a couple of planes we can overlay the vorticity streamlines as seen in figure 4.14.

In figure 4.13 there is a cross section of the vorticity isosurfaces with the velocity field overlaid, taken from simulation B, at $t = 0.9$. At this instant there is significant motion in the upper left quadrant with regions of maximum velocity and vorticity. We have seen that the vorticity isosurfaces show clear twisting and interaction within local regions of the flow, and that these regions are linked to other regions of major change within the velocity field. Can we

learn anything from the distribution of strain isosurfaces for the same flow? The surfaces of the vorticity are 'tube' like, whereas in figure 4.15 the regions of intense strains are a lot more localised and 'pancake' like which suggests a sheet formation at the lower values of strain.

The interaction between the vorticity and strain is interesting, we see that the vorticity is largely expressed as tube like structures whereas the strain is starting to look more sheet like. Something that would be interesting to consider is whether within a larger simulation, especially with the resources now generally available to researchers whether the development, motion, evolution and final dissipation of these interactions can be probed further. The current understanding suggests that as a turbulent cascade forms, the dominant structures are a result of the dominance of strain within the flow, leading to the formation of vortex sheets with strong shears. Eventually vortex tubes form from these sheets that after $t = 0.5$ dominate the flow. This would be an interesting area of further study.

The third order moments R_ω and R_S and their interaction are now of interest. Consider figure 4.16 there are regions of significant interaction between the two moments, highlighted by slicing through one of the planes. Tsinober makes a valid point in [35], where he explores the role R_ω has on opposing the production of dissipation, and it was mentioned in Tsinober et al [36], [37] "that the production of strain/dissipation occurs only because of the term $-s_{ij}s_{jk}s_{ki}$, since $\langle -R_S \rangle = \frac{3}{4} \langle R_\omega \rangle$ and $\langle s_{ij} \left(\frac{\partial^2 \mathbf{p}}{\partial x_i \partial x_j} \right) \rangle = 0$ ". Although not entirely clear from figure 4.16, Tsinober's observations appear true, in the regions where enstrophy production exists the structure of the dissipation production appears less dominant.

4.4 Summary

In this chapter we compared the calculations to what has been done before, and observed the explicit behaviour that is expected namely:

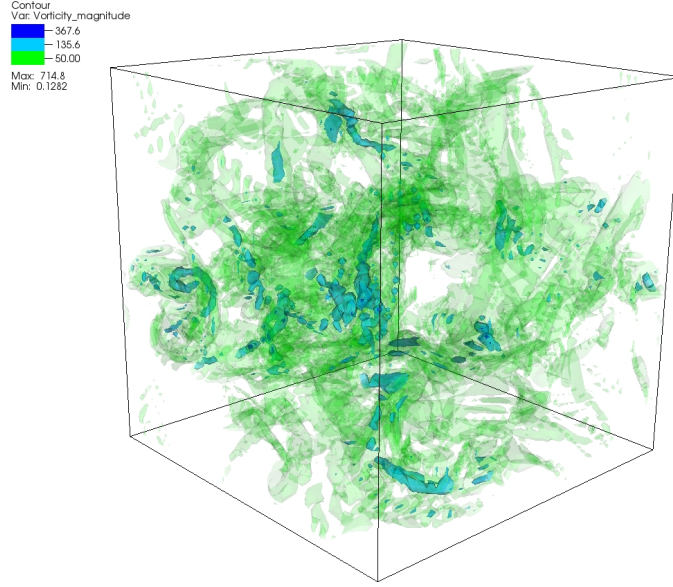


Figure 4.11: This figure considers the isosurfaces of vorticity from simulation B at $t=0.8$, $R_\lambda = 380$. The vorticity is conditioned on regions of low (green $|\omega| \approx 50$), medium (light blue $|\omega| \approx 135$) and high (blue $|\omega| \approx 370$) vorticity with the lower isosurfaces partially transparent to see the interior flow.

- We observed a region of $k^{-\frac{5}{3}}$, for the decay of the energy spectra for all simulations.
- The Energy spectra has shown that all simulations are well resolved.
- The expectation that $\int_0^\infty T(k, t) dk = 0$, is shown in Figure 4.4.
- The tendency for $\lim_{t \rightarrow \infty} S_k = 0.5$, is observed in all simulations.
- The Taylor microscale R_λ , collapses as the energy transfer moves the energy into the small scales.

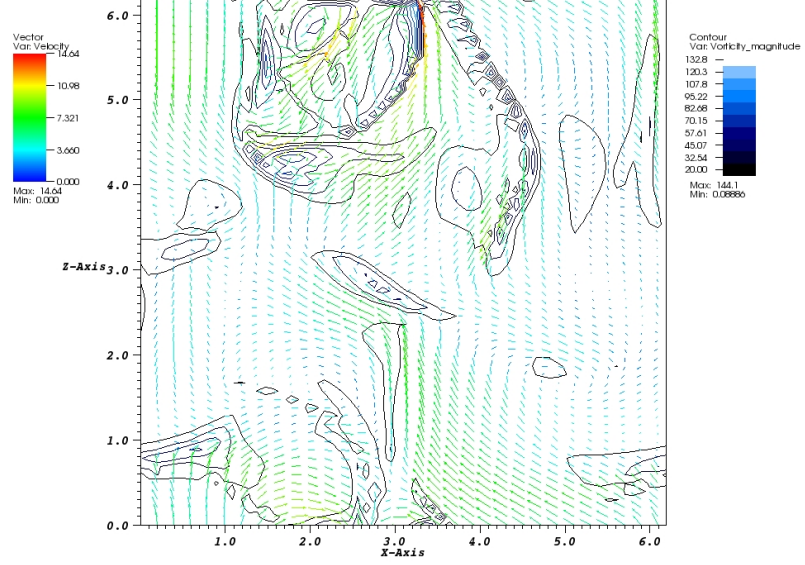


Figure 4.12: A slice through the isosurfaces of vorticity from simulation B, $R_\lambda = 380$ at $t = 0.8$. The vorticity is conditioned on regions of low(black $|\omega| \approx 20$), medium (blue $|\omega| \approx 20$) and high (pale blue $|\omega| \approx 130$) vorticity with the regions of high vorticity held within the intermediate structures. For clarity the velocity field have been overlaid with values ranging from 15 (red) to 0 (blue).

- Checked that the balance between the spatial and temporal discretization is as expected.
- Considered the visualisation of the velocity field, and how we can make use of visualisations to discuss expected behaviour within the flow.
- Looked at the isosurfaces of vorticity and strain and their interaction.
- We also looked at whether anything could be obtained from considering the interaction between the third order moments.

From these observations we can say that the simulations are of sufficient resolution, and sufficient correlation has been drawn with previous

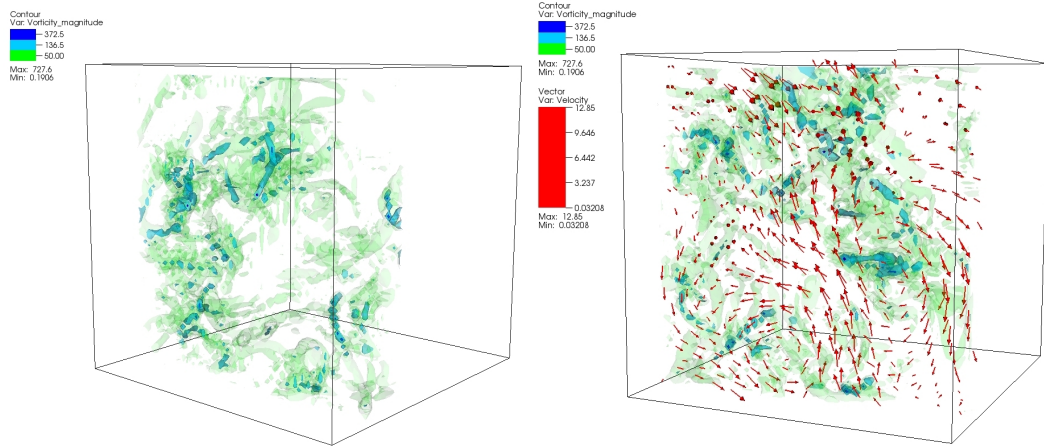


Figure 4.13: Here we have taken a slice through the volume of vorticity iso-surfaces at $t=0.9$ from simulation B (left), here the vorticity is conditioned on regions of low (green $|\omega| \approx 50$), medium (light blue $|\omega| \approx 135$) and high (blue $|\omega| \approx 370$) vorticity. The velocity field was then overlaid using a single colour - red (right)

experimental work with expected behaviour seen. We are going to use this data to perform an analysis on the velocity gradient tensor to discuss the velocity moments in a pre-turbulent state.

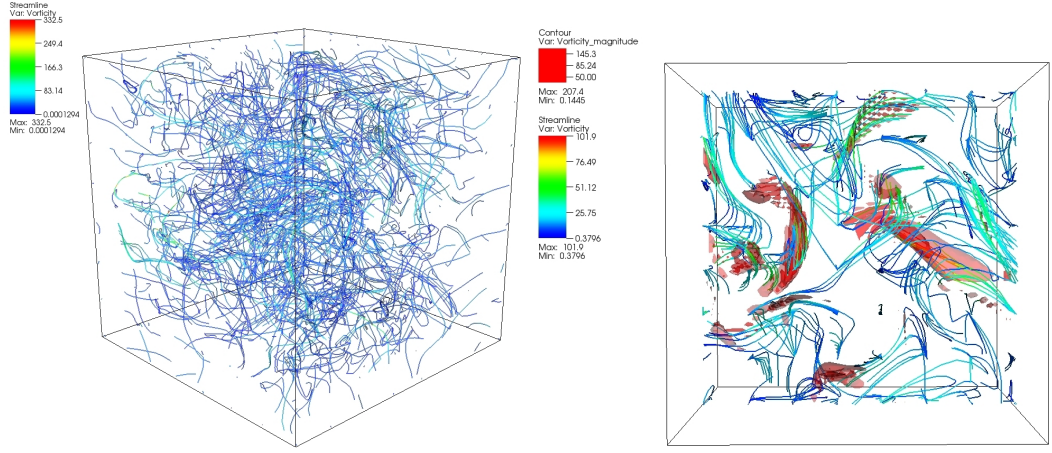


Figure 4.14: The left image shows the vorticity streamlines at $t=0.6$ from simulation B, the vorticity ranges from 332.5(red) to 0(blue). The right image is a slice through the vorticity isosurfaces with the vorticity streamlines overlaid, in this subsection the vorticity magnitude(red) ranges from 207 to 0 and the streamlines range from 102(red) to 0(blue).

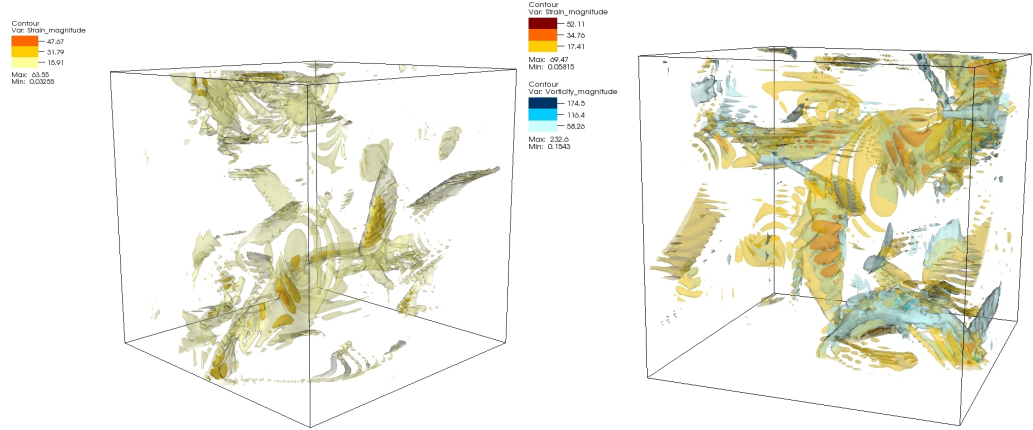


Figure 4.15: The left image shows the isosurfaces of the strain at $t=0.4$, the strain is divided into three regions orange, yellow and pale yellow with mid-values 47.67, 31.79 and 15.91 respectively. The right image looks at the interaction between vorticity(blue) and the strain(orange). The vorticity has been divided into three regions with midpoints 174.5 (blue), 116.4(light blue) and 58.26 (pale blue), similarly the strain has regions 52.11(red), 34.76(orange) and 17.41(yellow).

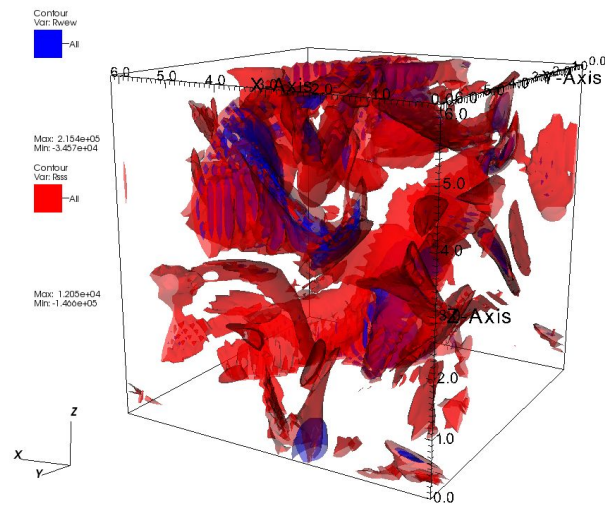


Figure 4.16: This is a representation of the isosurfaces of the enstrophy (blue) and dissipation (red) production terms.

Chapter 5

Validation

Whilst the Restricted Euler (RE) model has been a useful tool for discussing the evolution of certain moments of the velocity gradient tensor, its main defect is that it neglects the effects of the full pressure Hessian. The current goal is to investigate the effect the full pressure Hessian has on the R-Q phase space taken from a developing turbulent flow field by comparing how the true velocity moments develop and interact with each other in the RE model predictions. To do this, we begin by integrating the Vieillefosse equations (2.29), then move on to discuss the DNS calculations.

5.1 RE Validation One

How would you choose initial conditions for the set of RE ordinary differential equations that would be relevant to the direct numerical simulation? By scaling the RE it can be seen that all the terms, taken so that their dimensional units are 1/time, should go as $(T_c - t)^{-1}$ for some critical time T_c . This has already been found by [4] and [38], so the question that needs to be answered before the full Hessian analysis is done is how rapidly the individual terms of the RE relax to that state. Therefore, one wants an initial condition that is far from the predicted final state as possible.

The first question considered is how rapidly the full R and Q terms relax to zero. This is expected because, due to the periodic boundary conditions, the averages of R and Q over a true flow should be zero, even if at individual points they are not. Therefore, one wants to see how an initial condition with $R \neq 0$ and $Q \neq 0$ relaxes. Figure 5.1 confirms as $t \rightarrow T_c$ that $R = Q = 0$, that is $R_S = -(4/3)R_\omega$ and $S^2 = 0.5\omega^2$.

5.2 RE Validation Two

With this test passed, it is important to see how other RE terms, or combinations of terms, relax. Some of these combinations do not relax immediately to the asymptotic state. This is important because it could provide a partial explanation for their non-asymptotic values in real flows. The four frames in Figure 5.2 look at some of these terms, or combinations.

Notice how in the upper two frames in Figure 5.2, the ratio at which the second and third order moments approach zero is remarkably close. The normalised moments behave as expected, with the normalised triple strain and normalised vortex stretching both approaching zero with a zero net effect as would be expected for R as shown in the lower left frame. If we take this further and consider the ratio minus the expected limit we should get two plots that approach zero in the finite time limit in the lower right frame. This is consistent with the discriminant $D = \frac{27}{4}R^2 + Q^3 = 0$.

5.3 Probability Distributions

In Kerr 1985 [14] it is noticed that there is an alignment between the vorticity and strain, however it was not until two years later when this alignment was refined to discuss the particular behaviour of intermediate

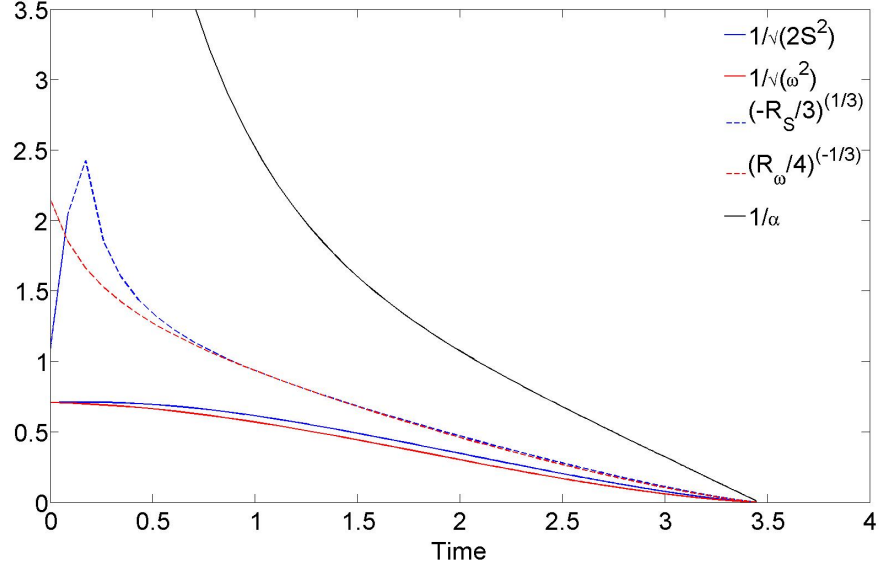


Figure 5.1: Confirming the constraint that R and Q should be zero over the entire flow. Other moments are included for completeness.

eigenvalue. Typically denoted by s_2 this middle eigenvalue from the ordered set $s_1 < s_2 < s_3$ can be normalised as follows:

$$\beta = \sqrt{6} \frac{s_2}{|\mathbf{S}|}, \quad |\mathbf{S}| = s_1^2 + s_2^2 + s_3^2 \quad (5.1)$$

There is preferred alignment between the vorticity and the intermediate eigenvalue when it is shown that the ratio of the strain eigenvalues is 3:1:-4 [4]. The normalised triple strain correlation is defined as [39]:

$$S_N^3 = \sqrt{6} \frac{\mathbf{R}_S}{|\mathbf{S}|^3}. \quad (5.2)$$

This can be expressed in terms of β :

$$S_N^3 = -\frac{1}{2}\beta(3 - \beta^2). \quad (5.3)$$

In figures 5.3 and 5.4 the probability distribution functions of the triple strain correlation and β are plotted for the full domain and the region

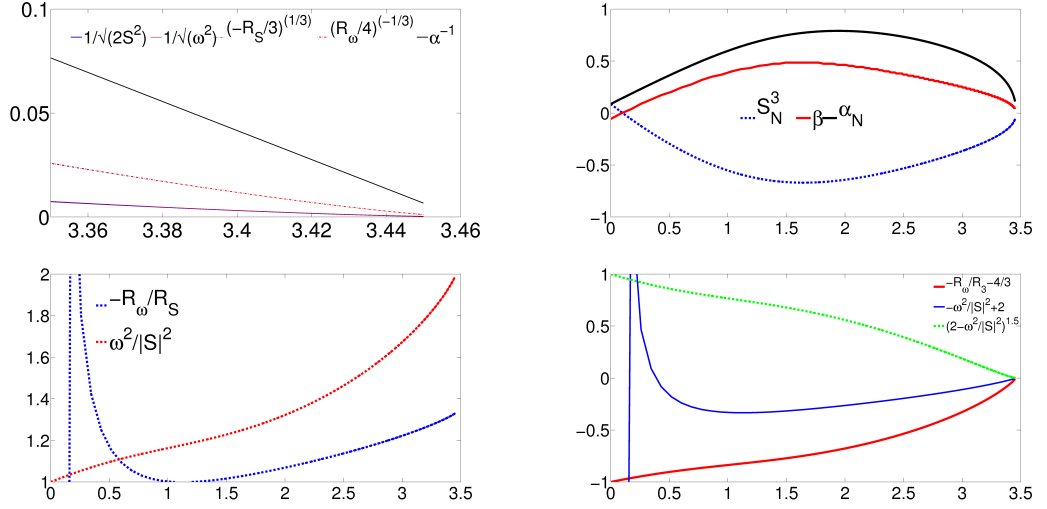


Figure 5.2: In all cases the x axis is time. Upper left: close-up of Figure 5.1 showing the linear approach to zero of these inverses. $\alpha^{-1} = \omega^2/R_\omega$, $(-R_S/3)^{-1/3}$, $(-R_\omega/4)^{-1/3}$, $(S^2)^{-1/2}$ and $(\omega^2)^{-1/2}$. Upper right: Normalised components: $\alpha_N^{-1} = \omega^2/R_\omega$, β and S_N^3 using equation (5.3). Lower left: ratio between the two second ω^2/S^2 and two third order moments, $-R_\omega/R_S$ respectively. As expected, the second order moments approach 2 as the singular time is reached and the third order moments approach $\frac{4}{3}$. Lower right: The ratio between the moments is considered again and this time we include a term analogous to Q , $(2 - \omega^2/S^2)$. The behaviour seen is exactly as expected with the two ratios $(-\omega^2/S^2 + 2)$, $-R_\omega/R_S - 4/3$ and the new term $(2 - \omega^2/S^2)^{1.5}$ approaching zero in the singular limit.

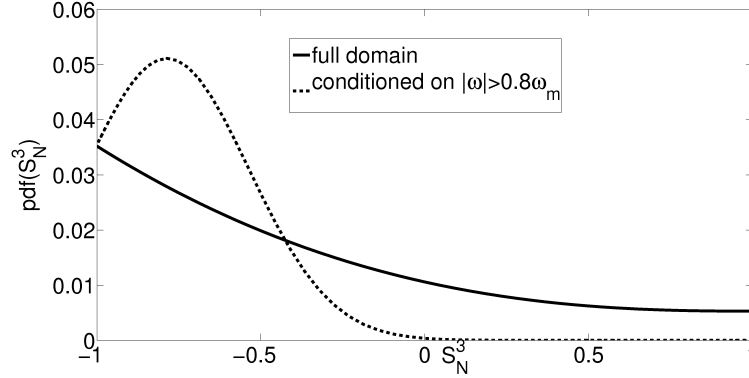


Figure 5.3: Typical probability distributions of the normalised triple strain S_N^3 in the full domain and conditioned on the region of maximum vorticity, provided by R M Kerr.

of maximum vorticity. The peak in the β distribution is noted at 0.5 in figure 5.5, with the inset image showing S_N^3 as calculated in terms of β .

5.4 R-Q Phase Space

When discussing the R-Q phase space the typical expectation is that the classic teardrop can be reproduced, this is shown in figure 5.6. The development of the flow up until the singularity is of particular interest, and the goal would be to explore whether the distribution of particular velocity moments can help explain the local flow characteristics. We know that R_S and R_ω approach zero as we approach the singular time, this is an unphysical effect of the Vieillefosse model as this behaviour is not observed within a turbulent flow.

5.4.1 Conditioned Distributions

The R-Q plane has been studied extensively over the last few years, with focus on providing a more sophisticated closure that has a significant computational benefit over full DNS and other CFD methods. Historically, the most common method of illustrating distributions in numerical simulation was to use probability density functions, however

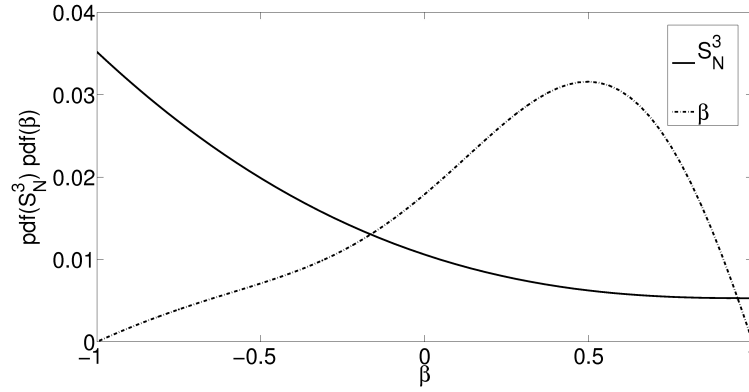


Figure 5.4: This is the probability distribution of both β and S_N , the intersection is of interest as it allows us to consider the balance between the third order moments R_ω and R_S , provided by R M Kerr.

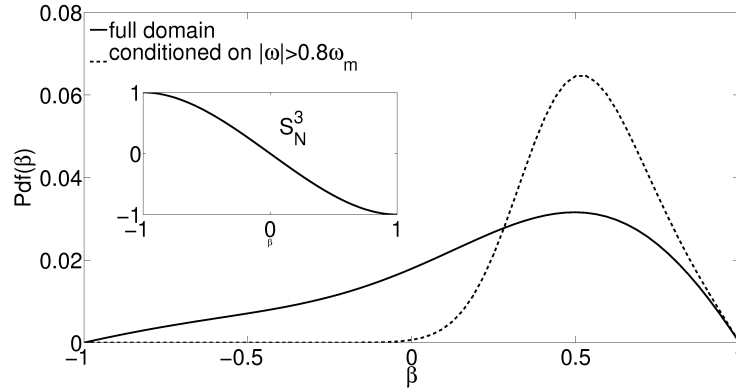


Figure 5.5: Typical probability distributions of the normalised β including β conditioned on the region of maximum vorticity, provided by R M Kerr.

the R-Q plane's prominent tear drop is best discussed through the use of Jackson Pollock style scatter plots. Scatter plots have been produced that highlight the regions of low to high intensity for each moment of interest in figures 5.7 to 5.12. Frames on the left and right show where in the R-Q plane different limits are located, with the central figure combining them.

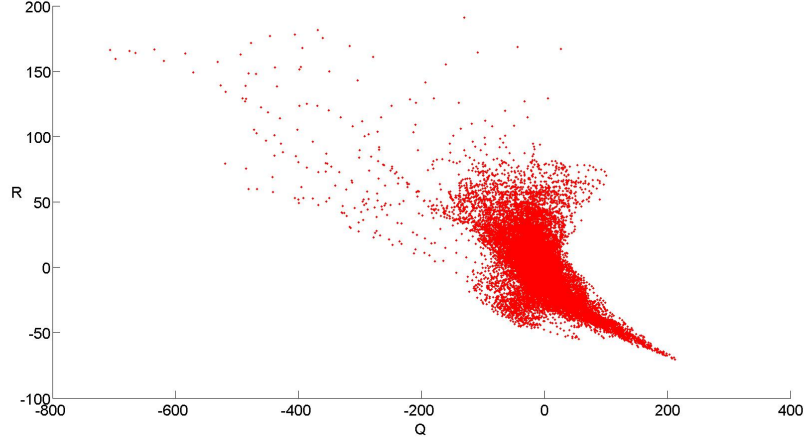


Figure 5.6: The typical R-Q teardrop characterised by R and Q , without breaking down the terms, from $t = 0.5$ from simulation A

Enstrophy

Figure 5.7 shows the R-Q plane with the regions of various levels of enstrophy production at three intervals, long after the peaks in the velocity derivative skewness in figure 4.7 and during the period when the flow is relaxing to statistics characteristic of fully-developed turbulence. What we see is that the region of maximum vorticity is somewhat diminished when compared to the earlier times, and most of the points associated with the tear drop, with a short tail on the $R = -(4/27)Q^3)^{1/2}$ asymptote, associated with low to intermediate values of the enstrophy production (blue and light blue).

Dissipation

Figure 5.8 shows the R-Q plane with the regions of various levels of dissipation. In the early stages the maximum dissipation acts throughout the flow with even proportion above and below the line $Q = 0$, however as the flow becomes increasingly more established the dissipation seeks to act along the Vieillefosse discriminant line.

Enstrophy Production

Figure 5.9 considers the enstrophy production. Here we see that the regions of intermediate enstrophy production align themselves along the asymptote with the region of maximum production remaining in the upper right hand quadrant. This is hardly surprising as we have already seen the preference of vorticity to sit within the same region.

Dissipation Production

Figure 5.10 shows the distribution of the dissipation production within the R-Q plane. The regions of intense negative strains are prominent along the asymptote with the bulk of the zero values around the centre with no real preferred reference. This behaviour is seen through the development of the turbulence.

I_4

The rotational invariant $I_4 = (\omega S)^2$ as seen in figure 5.12 sites primarily around the central flow field, however if we were to consider the upper half of the ranges it appears that as the flow develops the regions of upper intensity sit on the edges of the tear drop rotating round from regions of high dissipation to maximum vorticity. Which is not infeasible as the dissipation initially dominates the flow, whilst the vorticity grows and as such we may expect to see the observed behaviour of I_4 .

α

Figure 5.11, and the earlier times show no real change in the regions of vortex stretching, with the region of maximum vortex stretching being within the region of high dissipation.

5.5 Summary

Here we have considered how quickly the RE terms reach the critical time through direct integration, before discussing how the other terms relax to that state. We found that the behaviour we observed was as expected [4] and [38]. Finally, we considered the effects of the Vieillefosse equations and their subsequent evolution using DNS. We want to investigate the role the pressure Hessian has on a developing turbulent flow and whether any new conclusions can be drawn from its study, leading us to Chapter 6.

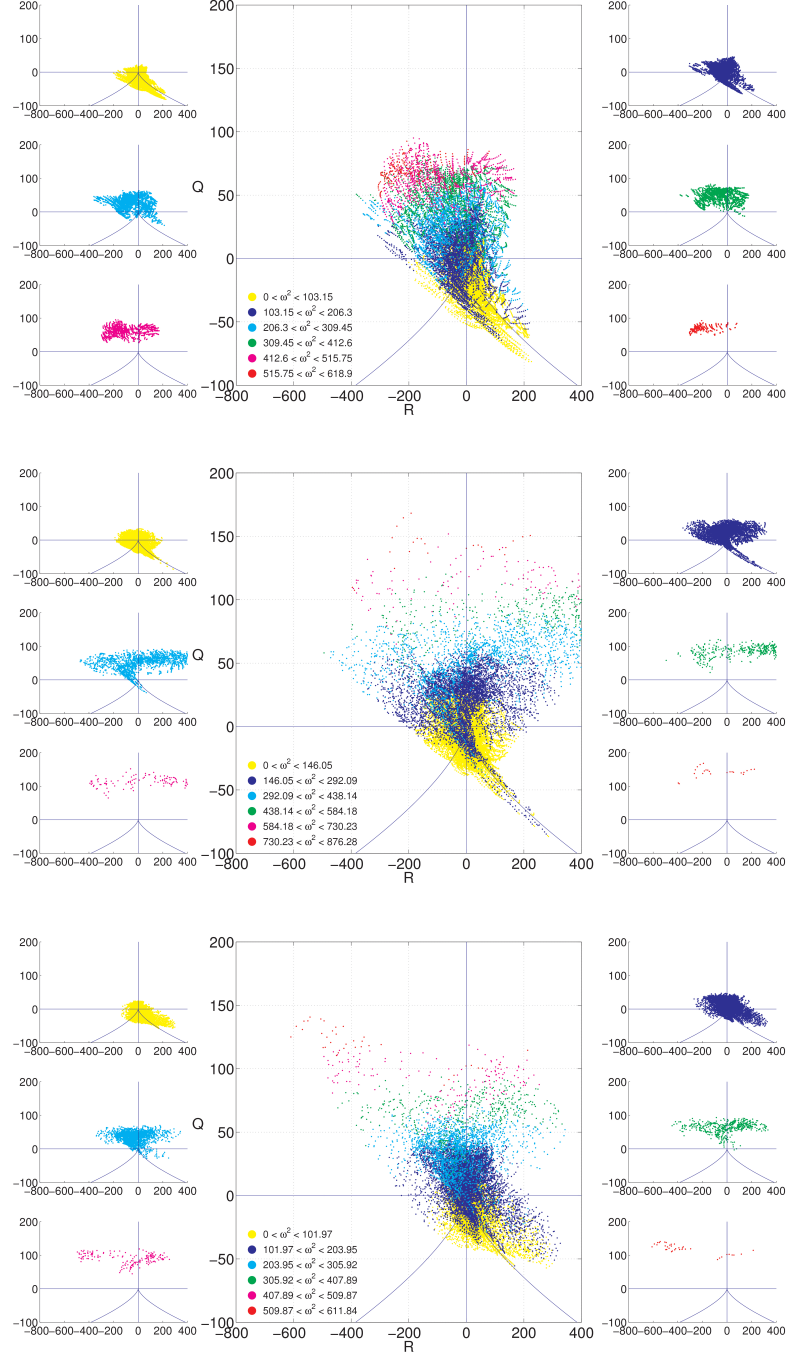


Figure 5.7: RQ sampled by ω^2 in the intervals; $[0.4, 0.425]$ (top), $[0.5, 0.525]$ (middle), $[0.6, 0.625]$ (bottom).

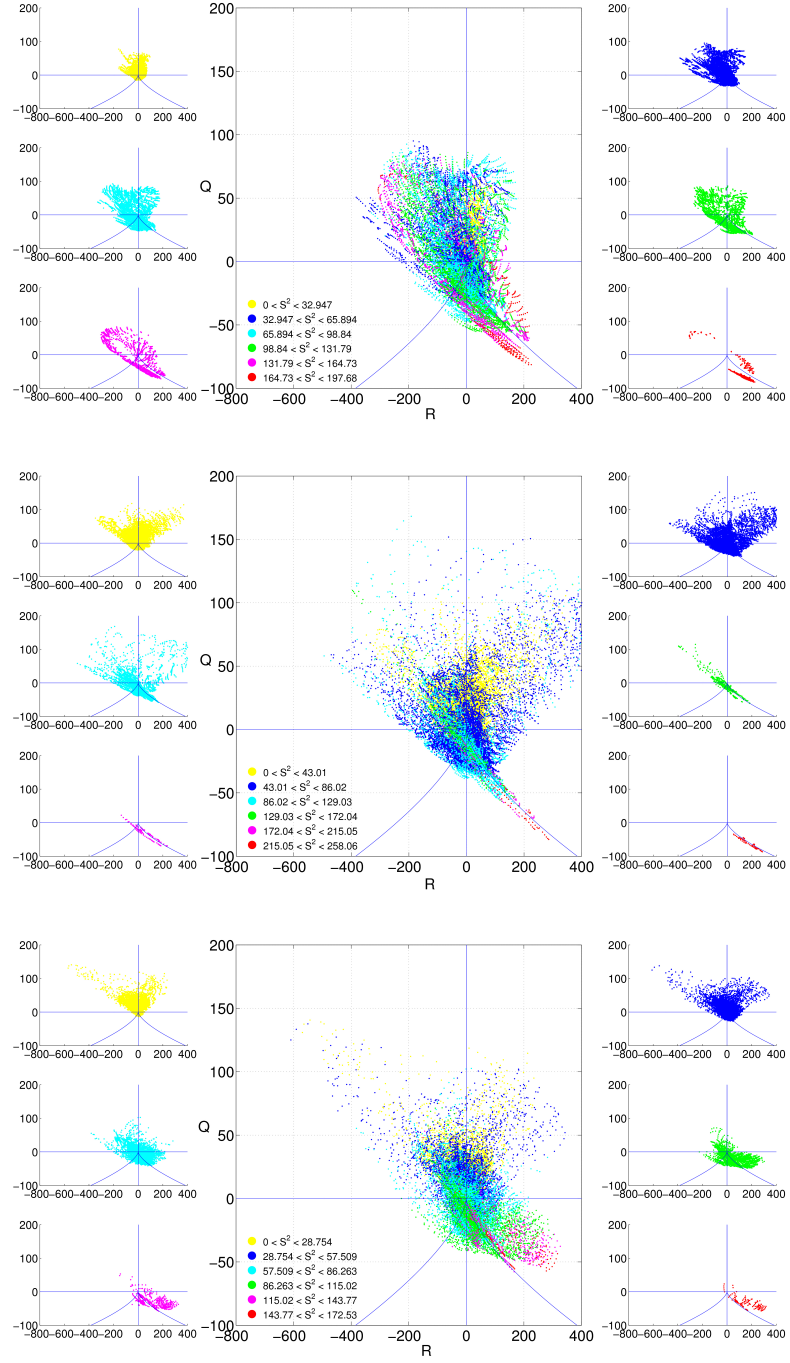


Figure 5.8: RQ sampled by S^2 in the intervals; $[0.4, 0.425]$ (top), $[0.5, 0.525]$ (middle), $[0.6, 0.625]$ (bottom).

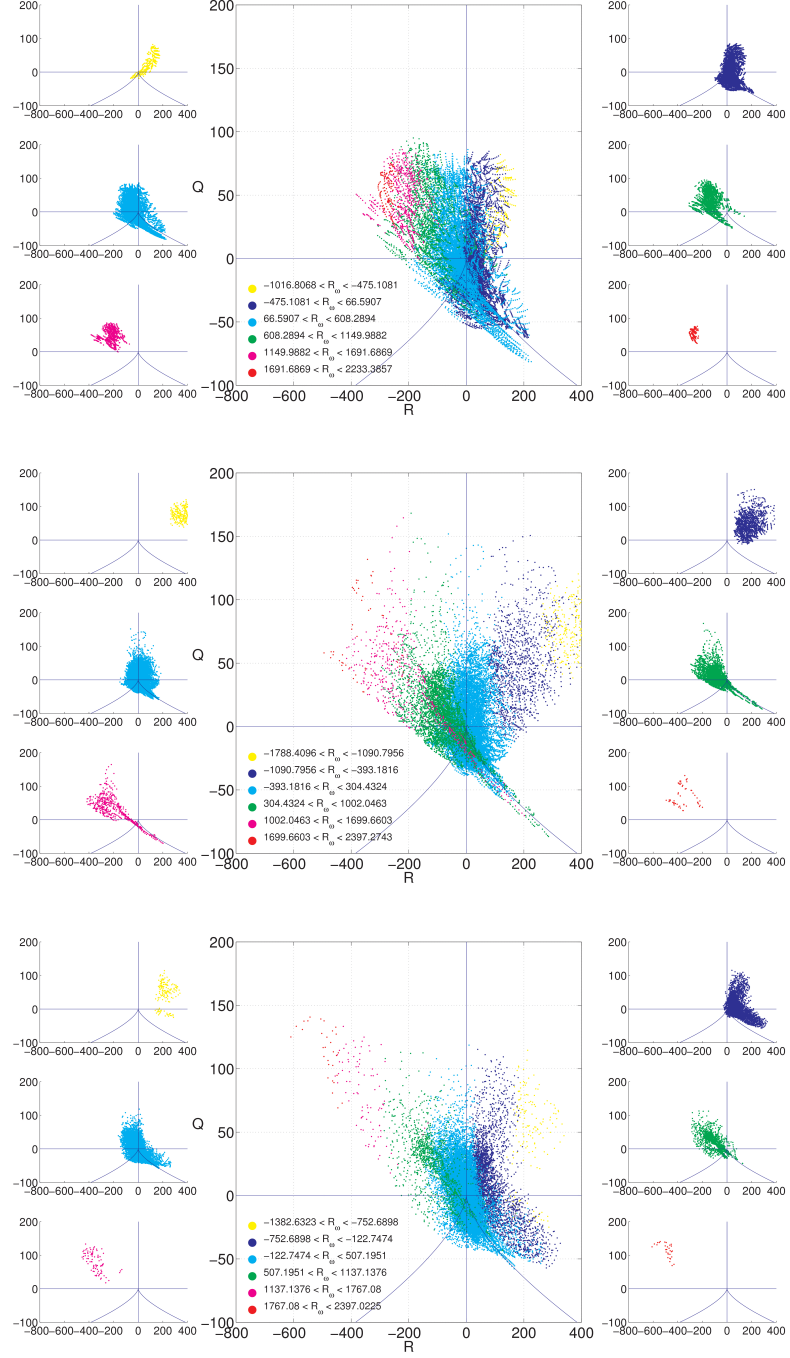


Figure 5.9: RQ sampled by R_w in the intervals; $[0.4, 0.425]$ (top), $[0.5, 0.525]$ (middle), $[0.6, 0.625]$ (bottom).

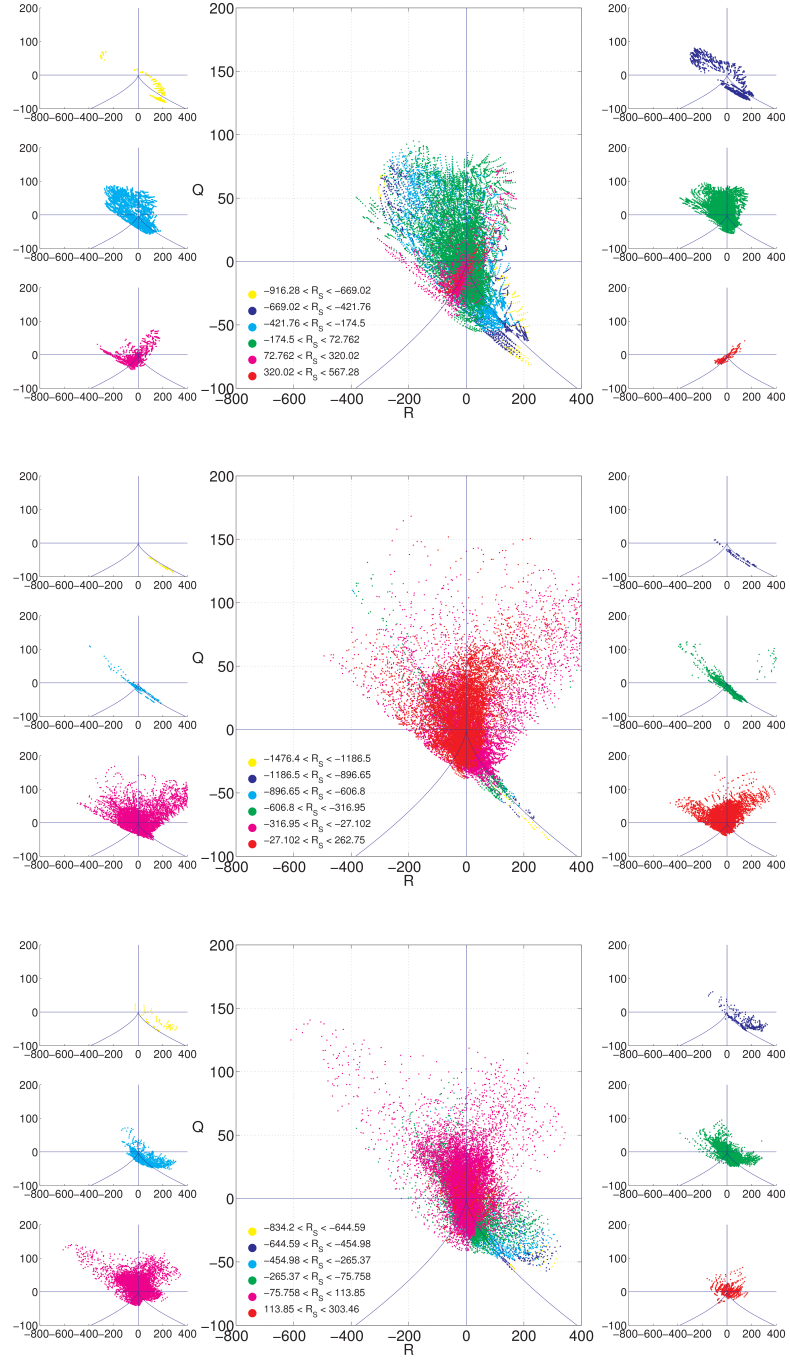


Figure 5.10: RQ sampled by R_S in the intervals; $[0.4, 0.425]$ (top), $[0.5, 0.525]$ (middle), $[0.6, 0.625]$ (bottom).

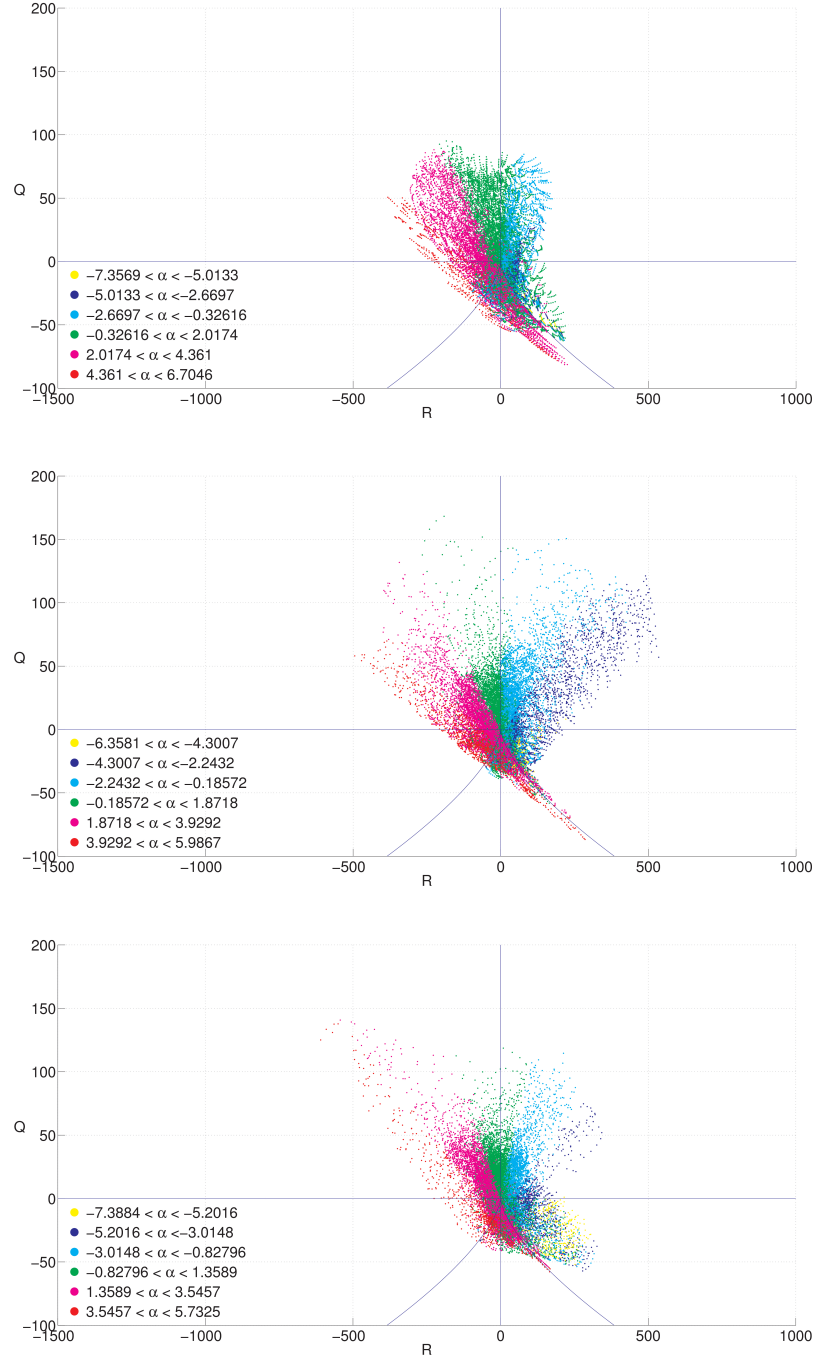


Figure 5.11: RQ sampled by α in the intervals; $[0.4, 0.425]$ (top), $[0.5, 0.525]$ (middle), $[0.6, 0.625]$ (bottom).

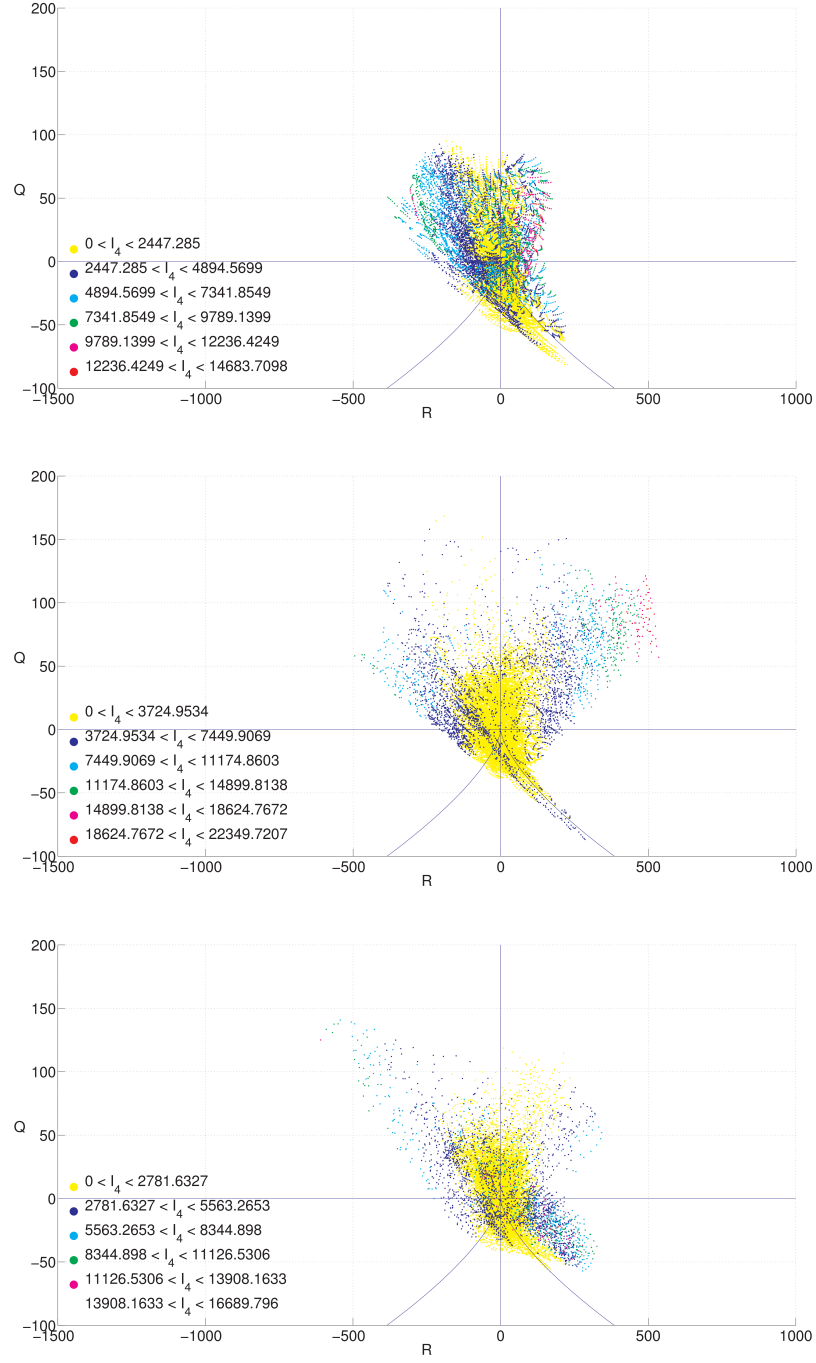


Figure 5.12: RQ sampled by I_4 in the intervals; $[0.4, 0.425]$ (top), $[0.5, 0.525]$ (middle), $[0.6, 0.625]$ (bottom).

Chapter 6

Pressure Hessian

This chapter will focus on separating the local and non-local components of the pressure Hessian and their effects upon the surrounding fluid. The pressure Hessian is the set of second order partial derivatives of the pressure field denoted as:

$$[\mathbf{P}]_{ij} = \frac{\partial^2 p}{\partial x_i \partial x_j}. \quad (6.1)$$

The local terms of \mathbf{P} are defined by the Restricted Euler terms (6.14), which are dependent solely upon local properties such as the vorticity, strain and other quantities formed from the velocity derivatives. The full pressure field, and its derivatives, are a non-local solution of a Poisson type equation with a quadratic source term formed from velocity derivatives.

$$\Delta \mathbf{p} = -\nabla \cdot (\mathbf{u} \cdot \nabla \mathbf{u}). \quad (6.2)$$

For our purposes, the non-local terms will be the differences between the full Poisson solution and the RE solution.

The RE model has been studied in part because it might form the basis of finding a suitable closure for the pressure and viscous terms in the Navier-Stokes equations, as discussed in Chapter 2. Most of these studies have looked at modifying the isotropic assumption with extra terms, both deterministic and stochastic, while neglecting to discuss the valid-

ity of the isotropic assumption for the pressure Hessian in general.

Equation (6.2) is solved through the application of the Biot Savart Law. Ohkitani [40] shows that if the velocity \mathbf{u} is written as the curl of a vector potential B , $\mathbf{u} = \nabla \times B$. Then the solution to an equation of the form $\nabla^2 B = \boldsymbol{\omega}$ is given by:

$$B(x) = \frac{1}{4\pi} \int G(\mathbf{y}) \omega(\mathbf{y}) d^3 \mathbf{y}. \quad (6.3)$$

Here $G(\mathbf{y})$ is a smooth function. In order to solve equation (6.2) the Laplacian operator needs to be applied to the pressure Hessian.

$$[\mathbf{P}]_{ij} = -\frac{\partial^2}{\partial y_i \partial y_j} \Delta^{-1} \text{tr}(\mathbf{A}^2) = -\nabla \nabla \Delta^{-1} \text{tr}(\mathbf{A}^2) \quad (6.4)$$

Where, \mathbf{A} is the velocity gradient tensor. Application of the Biot Savart law leads us to a solution for the pressure Hessian:

$$\mathbf{P} = -\frac{1}{4\pi} \int \mathbf{G}(\mathbf{y}) \text{tr}(\mathbf{A}^2) d^3 \mathbf{y}. \quad (6.5)$$

Where:

$$\mathbf{y} = \mathbf{x} - \mathbf{x}', \quad \text{and} \quad \mathbf{G}(\mathbf{y}) = \frac{\partial^2}{\partial y_i \partial y_j} \frac{1}{|\mathbf{y}|}. \quad (6.6)$$

Without solving the integral it is obvious that when $x \rightarrow x'$ the integral is undefined, as the denominator will be zero. However when $i = j$ we have the isotropic pressure Hessian and using the method of Cauchy principal value integrals ($PV \int = \lim_{R \rightarrow 0} \int_{B(x) \geq R}$) an equation for the pressure Hessian is derived that considers the local and non local effects.

$$\mathbf{P} = -\text{tr}(\mathbf{A}^2) \frac{\delta_{ij}}{3} + PV \int \mathbf{K}(\mathbf{y}) \text{tr}(\mathbf{A}^2) d^3 \mathbf{y}. \quad (6.7)$$

where:

$$\mathbf{K}(\mathbf{y}) = \frac{|\mathbf{y}|^2 \delta_{ij} - 3y_i y_j}{4\pi |\mathbf{y}|^5}. \quad (6.8)$$

The first term on the RHS is the isotropic part of the pressure Hessian and is a local effect of the flow. The second term considers the action

over the entire flow field and such is a non local effect.

6.1 Calculating p and P

The current pseudo-spectral code solves the velocity-vorticity form of the Navier Stokes equation as discussed in Chapter 3. In this formulation the pressure head π is used, not the pressure p , which are related by $\pi(\mathbf{x}, t) = \mathbf{p}(\mathbf{x}, t) + \frac{1}{2}\mathbf{u}^2(\mathbf{x}, t)$. To obtain the pressure field and its first and second order derivatives we must calculate $\frac{1}{2}\mathbf{u}^2$, and then subtract it from π , we then find the pressure derivatives which are stored in the following order: $p_{,z}; p_{,zz}; p_{,zy}; p_{,y}; p_{,yy}; p_{,yz}; p_{,x}; p_{,xx}; p_{,xz}$ and $p_{,xy}$.

6.2 Discussion

A major consideration in large-eddy simulations is deciding upon a pressure closure. The Restricted Euler equations offer an alternative approach to existing methods. In a pseudo-spectral code you can roll the pressure into the non linear term in Fourier space fairly neatly, however it is not quite this straightforward when considering alternative models. Chevillard and Meneveau [3] introduce the concept of an inverse Cauchy Green tensor as a method of closing the pressure Hessian which is analogous to work of Chertkov et al [19]. Furthermore Gotoh et al [41] show that the pressure term is key to understanding the scaling of the velocity structure functions and Ohkitani [42] explains that if we have a finite-time blow up of the vorticity; then equation (6.9) and the theorem of Beale Kato Majda [43] can be applied to show that there will be a blow up of the pressure field also.

$$\frac{D^2\boldsymbol{\omega}}{Dt^2} = -\mathbf{P}\boldsymbol{\omega}. \quad (6.9)$$

The aim is to understand the role and action of the pressure Hessian. We have discussed how the pressure can be calculated through the strain and vorticity and whilst we are primarily interested in the behaviour of

these quantities; the development and effect of the pressure Hessian is of great interest. Taking the trace of the pressure Hessian equation (6.1), we obtain a Poisson equation in terms of the velocity gradient tensor.

$$\nabla^2 \mathbf{p} = -A_{ij}A_{ji}. \quad (6.10)$$

6.2.1 Isotropy and Pressure Decomposition

Reviewing equation (6.7), the first term is the Vieillefosse term representing the isotropic component of the pressure Hessian which works to preserve the volume of the fluid element against the deformation gradient. The second term is the non local component, frequently referred to as the deviatoric component of the pressure Hessian. Chevillard [3] suggested that equation (6.10) is all that is required to show non locality of the pressure field. He states that it is the unrestricted growth of the self stretching term $-A^2$; due to the absence of the pressure and viscous terms that leads to the finite time singularity as discussed in Chapter 5.

However in order to fully understand non local effects, and in particular how they relate to regions of development and destruction within the flow field more work must be undertaken. Nomura and Post [44] propose that previously we have looked at the pressure Hessian in the wrong way. They suggest we think of the pressure Hessian as the quantity that describes the non local interaction of the vorticity and strain. The pressure Hessian is composed of an isotropic and deviatoric term. The isotropic term of the pressure Hessian $[\mathbf{P}]_{ii}$ is simply the trace of the pressure Hessian so as to satisfy the incompressibility condition. The anisotropic part is what is left; that is the set of mixed partial derivatives of the pressure Hessian minus the isotropic part. The pressure Hessian is then the sum of these two quantities:

$$P_{ij} = P_{kk} \frac{\delta_{ij}}{3} - H_{ij}. \quad (6.11)$$

It then follows that the anisotropic or deviatoric pressure Hessian is defined as:

$$H_{ij} = -P_{ij} + P_{kk} \frac{\delta_{ij}}{3}. \quad (6.12)$$

6.2.2 Evolution Equation Derivation

The vorticity evolution equation is given as:

$$\frac{D\boldsymbol{\omega}}{Dt} = \mathbf{S}\boldsymbol{\omega}. \quad (6.13)$$

As equation (6.13) contains no component of the pressure Hessian, we cannot directly consider the effect the pressure Hessian has on vortex stretching, however the evolution of strain introduces the pressure Hessian into Q (2.30):

$$\frac{d\mathbf{S}}{dt} = -\mathbf{S}\mathbf{S} - \frac{1}{4}\boldsymbol{\omega} \otimes \boldsymbol{\omega} + \frac{1}{4}\mathbf{I}|\boldsymbol{\omega}|^2 - \mathbf{P}. \quad (6.14)$$

and finally the dissipation can be easily found from above:

$$\frac{1}{2} \frac{d\mathbf{S}^2}{dt} = -\mathbf{S}\mathbf{S}\mathbf{S} - \frac{1}{4}\boldsymbol{\omega}\mathbf{S}\boldsymbol{\omega} - \mathbf{S}\mathbf{P}. \quad (6.15)$$

Now if consider the strain dissipation $\mathbf{R}_\mathbf{S}$, noting that $\mathbf{S}^4 = \frac{1}{2}(\mathbf{S}^2)^2$:

$$\frac{d\mathbf{S}^3}{dt} = \frac{d\mathbf{S}}{dt}\mathbf{S}^2 + \mathbf{S}\frac{d\mathbf{S}}{dt}\mathbf{S} + \mathbf{S}^2\frac{d\mathbf{S}}{dt}, \quad (6.16)$$

$$= 3\mathbf{S}^2\frac{d\mathbf{S}}{dt}, \quad (6.17)$$

$$= -3\mathbf{S}^4 - \frac{3}{4}\mathbf{I}_4 + \frac{3}{4}\mathbf{S}^2\boldsymbol{\omega}^2 - 3\mathbf{S}\mathbf{P}\mathbf{S}, \quad (6.18)$$

$$= -\frac{3}{4}\mathbf{I}_4 + 3\mathbf{S}^2 \underbrace{\left(-\frac{1}{2}\mathbf{S}^2 + \frac{1}{4}\boldsymbol{\omega}^2\right)}_{=Q} - 3\mathbf{S}\mathbf{P}\mathbf{S}. \quad (6.19)$$

We arrive at the following

$$\frac{d\mathbf{R}_\mathbf{S}}{dt} = -\frac{3}{4}\mathbf{I}_4 + 3\mathbf{S}^2Q - 3\mathbf{S}\mathbf{P}\mathbf{S}. \quad (6.20)$$

Moving on to the enstrophy production term, using equations (6.13) and (6.14)

$$\frac{d\mathbf{R}_\omega}{dt} = \boldsymbol{\omega} \frac{d\mathbf{S}}{dt} \boldsymbol{\omega} + 2\boldsymbol{\omega} \mathbf{S} \frac{d\boldsymbol{\omega}}{dt}, \quad (6.21)$$

$$= -I_4 - \boldsymbol{\omega} \mathbf{P} \boldsymbol{\omega} + 2I_4, \quad (6.22)$$

$$= I_4 - \boldsymbol{\omega} \mathbf{P} \boldsymbol{\omega}. \quad (6.23)$$

Finally, by using equations (6.13) and (6.14) again, and the equation for the second invariant Q :

$$Q = -\frac{1}{2}\mathbf{S}^2 + \frac{1}{4}\boldsymbol{\omega}^2. \quad (6.24)$$

$$\begin{aligned} \frac{dQ}{dt} &= -\frac{1}{2} \frac{d\mathbf{S}^2}{dt} + \frac{1}{4} \frac{d\boldsymbol{\omega}^2}{dt}, \\ &= \mathbf{R} \mathbf{S} + \frac{3}{4} \mathbf{R} \boldsymbol{\omega} + \mathbf{S} \mathbf{P}, \\ &= -3R + \mathbf{S} \mathbf{P}. \end{aligned} \quad (6.25)$$

It is noteworthy to mention that $\delta_{ij} S_{ij} = 0$ is analogous to the incompressibility equation. So by using equation (6.12) we arrive at the following equations for the velocity gradient invariants, the enstrophy has not been forgotten it simply does not have a component of the pressure:

$$\frac{d\mathbf{R} \mathbf{S}}{dt} = -\frac{3}{4} I_4 + \mathbf{S}^2 Q + 3\mathbf{S} \mathbf{H} \mathbf{S}, \quad (6.26)$$

$$\frac{d\mathbf{R}_\omega}{dt} = I_4 - \frac{2}{3} \boldsymbol{\omega}^2 Q + \boldsymbol{\omega} \mathbf{H} \boldsymbol{\omega}, \quad (6.27)$$

$$\frac{dQ}{dt} = -3R - \mathbf{S} \mathbf{H}. \quad (6.28)$$

6.3 Conditional Mean Trajectories

The analysis of the R-Q joint distribution functions so far has been kinematic and has established the consistency between this data set and earlier work relating the invariants to the geometry of the small scales. We

now want to introduce similar dynamical R-Q analysis similar to Ooi et al [45] who examined the Lagrangian dynamics of the invariants of the velocity gradient tensor using conditional mean trajectories or CMTs. To generate CMTs one collects the statistics of the Lagrangian motion on a refined mesh in the R-Q space. As we are interested in the second Q and third R invariant of the velocity gradient tensor, their CMT's can be defined as follows:

$$\begin{aligned}\dot{\mathbf{Q}}(\mathbf{Q}, \mathbf{R}) &= \left\langle \frac{d\mathbf{Q}}{dt} \middle| Q = Q_0, R = R_0 \right\rangle, \\ &= \frac{1}{N_{RQ}} \sum_{\bar{Q} - \frac{\Delta Q}{2}}^{\bar{Q} + \frac{\Delta Q}{2}} \sum_{\bar{R} - \frac{\Delta R}{2}}^{\bar{R} + \frac{\Delta R}{2}} \frac{d\mathbf{Q}}{dt}(\mathbf{Q}, \mathbf{R}).\end{aligned}\quad (6.29)$$

$$\begin{aligned}\dot{\mathbf{R}}(\mathbf{Q}, \mathbf{R}) &= \left\langle \frac{d\mathbf{R}}{dt} \middle| Q = Q_0, R = R_0 \right\rangle, \\ &= \frac{1}{N_{RQ}} \sum_{\bar{Q} - \frac{\Delta Q}{2}}^{\bar{Q} + \frac{\Delta Q}{2}} \sum_{\bar{R} - \frac{\Delta R}{2}}^{\bar{R} + \frac{\Delta R}{2}} \frac{d\mathbf{R}}{dt}(\mathbf{Q}, \mathbf{R}).\end{aligned}\quad (6.30)$$

where $(Q_0, R_0) = (0, 0)$ is the central mesh point, N_{RQ} is the number of points, is a small deviation from Q . The refined mesh is centred around this point $\pm \frac{\Delta Q}{2}$ and the mean values of the two evolution equations are determined. In Chapter 7 this approach is extended to three variables. Two methods have been used before to graphically represent these results, streamlines in R-Q space and vectors on the grid points in the R-Q space. In this work only the vectors will be shown. The direction and magnitude of the vectors represents the velocity and Lagrangian path.

Figure 6.1 considers the R-Q space RE trajectories of Lagrangian points for Run A at $t = 0.5$, with flow converging along both sides of the Vieille-fosse asymptote as observed in [46]. The family of curves for $\frac{dQ}{dt}$ and $\frac{dR}{dt}$ here are in the left images of figures 6.2 through to 6.5 are consistent

with the results of [45]. How do these model curves compare with the effects of the full pressure Hessian? This has previously been considered twice [47] and [48], but only for forced flows. The right images of Figures 6.2 through to 6.5 show that this well-defined phase space flow breaks down with a distinct change in the central flow field, before relaxing to the restricted Euler prediction.

To understand the R-Q trajectories for all times, it is best to start with the final times shown for all the datasets, $t = 0.6$. For the full pressure Hessians these are the last row in figure 6.6 for B and C and figure 6.5 for A. What should be observed is that all of them are similar. That is, all the full pressure Hessian trajectories look like the RE trajectory in 6.5, with trajectories eventually pointing along the Vieillefosse discriminant (6.31) in the lower right.

$$R = \left(\frac{-4}{27} Q^3 \right)^{1/2} \quad (6.31)$$

This shows that for all the datasets, the trajectories have similar final states, even if they did not get there at the same rate. This could be called the fully developed vortex tube regime because in all cases, the spectra form a $k^{-5/3}$ at least briefly and the vorticity field is becoming dominated by vortex tubes.

Now, let us start at the early time of $t = 0.3$, which is representative of everything before then for all the cases. Trajectories using the full pressure Hessian are in the first row in figure 6.6 for datasets B and C and figure 6.2 for dataset A. There is some tendency for the trajectories to flow clockwise in the upper half $Q > 0$ plane as in all of the RE trajectories for all times in figures 6.2 to 6.5, and the last times for the full Hessian. However, along the Vieillefosse discriminant (6.31), the full Hessian trajectories cross it directly and for $0 > Q > -100$ tend to flow back around the point $R = Q = 0$.

One could call the evolution up to $t = 0.3$ the sheet-like region, suggesting that the strong deviation from the RE prediction is because the structures are as far as possible from the vortex tube configurations that are associated with RE type statistics.

For the next time shown, $t = 0.4$ figures 6.3 and 6.6 (row 2, right) for datasets A and C respectively, an ill-defined line forms that approximately follows the Vieillefosse discriminant. At the higher Reynolds number, dataset B; figure 6.6 (row 2 left), two features should be noted. First, something closer to the RE trajectories are forming along the discriminant in the lower right quadrant. Second, nearer $R = Q = 0$ the trajectories are clearly circulating about $R = Q = 0$ over a larger regime.

The tendency towards the RE trajectories continues at $t = 0.5$, again more strongly for the higher Reynolds number in dataset B where the full Hessian trajectories nearly match the RE trajectory for dataset B in figure 6.6 (row 3, left). While datasets A and C figures 6.4 and 6.6 (row 3, right) at lower Reynolds number, have caught up to the situation that existed at $t = 0.4$ for dataset B. That is, in the lower right quadrant trajectories tend to follow the Vieillefosse discriminant while circulating around $R = Q = 0$ for $0 < Q < -100$.

Finally, at $t = 0.6$ for all cases, the trajectories in figures 6.5 and 6.6 (row 4) are similar those in the RE figure 2.1 provided in Chapter 2.

6.4 Underlying Physics

Lagrangian paths are an example of a topological feature in turbulent flow. The Vieillefosse model's assumption is that the evolution of the second and third invariants along these paths is consistent with the assumption that the pressure Hessian is isotropic, these trajectories are

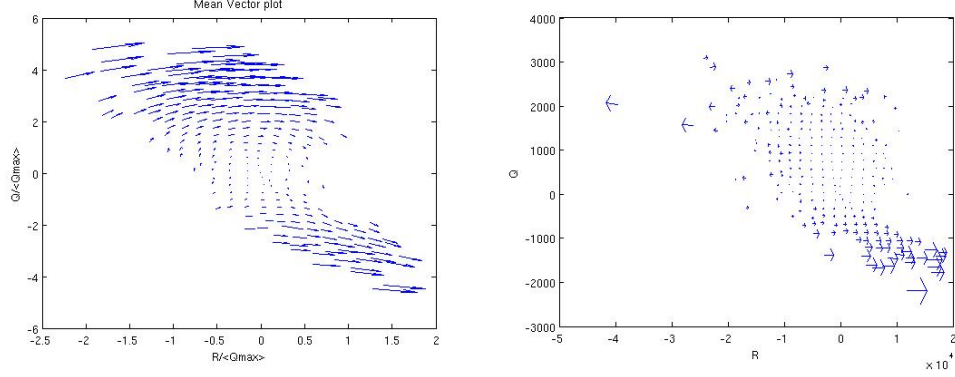


Figure 6.1: A typical restricted Euler (RE) trajectory for reference for all the following figures showing trajectories of points in the R-Q phase space. In this figure the vectors show the strength and direction of the Lagrangian RE time derivatives (6.14) of Lagrangian points in physical space for dataset A at time $t = 0.5$, essentially the same data as used for scatter plots in figures 5.7b, 5.8b, 5.9b, 5.10b, and 5.12b and is included in Figure 6.2. In RE, the dominant path of trajectories is clock-wise about $(R, Q) = (0, 0)$ for $Q > 0$, converging on the Vieillefosse discriminant (6.31) in the lower right quadrant.

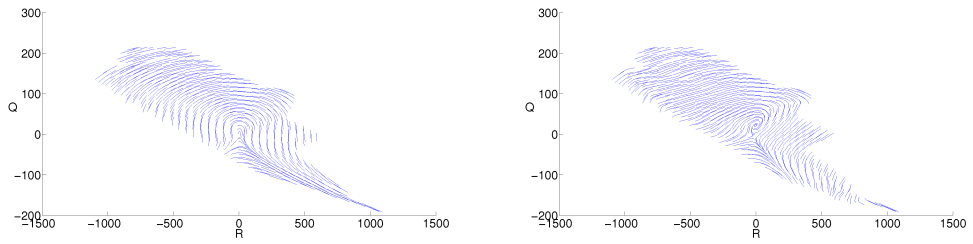


Figure 6.2: R-Q trajectories of Lagrangian points of the second and third invariants of the velocity gradient tensor within the interval $t = [0.0, 0.3]$, from dataset A a) left image is where we have neglected the effects of the deviatoric pressure Hessian, and b) the right image is the full flow.

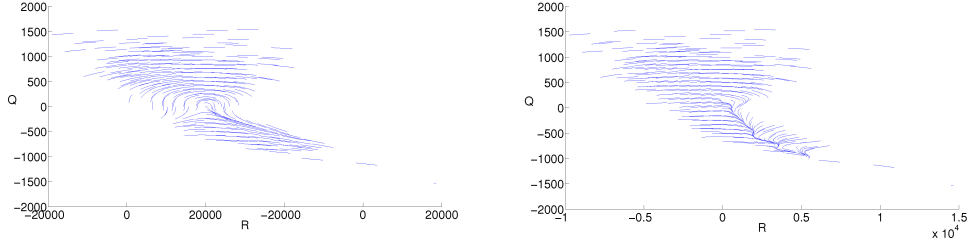


Figure 6.3: R-Q trajectories of Lagrangian points of the second and third invariants of the velocity gradient tensor within the interval $t = [0.3, 0.4]$, from dataset A a) left image is where we have neglected the effects of the deviatoric pressure Hessian, and b) the right image is the full flow.

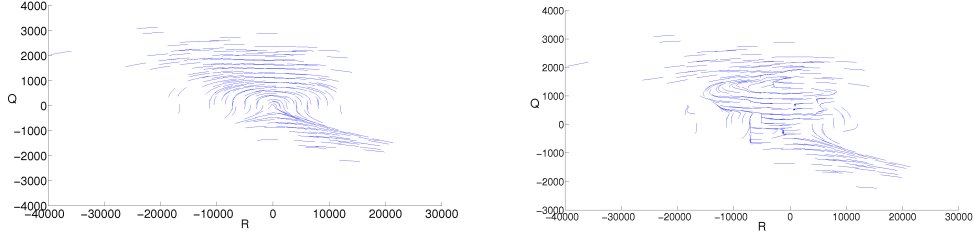


Figure 6.4: R-Q trajectories of Lagrangian points of the second and third invariants of the velocity gradient tensor within the interval $t = [0.4, 0.5]$, from dataset A a) left image is where we have neglected the effects of the deviatoric pressure Hessian, and b) the right image is the full flow..

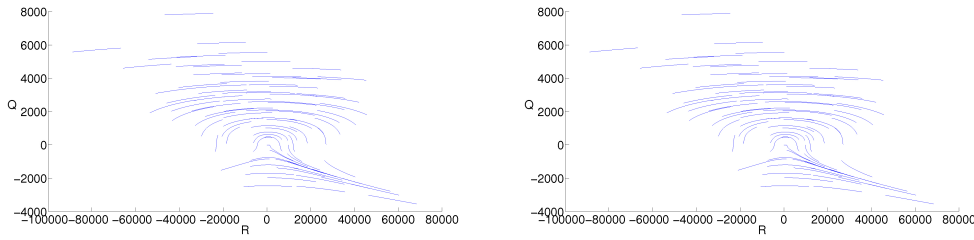


Figure 6.5: R-Q trajectories of Lagrangian points of the second and third invariants of the velocity gradient tensor within the interval $t = [0.5, 0.7]$, from dataset A a) left image is where we have neglected the effects of the deviatoric pressure Hessian, and b) the right image is the full flow.

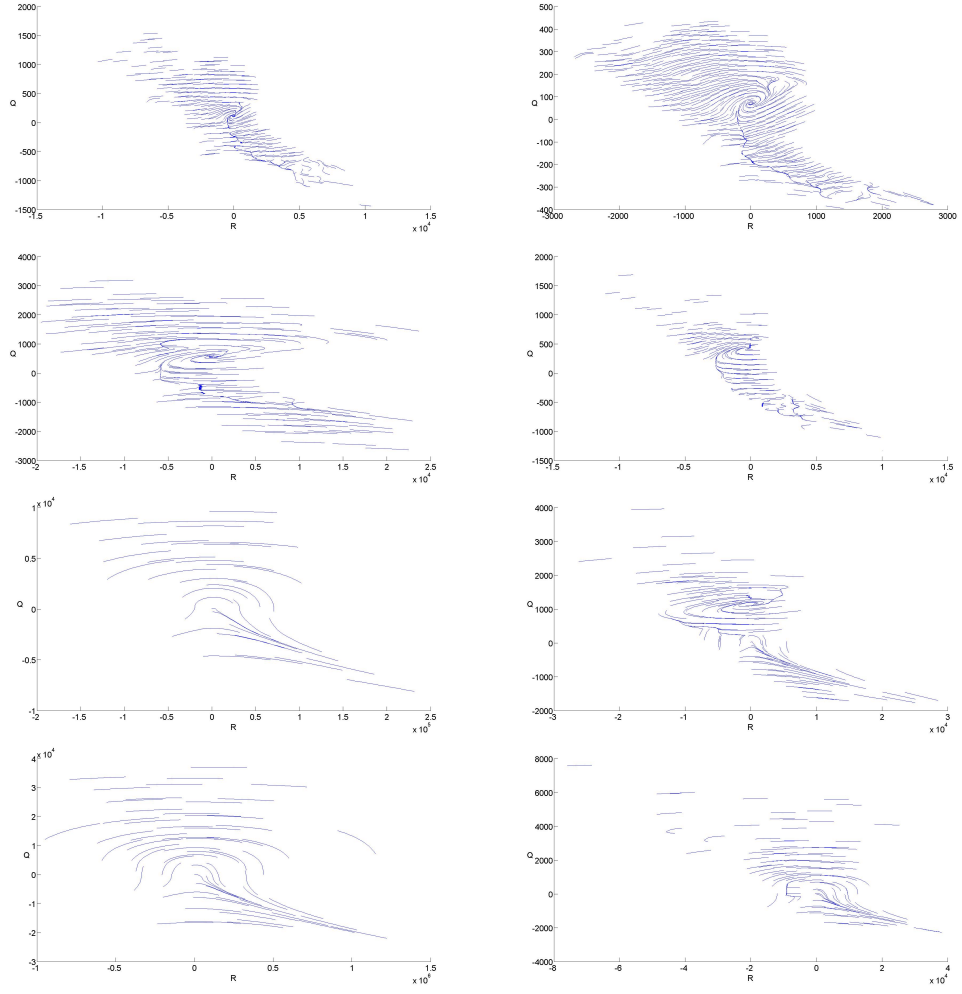


Figure 6.6: The left images are taken from dataset B and the right images are taken from dataset C. (Top) $t=0.3$, (Second) $t=0.4$, (third) $t=0.5$ and (last) $t=0.6$.

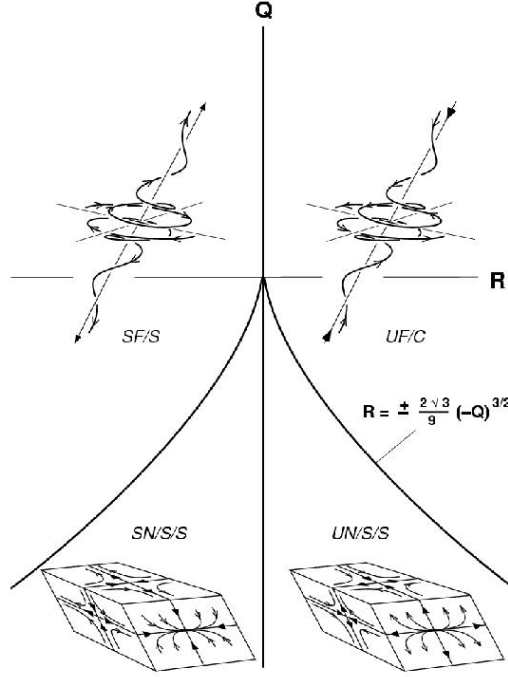


Figure 6.7: Three-dimensional topologies in the R-Q plane, taken from [47]

illustrated by the left image of figures 6.2 to 6.5. The topologies in the R-Q plane are illustrated in figure 6.4. This evolution moves between quadrants in the R-Q diagram in a manner that would be consistent with how vortex sheets could be transformed into vortex tubes by slowly rolling up. This has been observed in many turbulent calculations with initial conditions similar to those used here going as far back as [49], even if the details of any such transition were not fully understood until [30].

In the viscous Navier-Stokes equations fluid parcels do not necessarily follow Lagrangian paths, this is a phenomena of the inviscid Euler equations. In the Navier-Stokes equations, fluid parcels diverge from Lagrangian paths, which has been demonstrated numerically using the potential vorticity of a passive scalar [50] and through Weber-Clebsch variables where the Lagrangian map is shown to be non-invertible [51].

Numerical simulations show fluid parcels diverging from Lagrangian paths

when there is a vortex reconnection. Vortex reconnection is another example of breaking a topological invariant besides the divergence of fluid parcel motion from the Lagrangian paths. Several properties are well known a) The reconnection of coherent structures is a by product of the viscosity and b) Topological changes occur when the dissipation dominates the coherent structures. Recent numerical work [52] and [30] gave an example of how reconnection events can induce a rapid change in topology that creates vortex tubes from vortex sheets, a change that is faster than the traditional view that vortex tubes are formed from vortex sheets rolling up. Following Holm and Kerr [30] the general development of structures obeys the following sequence:

- Collision of blobs of vorticity,
- Around $t = 0.3$ vortex sheets dominate the flow, with the intensity of their growth determined by the Reynolds number.
- Between $t = 0.3 - 0.5$, is a transitional period, between sheets and tubes.
 - * Somewhere during this span there is vortex reconnection, which might be related to the L-infinity norm of vorticity ($\|\omega\|_\infty$) forming a singularity in the inviscid limit.
- Between $t = 0.4 - 0.7$. Formation of vortex tubes and strong dissipation.
- Finally for $t > 0.9$ after about one eddy turnover time, a $k^{-5/3}$ spectral regime forms and small-scale vortex tubes dominate.

This process is consistent with the observation here, the most rapid changes in the R-Q statistics are up to $t = 0.5$ and could be because the R-Q have evolved from their original state due to a global change in the topology of the fluid flow.

The helicity and the kinetic energy are quadratic invariants conserved

by the Euler equation, The helicity is defined as:

$$H = \int h(x)dV = \int \mathbf{u} \cdot \boldsymbol{\omega} dV. \quad (6.32)$$

Here V represents the fluid volume and $h(x)$ is the local helicity density. The helicity density is measure of the vortical topology, how vortices are linked in a turbulent flow [53]. One would expect to see changes in the helicity if these links are broken.

Transitional growth events exhibited in a developing turbulent flow, generated from a smooth initial condition are discussed in Holm and Kerr [52] where particular emphasis is given to the helicity and the role it has in establishing the energy cascade. Further analysis [30] concluded that the critical changes in the helicity were during the phase $0.4 < t < 0.5$ when vortex reconnection is dominant.

This period $0.4 < t < 0.5$ corresponds to where we have no observed strong changes in the trajectories in the R-Q plane, suggesting that reconnection is recycling trajectories. That is, rather than asymptotically approaching the Vieillefosse discriminant, under the action of the full pressure Hessian, during reconnection many of the trajectories return to the source quadrant.

One conclusion then could be that it is the RE model, representing the effects of stretched vortex tubes, that dominate the subgrid pressure dynamics and models based upon this model could be appropriate. However, the RE dynamical behaviour is not consistent with the events during reconnection periods, which should be modelled differently. Now that a reconnection period has been identified, how should the flow be modelled during these periods? In Chapter 7 we find changes in the distribution of higher-order Vieillefosse moments that could potentially be used to quantify these effects.

In figure 6.8 an interaction region between the strain and vorticity is

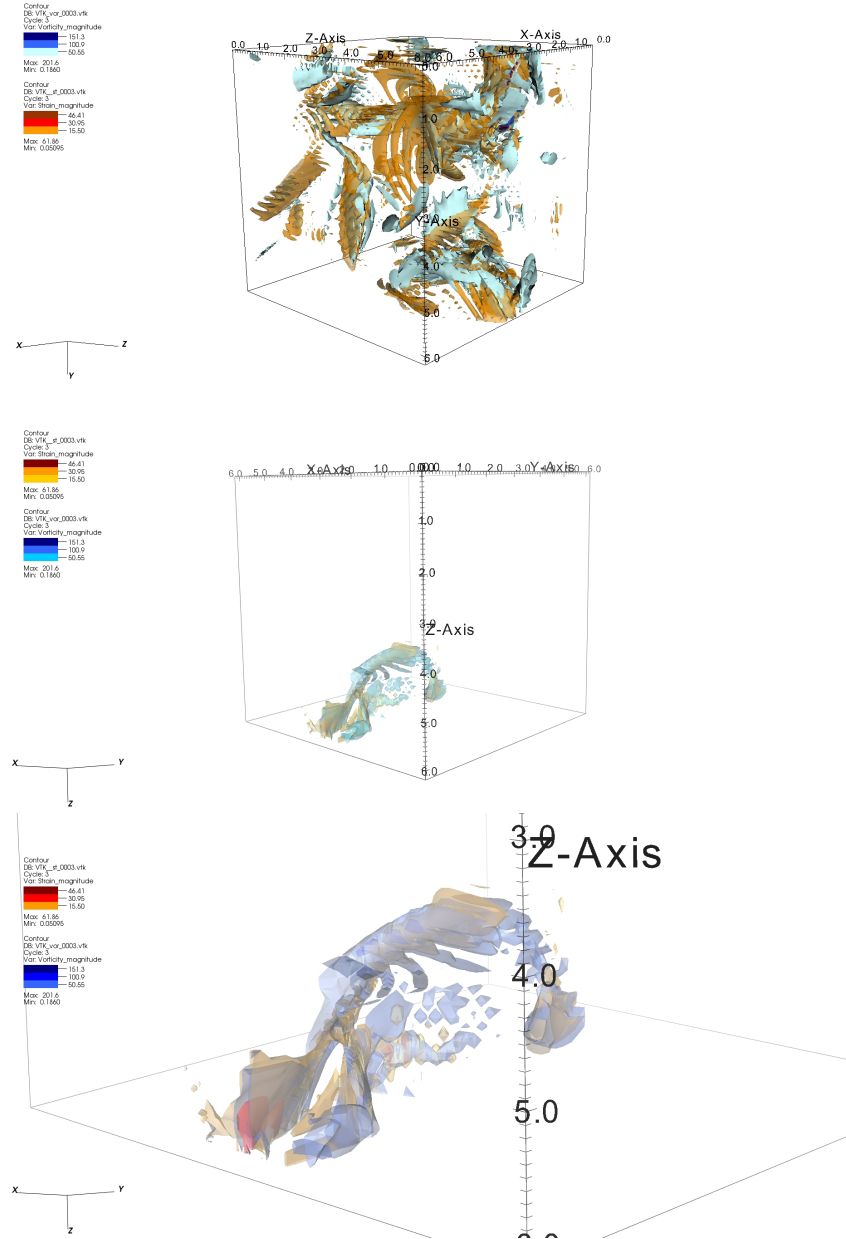


Figure 6.8: Here the interaction region between the strain and vorticity is realised from simulation A at time $t = 0.5$. Here The top image is a visualisation of the total vorticity and strain interaction within the periodic domain, the middle image is the subset of the same domain containing the interaction region. The final image is a refined view with varying levels of opacity for both the strain and vorticity. The vorticity magnitude is divided into three regions; blue $|\omega| \approx 152$, light blue $|\omega| \approx 102$, pale blue $|\omega| \approx 152$. Similarly the strain magnitude is divided into three coloured sections, brown $|\mathbf{S}| \approx 47$, red $|\mathbf{S}| \approx 31$, orange $|\mathbf{S}| \approx 16$. Please note that the ribs are a resolution effect in the graphic caused by only sampling every other point.

found from simulation A at time $t = 0.5$. The top image looks at the entire flow field conditioned on the magnitude of strain and vorticity within a periodic domain. The central image is a close up of one of the regions of greatest interaction between the strain and vorticity at this time, with the last image a zoomed in view.

6.5 Summary

The significance of the pressure Hessian's role within the NSE has been explained, with particular emphasis on the isotropic, or Vieillefosse, assumption. The effect of the pressure can be felt both locally through the square of the velocity stress tensor A^2 and through the Poisson equation. The anisotropic component is due to the solution of the Cauchy principal value integral over the entire flow field.

The focus on the isotropic assumption and its comparison to the full equations has shown that while the RE equations are a good starting point for allowing numerical and analytical investigations of the flow field, they do not capture all features of the flow. When considering the trajectories of R and Q , it is noted that for $Q < 0$ there is a marked difference in the flow trajectories before and during a reconnection event. Evidence is presented that this is related to the change in the global topology of the flow due to a reconnection. Recently, Lüthi [6] has extended the R-Q phase space into three dimensions, with what we have just seen can we gain anything by considering the evolution of these quantities in three-dimensional space? This leads us to Chapter 7.

Chapter 7

3D Phase Space

Up to now we have been almost exclusively concerned with the events in 2D Phase space, now whilst this has allowed us to gain further insight in to the formation and reconnection of structures in 3D turbulence it only provides a snap shot of the underlying events and the processes leading to their generation and dissipation within the flow field. Ideally, we would see a model of turbulence that contains the four key turbulence invariants, and possibly Siggia's I_4 . A 5D model should have the necessary sophistication to predict the flow characteristics, however we are looking for a way to reliably probe the turbulent processes. The recent work by Lüthi introduced in his Ph.D. Thesis [6] and later applied to a direct numerical simulation [54] provides the methodology in which the familiar R-Q phase space can be extended through the decomposition of R, and it is this that I would like to discuss here.

The question Lüthi asked was how can we present the evolution of the enstrophy, dissipation and their production terms in three dimensional space? Starting from the R-Q phase space where we consider the linear combination of terms, it is only a natural progression to consider the decomposition of R, and a change in basis to represent the evolution of the (Q, R_S, R_ω) space. The primary benefit of moving to three-dimensional space is the ability to look for and visualise structures within the flow field, with the opinion that the R-Q model is too restricted neglecting

the effect the pressure has on the flow.

In 2002 [6] Lüthi undertook a three-dimensional particle tracking velocimetry experiment in the search of new underlying mechanisms of the turbulent flow, and obtains good results for tracking the velocities, and proceeds to expand the R-Q phase space to the (Q, R_S, R_ω) probability orbital. In 2009 Lüthi et al [54] published a paper on the expansion of the R-Q phase space, with the analysis applied to a data set from John Hopkins University. The conclusions drawn from this further study were that there exists a strong cyclic evolution, this behaviour we have seen in the R-Q phase space by considering the full evolution equations. Additionally, they claim that the pressure Hessian enhanced the growth of stretching in regions of high strain. With the overall conclusion that the evolution of the three dimension model provides a clearer evolution of the associated quantities in direct comparison to the R-Q phase space. It is known that the pressure Hessian affects the flow characteristics, but very little work has been done to try and understand this phenomena as discussed in Chapter 6.

7.1 Decomposing R

Anyone who studies turbulence cannot underestimate the importance of the enstrophy, dissipation and the associated production terms. It is the interplay between these quantities that had not been investigated until Lüthi [6]. If we take a moment to consider the convection of a vortex line throughout 3D turbulence, and how the velocity field is generated, then it follows that the velocity field is partly generated by the vorticity it is convecting.

In 1938 Taylor proposed that 3D turbulence exists due to vortex stretching, specifically that the ensemble average of the vortex stretching is positive $\langle R_\omega \rangle > 0$. This result is a consequence of the negative velocity

derivative skewness S_k measured by hot wire probes as far back as the 1950's. If you consider the evolution of vortex stretching and enstrophy production it is clear that they are formed from the various moments of interaction between the strain and vorticity.

In areas of high strain rate, the dissipation production term R_S , is dominant over R_ω , more so than dominance exerted by enstrophy production term over the dissipation production term observed in regions of maximal vorticity. The transfer of energy between scales and the eventual saturation of dissipation are all associated with the self amplification of the rate of strain production and vortex compression rather than with vortex stretching. Ashurst et al [4] comments that for enstrophy production the intermediate strain eigenvalue must be positive, however the regions of largest dissipation also fall under this condition, highlighting the importance of considering their individual dynamics.

Because closures generally fail to deal with the pressure Hessian accurately or completely neglect the effect of the Hessian. The use of third order moments R_ω and R_S provides a tool for understanding the interactions.

7.1.1 Distribution

Understanding the differences in the dynamical behaviour between the inclusion and neglect of the pressure Hessian is what will be studied here. Does any relationship exist between the individual moments before we consider the evolution in (Q, R_S, R_ω) space?

The comparison between the distribution of the restricted Euler model and the inclusion of the pressure Hessian for the three primary moments (Q, R_S, R_ω) is seen in figures 7.1, 7.2 and 7.3. The distribution when the Hessian is considered is slightly broader than the restricted Euler model in all three instances. Looking at these figures further, specifically figures 7.2 and 7.3 the quantities $\frac{dR_\omega}{dt}$ and $\frac{dR_s}{dt}$ appear to be positively

skewed, whilst $\frac{dQ}{dt}$ is centred around zero. These plots show that including the pressure Hessian does produce a different distribution to that of the Restricted Euler equations.

7.2 (Q, R_S, R_ω) Evolution

7.2.1 Q Evolution

Figure 7.4 shows the relationship between the restricted and full evolution equations for Q , conditioned on regions of vorticity for simulation B. There is a linear correlation between the isotropic assumption and the full pressure Hessian at $t = 0.3$ (top image in figure 7.4). At $t = 0.4$ there is a marked change in behaviour, the region of maximum vorticity is very centralised and the tails of the distribution are more rounded with a growth of the number of points in the central band. Similar behaviour is observed in simulation C as seen in figure 7.5. In both cases the slope of the graph looks to be greater than 1. This suggests that the growth of restricted model is less than that of the full equations.

The correlation coefficient r is a measure of the degree of correlation between two quantities, if $r = 1$ we would have a perfect linear relationship between the two quantities. We define r as follows:

$$r = \frac{S_{xy}}{\sqrt{S_{xx}S_{yy}}} \quad (7.1)$$

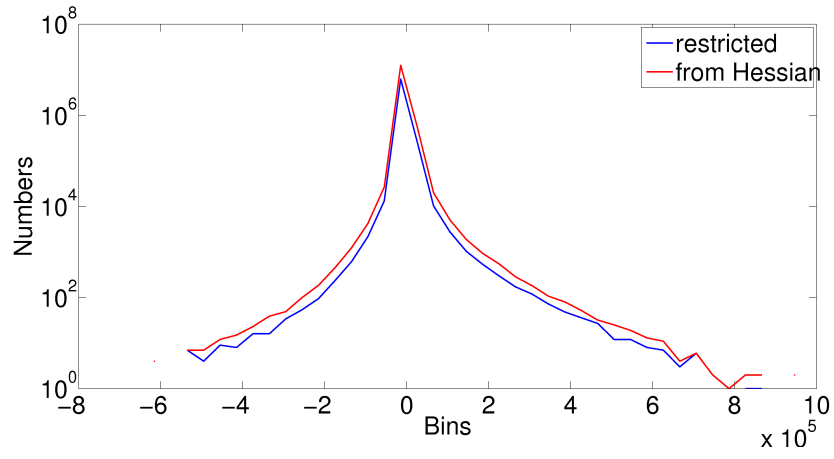


Figure 7.1: Comparison of $\frac{dQ}{dt}|_{Hessian}$ against $\frac{dQ}{dt}|_{Restricted}$.

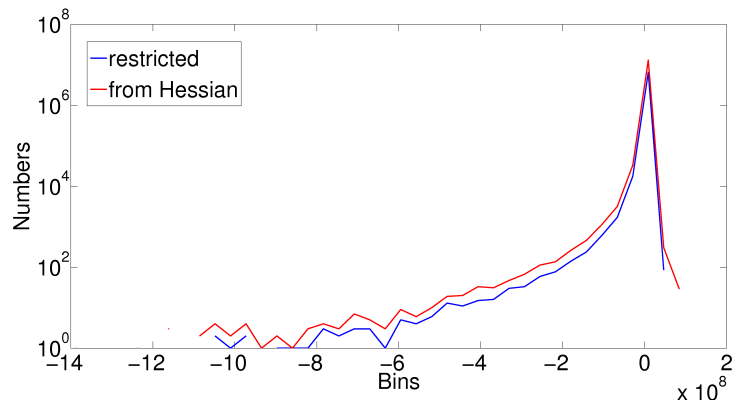


Figure 7.2: Comparison of $\frac{dR_{\omega}}{dt}|_{Hessian}$ against $\frac{dR_{\omega}}{dt}|_{Restricted}$.

Where S_{xx}, S_{yy} and S_{xy} are the sums of squares defined as follows:

$$S_{xx} = \sum_{i=1}^n x_i^2 - n\bar{x}^2, \quad (7.2)$$

$$S_{yy} = \sum_{i=1}^n y_i^2 - n\bar{y}^2, \quad (7.3)$$

$$S_{xy} = \sum_{i=1}^n x_i y_i - n\bar{x}\bar{y}. \quad (7.4)$$

$$(7.5)$$

Where:

$$\bar{x} = \frac{1}{n} \sum_{i=1}^n x_i. \quad (7.6)$$

Table 7.1 compares the values of r for figures 7.4 and 7.5. There is a good degree of correlation between $\frac{dQ}{dt}|_{Hessian}$ and $\frac{dQ}{dt}|_{Restricted}$ for runs B and C. In fact the values of r for both simulations is sufficient to confirm that $\frac{dQ}{dt}|_{Hessian}$ and $\frac{dQ}{dt}|_{Restricted}$ move together.

Statistically, we want to know what range of values r could possibly take. This is achieved by calculating the 95% two sided confidence interval for r using the Fisher Z transformation $z_r = \tanh^{-1} r$. The Fisher transform is used to test the correlation coefficient r when it is non zero as in this case; z_r can then be approximated by a normal distribution so that a confidence interval around r can be found. We will assume that the correlation coefficients approximately follow a normal distribution with mean z_o and variance $\frac{1}{n-3}$, note that n is the number of points in the sample. Hence:

$$z_r \approx \mathcal{N}\left(z_o, \left(\frac{1}{\sqrt{n-3}}\right)^2\right) \quad (7.7)$$

Here z_o is the population correlation coefficient, using the inverse normal distribution tables ϕ for $\pm 2.5\%$, $\phi(\pm 0.025) = \pm 1.96$. The interval

is calculated as: $\tanh z_o = \tanh \left(z_r \pm \frac{1.96}{\sqrt{n-3}} \right)$. z_r and the two-sided 95% confidence intervals for simulations B and C are listed in table 7.1.

The high value of $r > 0.75$ suggests that we have a reasonable linear fit in figures 7.4 and 7.5. Assuming a standard linear regression of the form $y_i = \beta x_i + c_i$ where c_i is the intercept with the y axis, and β is a measure of the slope. Then using maximum likelihood estimation we can find the standard deviation of the linear regression denoted $\hat{\sigma}$. It can then be shown that the variance of β is equal to $\text{var}(\beta) = \frac{\hat{\sigma}^2}{S_{xx}}$.

Applying this to 7.4 we assume that:

$$\frac{dQ}{dt}|_{Hessian} = \beta_Q \frac{dQ}{dt}|_{Restricted} + c \quad (7.8)$$

where β_Q is the gradient of the slope in figure 7.4 and c is the intersection with the vertical axis. This is of particular interest as the gradient quantifies the relationship between $\frac{dQ}{dt}|_{Hessian}$ and $\frac{dQ}{dt}|_{Restricted}$. The gradient is calculated as follows $\beta_Q = \frac{S_{xy}}{S_{xx}}$. Lets initially assume that $\beta_Q = 1$, that is the growth of $\frac{dQ}{dt}|_{Hessian}$ and $\frac{dQ}{dt}|_{Restricted}$ is equal. Then we can make an initial H_0 and alternative hypotheses H_1 :

$$H_0 : \beta = 1, \text{ The growth of } \frac{dQ}{dt}|_{Restricted} = \frac{dQ}{dt}|_{Hessian} .$$

$$H_1 : \beta \neq 1, \text{ The growth of } \frac{dQ}{dt}|_{Restricted} \neq \frac{dQ}{dt}|_{Hessian} .$$

These hypotheses can be tested using a two sided 95% confidence interval:

$$\left(\beta_Q - t_{n-2} \sqrt{\frac{\hat{\sigma}^2}{S_{xx}}}, \beta_Q + t_{n-2} \sqrt{\frac{\hat{\sigma}^2}{S_{xx}}} \right) . \quad (7.9)$$

Where t is the t-distribution, n is the number of points in the sample and $\hat{\sigma}^2 = \frac{1}{n-2} \left(S_{yy} - \frac{S_{xy}^2}{S_{xx}} \right)$, the maximum likelihood estimate of the standard deviation. The values of β_Q and the confidence interval are

tabulated in table 7.2. Here we can see that H_0 can be rejected since β_Q is greater than 1 in all cases. The rate of change in simulation B is not as consistent as in simulation C, it drops off from 1.4 at time $t = 0.3$ to a low of 1.12 at time $t = 0.5$ before increasing at time $t = 0.6$ to 1.5. Whereas in simulation C, β_Q fluctuates between 1.3 and 1.4. This suggests that there is possibly an underlying process driving the growth in $\frac{dQ}{dt}|_{Hessian}$ that is missing from $\frac{dQ}{dt}|_{Restricted}$.

What we are observing here is that $\frac{dQ}{dt}|_{Restricted}$ broadly follows $\frac{dQ}{dt}|_{Hessian}$ but the growth of $\frac{dQ}{dt}|_{Hessian}$ is approximately 1.3 times that of $\frac{dQ}{dt}|_{Restricted}$. Can we improve on $\frac{dQ}{dt}|_{Restricted}$? The observed growth is linear; so one could choose to modify $\frac{dQ}{dt}|_{Restricted}$ by placing it as the explanatory variable in a linear regression model. Looking at table 7.2 one could assume $\beta'_Q = 1.34$ (Here β'_Q is used to distinguish from β_Q calculated earlier), we will call this Trial 1.

Let $\overline{\frac{dQ}{dt}}|_{Hessian}$ and $\overline{\frac{dQ}{dt}}|_{Restricted}$ represent the mean of the Hessian and Restricted equations respectively. c can then be found:

$$c = \overline{\frac{dQ}{dt}}|_{Hessian} - \beta \overline{\frac{dQ}{dt}}|_{Restricted} = -13.74 \quad (7.10)$$

Leading us to:

$$\frac{dQ}{dt}|_{Trial1} = 1.34 \frac{dQ}{dt}|_{Restricted} - 13.74. \quad (7.11)$$

We now expect that $\beta'_Q \approx 1$, however there is still a large variation from the target $\beta = 1$ as seen in table 7.3.

Trial 2, lets assume the values grow according to:

$$\frac{dQ}{dt}|_{Trial2} = \beta''_Q(t) \frac{dQ}{dt}|_{Restricted}. \quad (7.12)$$

Here c has been omitted as it only acts to translate the distribution vertically, and let β_Q'' be the β for Trial 2. It is clear that β_Q'' changes with time. Let $\beta_Q''(t) = (1.4, 1.3, 1.2, 1.5)$ for the following values of $t = (0.3, 0.4, 0.5, 0.6)$. Then looking at table 7.3 one achieves a closer approximation to the growth of $\frac{dQ}{dt}|_{Hessian}$ using equation (7.12).

The current observations suggest that perhaps an analytical model could be used for $\beta(t)$ in a statistical linear regression model to improve on the current Restricted Euler equation for the evolution of Q . Figure 7.10 shows a comparison between β_Q for runs B and C. Here we see we have an almost analytic initial growth phase, with B peaking earlier than C before evolving to the more usual picture of turbulent growth. The middle and bottom images of Figure 7.10 have an polynomial of order 6 fitted to the β_Q data for runs B and C respectively. The missing components of the pressure Hessian in $\frac{dQ}{dt}|_{Restricted}$ act to increase the rate of growth and as such the restricted model underestimates the growth of $\frac{dQ}{dt}$.

The following model is suggested, it scales the value of $\frac{dQ}{dt}(t)|_{Restricted}$ so that it represents $\frac{dQ}{dt}(t)|_{Hessian}$. We will refer to this model as $\frac{dQ}{dt}|_{Scaled}$:

$$\frac{dQ}{dt}|_{Scaled} = \beta(t) \frac{dQ}{dt}(t)|_{Restricted} \quad (7.13)$$

Where $\beta(t) = 2500t^6 - 7600t^5 + 800t^4 - 3600t^3 + 64t^2 - 2.1t + 1.1$. Running this scaled model based on the statistical analysis we completed earlier we see that we still have a variation in the rate of growth between the scaled model $\frac{dQ}{dt}|_{Scaled}$ and $\frac{dQ}{dt}|_{Hessian}$ but the degree of variation has been reduced, table 7.4. Plotting time $t = 0.5$ in figure 7.11 it is apparent that β_Q works to increase the growth of $\frac{dQ}{dt}(t)|_{Restricted}$ whilst retaining the same degree of correlation between the modelled values and the full equations. Considering $t = 0.6$ in figure 7.12 we observe the same behaviour, although $\beta \neq 1$ the variation from 1 is less than that experienced previously.

7.2.2 R_ω Evolution

The change in behaviour of R_ω can be seen for simulations B and C in figures 7.6 and 7.7 respectively. Between $t = 0.3$ and $t = 0.4$ the linear relationship is significantly reduced with a shift in the angle between the two quantities which is more pronounced in the region where $\frac{dR_\omega}{dt}|_{Hessian}$ and $\frac{dR_\omega}{dt}|_{Restricted}$ are both positive. As the quantities evolve there is a clear preference for the Hessian case to have $\frac{dR_\omega}{dt}|_{Hessian} > 0$. Moreover, when $\frac{dR_\omega}{dt}|_{Restricted} < 0$ we typically have $\frac{dR_\omega}{dt}|_{Hessian} \approx 0$. This stepped change around 0 raises many questions, and in order to look at this I decided to split the domain into two regions based on the restricted model. For $\frac{dR_\omega}{dt}|_{Restricted} < 0$ and $\frac{dR_\omega}{dt}|_{Restricted} > 0$ we can define r_- and r_+ respectively, where:

$$r_- = \frac{S_{xy}|_{x_i, y_i < 0}}{\sqrt{S_{xx}|_{x_i, y_i < 0} S_{yy}|_{x_i, y_i < 0}}} \quad (7.14)$$

$$r_+ = \frac{S_{xy}|_{x_i, y_i \geq 0}}{\sqrt{S_{xx}|_{x_i, y_i \geq 0} S_{yy}|_{x_i, y_i \geq 0}}} \quad (7.15)$$

$$(7.16)$$

Considering the positive quadrant in figures 7.6 and 7.7 there appears to be reasonable correlation between the two values. The values of r , r_+ and r_- are tabulated in table 7.5. The overall correlation r shows no consistency between the times, the degree of correlation in the region of $\frac{dR_\omega}{dt}|_{Restricted} < 0$ is very low, in fact for Run C there is no correlation. However the region $\frac{dR_\omega}{dt}|_{Restricted} > 0$ does show a good degree of correlation between the times as detailed in table 7.5.

Linear regression is applied to fit the model by setting the negative values equal to zero and the positive values to $\beta_{R_\omega} \frac{dR_\omega}{dt}|_{Restricted}$ then letting $\beta_{R_\omega} = (1.02, 0.66, 0.73, 0.7)$ the growth of the restricted Euler model can be aligned with the full model as seen in table 7.7. Plotting $\beta_{R_\omega}^+$ for

all times as seen in Figure 7.13, it is observed that the growth of $\frac{dR_\omega}{dt}$ is overestimated initially, before underestimating the growth of the full equations at later times. If we fit the data to an analytic curve we arrive at the following model:

$$\frac{dR_\omega}{dt}|_{Scaled} = \begin{cases} 0, & \text{if } \frac{dR_\omega}{dt} \leq 0 \\ \beta_{R_\omega}(t) \frac{dR_\omega}{dt}|_{Restricted}, & \text{if } \frac{dR_\omega}{dt} > 0. \end{cases} \quad (7.17)$$

Where $\beta_{R_\omega}(t) = 1.8t^2 - 2.3t + 1.3$.

7.2.3 R_S Evolution

The third component $\frac{dR_s}{dt}$ as seen in figures 7.6 and 7.7 at $t = 0.3$ again appears to initially have a linear relationship however past $t=0.4$ the behaviour changes significantly, and it appears that $\frac{dR_s}{dt}|_{Hessian}$ and $\frac{dR_s}{dt}|_{Restricted}$ are decorrelated. As such no amendment to the model is suggested.

7.3 Pressure Hessian

In Chapter 6 the notion of a conditional mean trajectory was introduced, following on from the work of Ooi et al [45]. In three-dimensional space the original equations are reformulated in terms of the (Q, R_S, R_ω) space.

$$\dot{\mathbf{R}}_S(Q, \mathbf{R}_\omega, \mathbf{R}_S) = \left\langle \frac{d\mathbf{R}_S}{dt} \middle| \overline{Q}, \overline{R_\omega}, \overline{R_S} \right\rangle, \quad (7.18)$$

$$= \frac{1}{N} \sum_{Q^-}^{Q^+} \sum_{R_\omega^-}^{R_\omega^+} \sum_{R_S^-}^{R_S^+} \frac{d\mathbf{R}_S}{dt}(\mathbf{Q}, \mathbf{R}_\omega, \mathbf{R}_S) \quad (7.19)$$

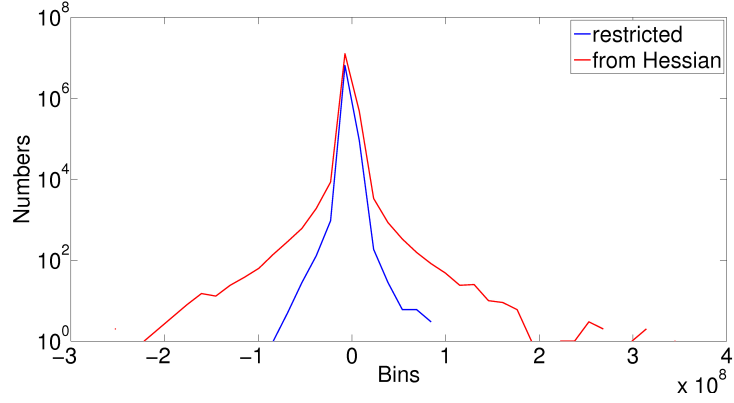


Figure 7.3: Comparison of $\frac{d\mathbf{R}\mathbf{S}}{dt}|_{Hessian}$ against $\frac{d\mathbf{R}\mathbf{S}}{dt}|_{Restricted}$.

Simulation	Time	r	z_r	Confidence Interval
B	0.3	0.9167	1.5681	(0.9161,0.9173)
C	0.3	0.8783	1.3684	(0.8775,0.8792)
B	0.4	0.7695	1.0192	(0.7680,0.7711)
C	0.4	0.8133	1.1368	(0.8120,0.8146)
B	0.5	0.8548	1.2738	(0.8538,0.8559)
C	0.5	0.8078	1.1208	(0.8065,0.8092)
B	0.6	0.9377	1.7184	(0.9372,0.9381)
C	0.6	0.9013	1.4792	(0.9006,0.9020)

Table 7.1: This table compares the values of r , z_r and the 95% confidence interval for r at key times for runs B and C.

Time	Simulation	β_Q	Confidence Interval	Accept/Reject H_0
0.3	B	1.3793	(1.3770,1.3816)	Reject
0.3	C	1.4308	(1.4278,1.4337)	Reject
0.4	B	1.2981	(1.2940,1.3023)	Reject
0.4	C	1.3101	(1.3065,1.3137)	Reject
0.5	B	1.1220	(1.1194,1.1246)	Reject
0.5	C	1.3678	(1.3639,1.3716)	Reject
0.6	B	1.5137	(1.5116,1.5116)	Reject
0.6	C	1.3915	(1.3889,1.3940)	Reject

Table 7.2: The values of β_Q , 95% Confidence Interval and Hypothesis Test result for figures 7.4 and 7.5

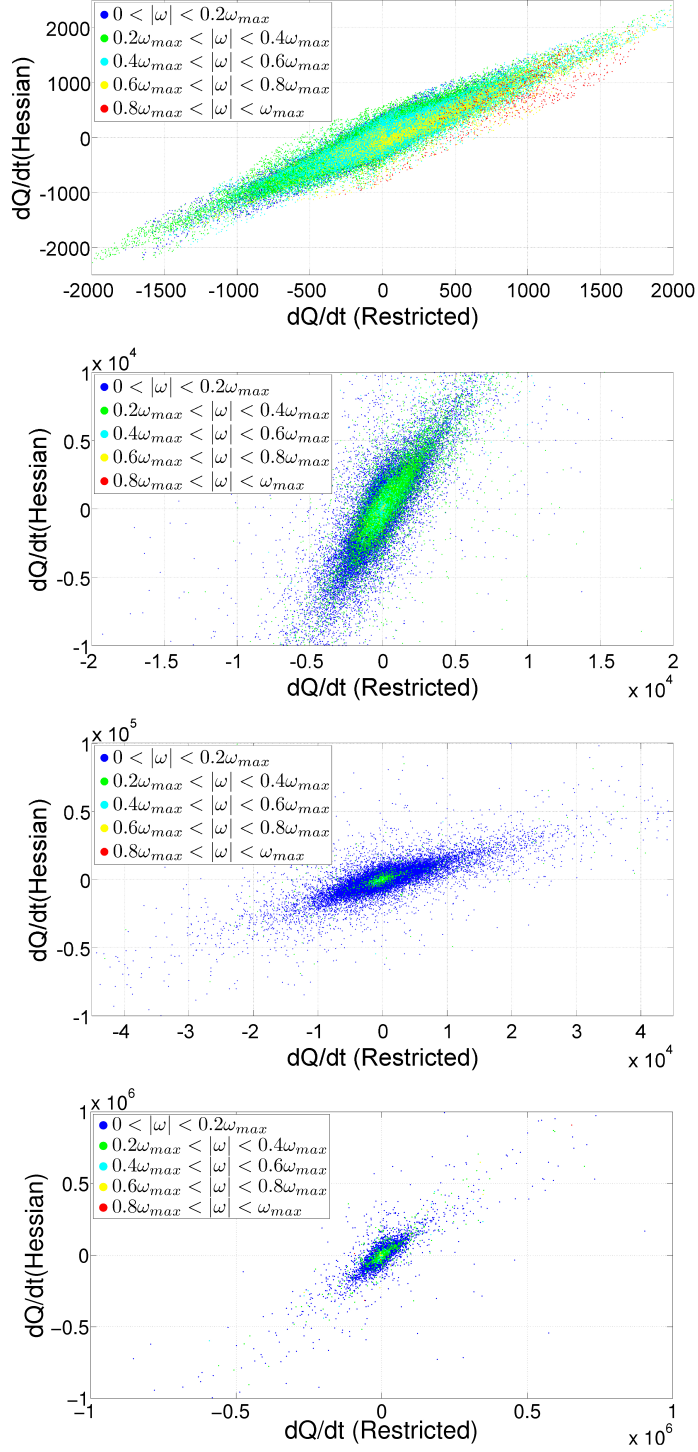


Figure 7.4: The above images compare the relationship between the isotropic assumption for the pressure Hessian and the full pressure Hessian in the evolution equation for the second invariant Q from Simulation B from $t=0.3$ (top) until $t=0.6$ (bottom).

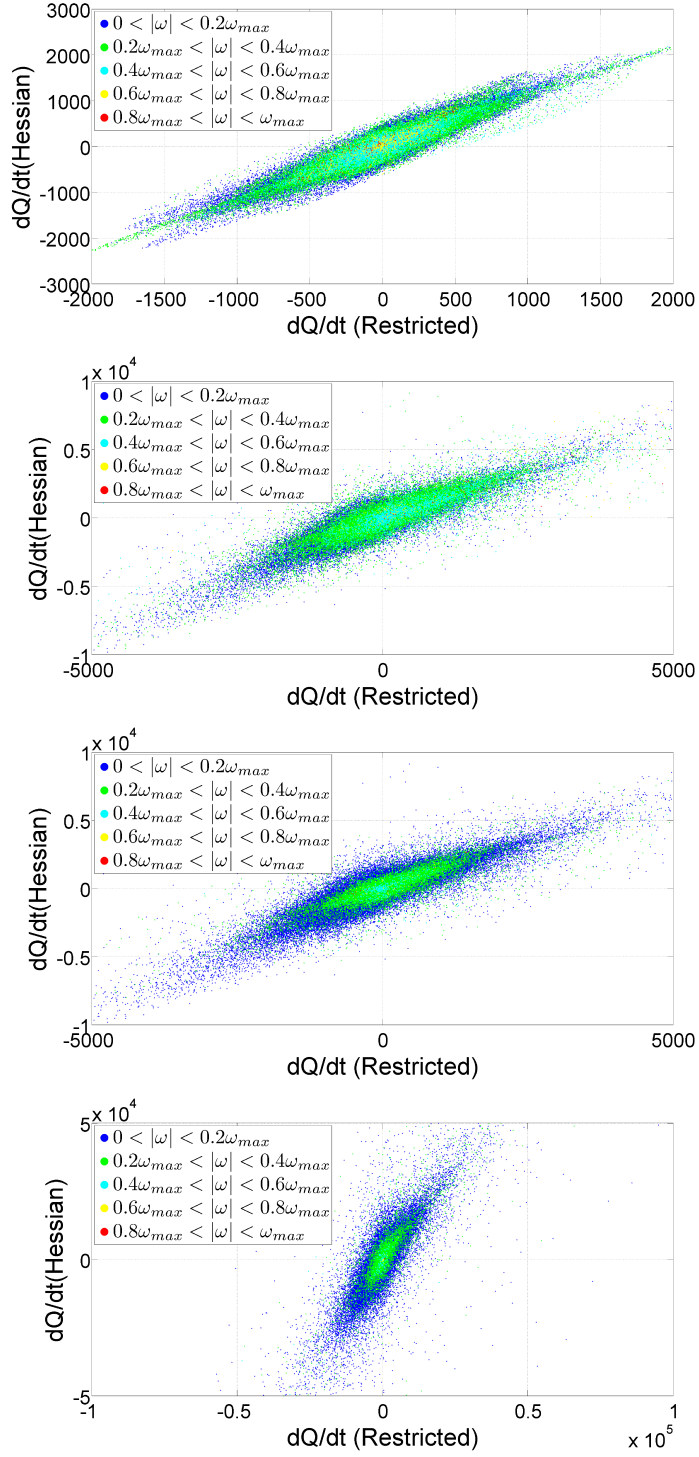


Figure 7.5: The above images compare the relationship between the isotropic assumption for the pressure Hessian and the full pressure Hessian in the evolution equation for the second invariant Q from Simulation C from $t=0.3$ (top) until $t=0.6$ (bottom).

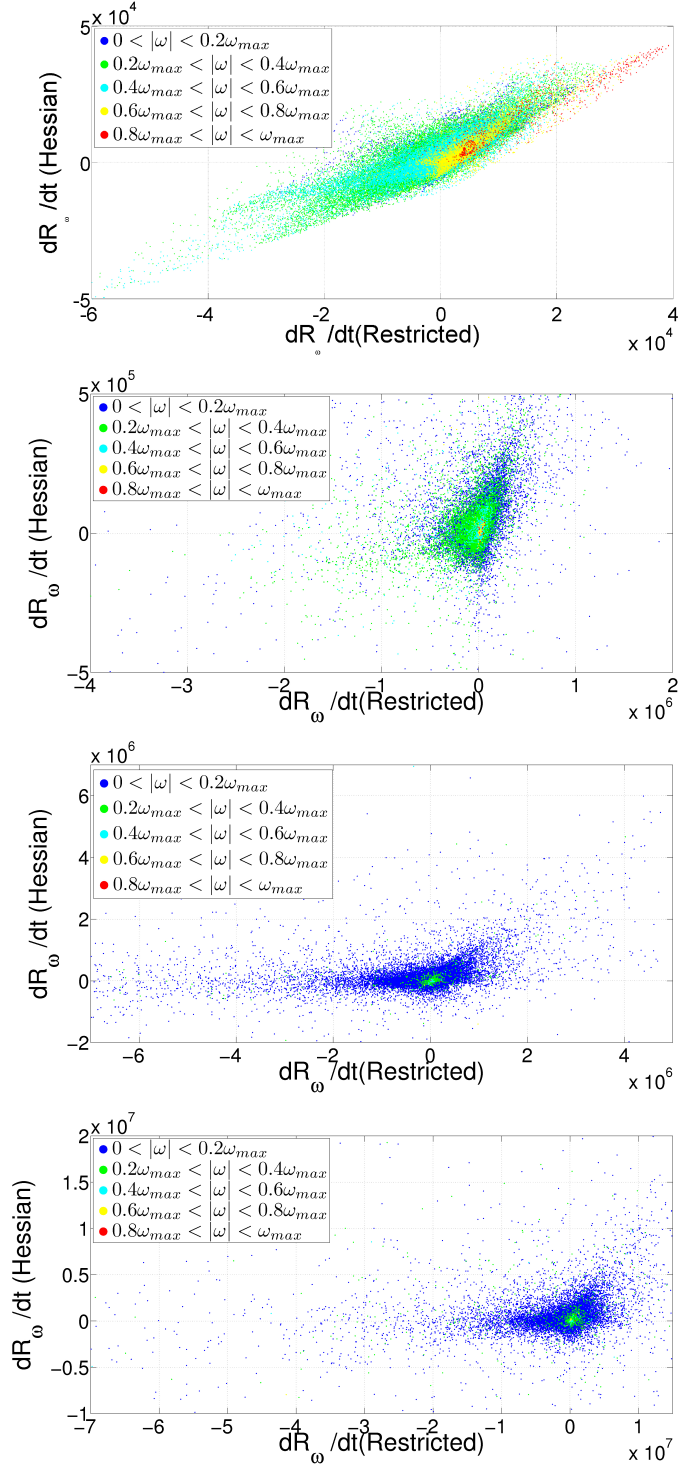


Figure 7.6: The above images compare the relationship between the isotropic assumption for the pressure Hessian and the full pressure Hessian in the evolution equation for \mathbf{R}_ω from Simulation B from $t=0.3$ (top) until $t=0.6$ (bottom).

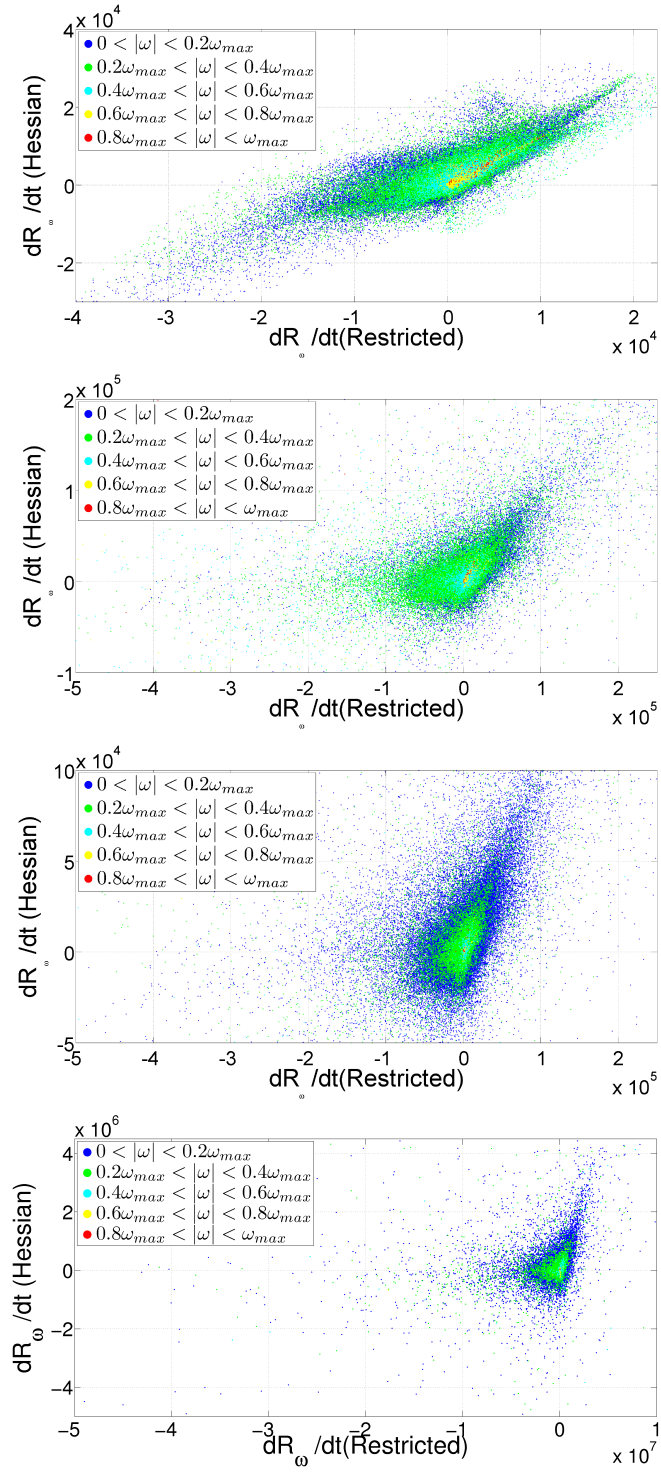


Figure 7.7: The above images compare the relationship between the isotropic assumption for the pressure Hessian and the full pressure Hessian in the evolution equation for \mathbf{R}_ω from Simulation C from $t=0.3$ (top) until $t=0.6$ (bottom).

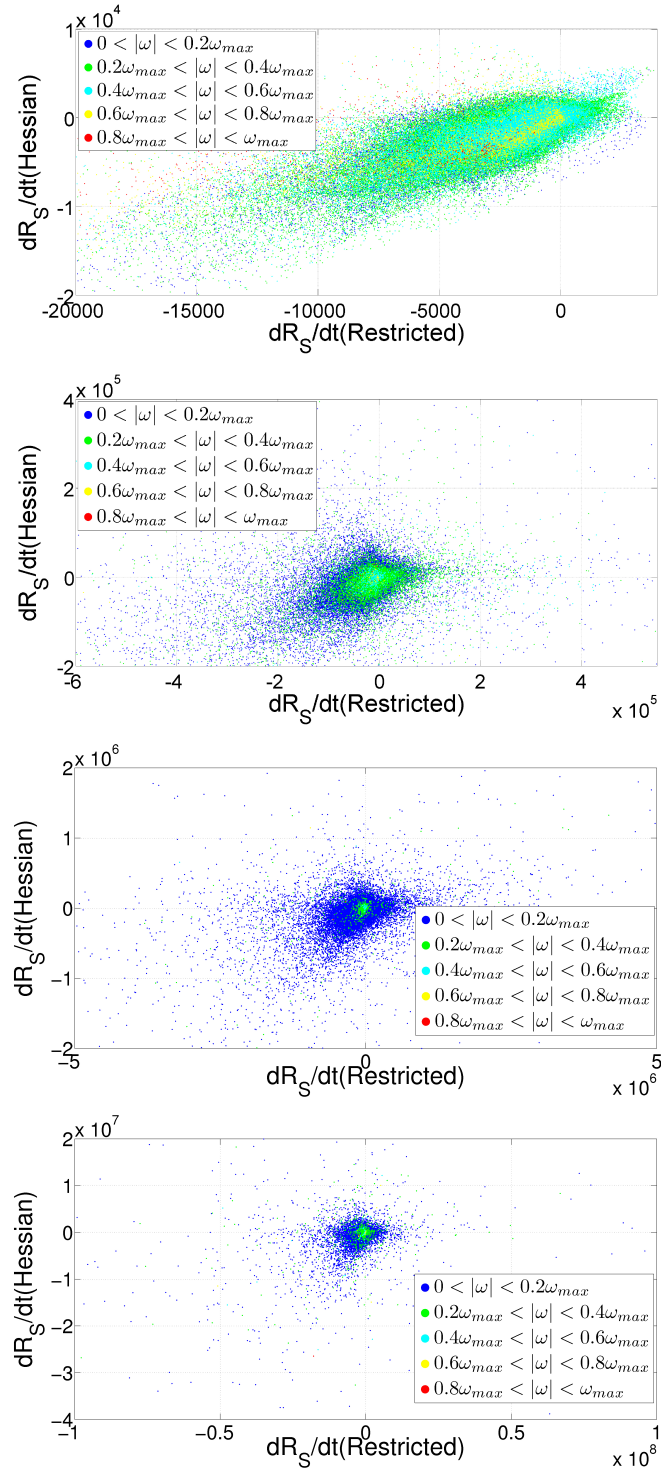


Figure 7.8: The above images compare the relationship between the isotropic assumption for the pressure Hessian and the full pressure Hessian in the evolution equation for \mathbf{R}_S from Simulation B from $t=0.3$ (top) until $t=0.6$ (bottom).

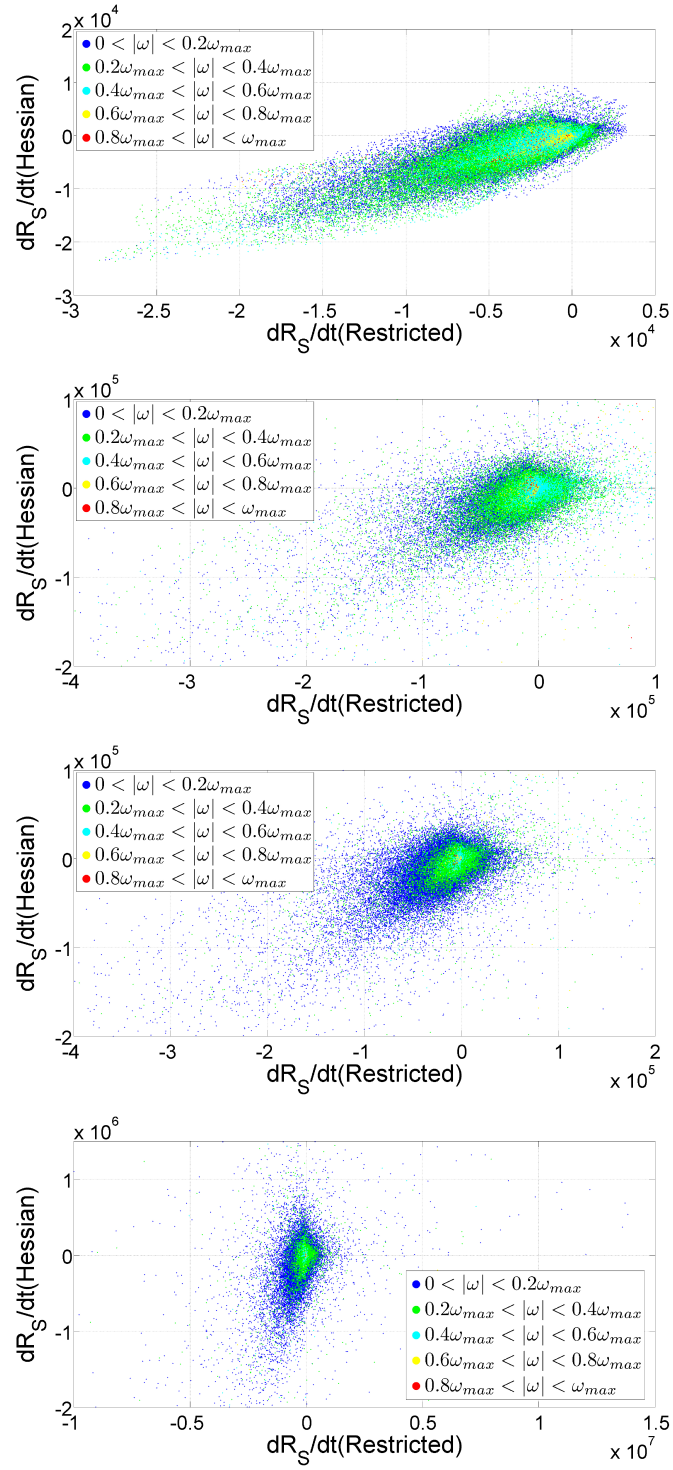


Figure 7.9: The above images compare the relationship between the isotropic assumption for the pressure Hessian and the full pressure Hessian in the evolution equation for \mathbf{R}_S from Simulation C from $t=0.3$ (top) until $t=0.6$ (bottom).

Simulation	Time	r	β_Q	β'_Q	β''_Q
B	0.3	0.9167	1.3793	1.0294	0.9852
B	0.4	0.7695	1.2981	0.9688	0.9986
B	0.5	0.8548	1.1220	0.8373	0.9350
B	0.6	0.9377	1.5137	1.1297	1.0092

Table 7.3: This table compares the values of r , β_Q , β'_Q and β''_Q for run B.

Simulation	Time	β_Q^{Scaled}	β_Q
B	0.3	0.9847	1.3793
B	0.4	1.1103	1.2981
B	0.5	0.9508	1.1220
B	0.6	1.1570	1.5137

Table 7.4: A comparison between β_Q and β_Q^{Scaled} for run B.

Simulation	Time	r	r_-	r_+
B	0.3	0.4664	0.2688	0.8328
C	0.3	0.5915	0.0491	0.8632
B	0.4	0.1688	-0.0839	0.7691
C	0.4	0.2898	0.0248	0.8361
B	0.5	-0.4614	-0.5839	0.6642
C	0.5	0.0410	-0.1891	0.8287
B	0.6	0.2659	0.1971	0.8807
C	0.6	0.0537	0.0071	0.7919

Table 7.5: Correlation coefficients for runs B and C for R_ω at key times. r is the standard correlation coefficient, r_- is the correlation coefficient in the region $\frac{dR_\omega}{dt}|_{Restricted} < 0$ and r_+ is the correlation coefficient in the region $\frac{dR_\omega}{dt}|_{Restricted} \geq 0$.

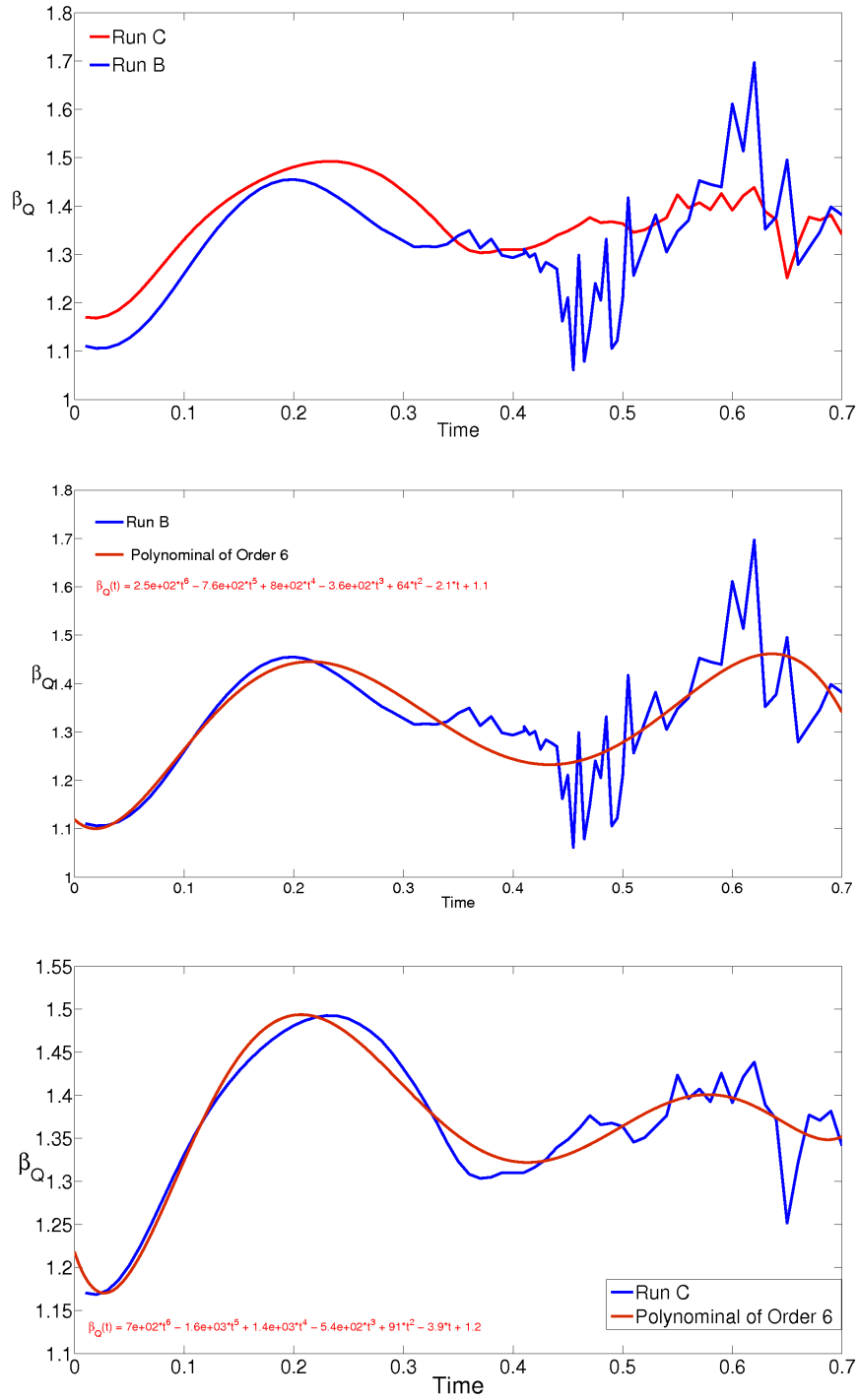


Figure 7.10: (top) A comparison between run B and run C is made for the value of β_Q . (middle) A 6th order polynomial is fitted to β_Q for run B. (bottom) A 6th order polynomial is fitted to β_Q for run C.

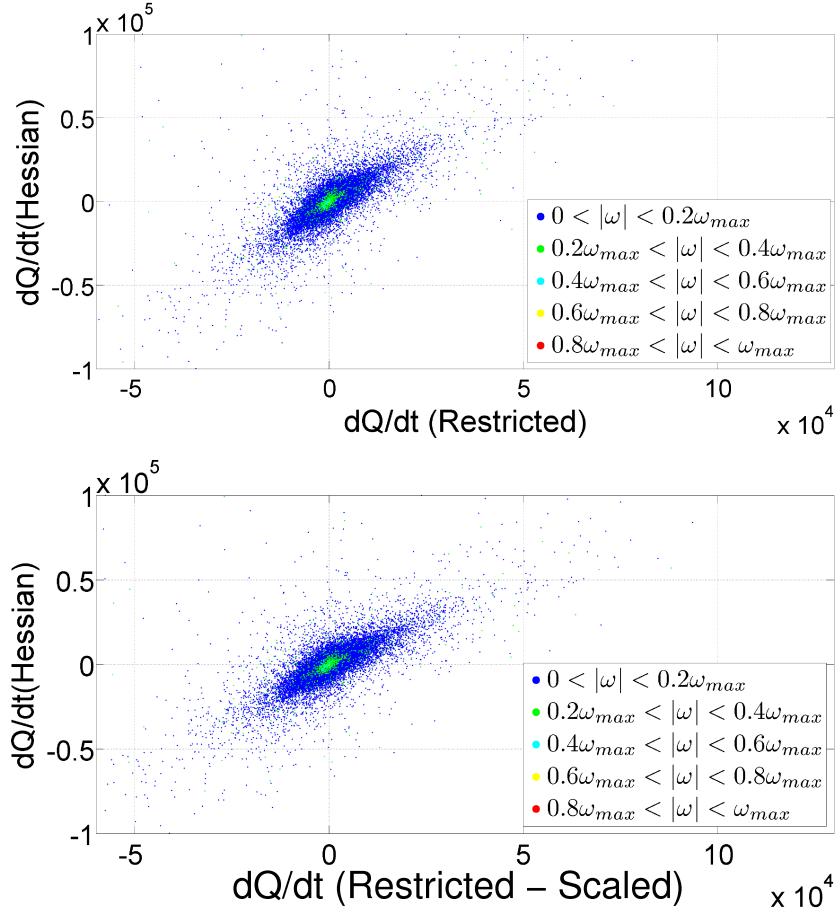


Figure 7.11: The top plot is Run B at $t = 0.5$, here we compare $\frac{dQ}{dt}(t)|_{\text{Restricted}}$ and $\frac{dQ}{dt}(t)|_{\text{Hessian}}$ (top) against $\frac{dQ}{dt}(t)|_{\text{Hessian}}$ and $\frac{dQ}{dt}(t)|_{\text{Scaled}}$ (bottom) observing a reduction in the slope of the distribution, that it $\frac{dQ}{dt}(t)|_{\text{Scaled}}$ closer to $\frac{dQ}{dt}(t)|_{\text{Hessian}}$.

Simulation	Time	$\beta_{R_\omega}^{\text{Scaled}}$	β_{R_ω}
B	0.3	1.0848	1.0244
B	0.4	1.0162	0.6621
B	0.5	1.1820	0.7253
B	0.6	1.2362	0.7046

Table 7.6: A comparison between β_{R_ω} and $\beta_{R_\omega}^{\text{Scaled}}$ for run B.

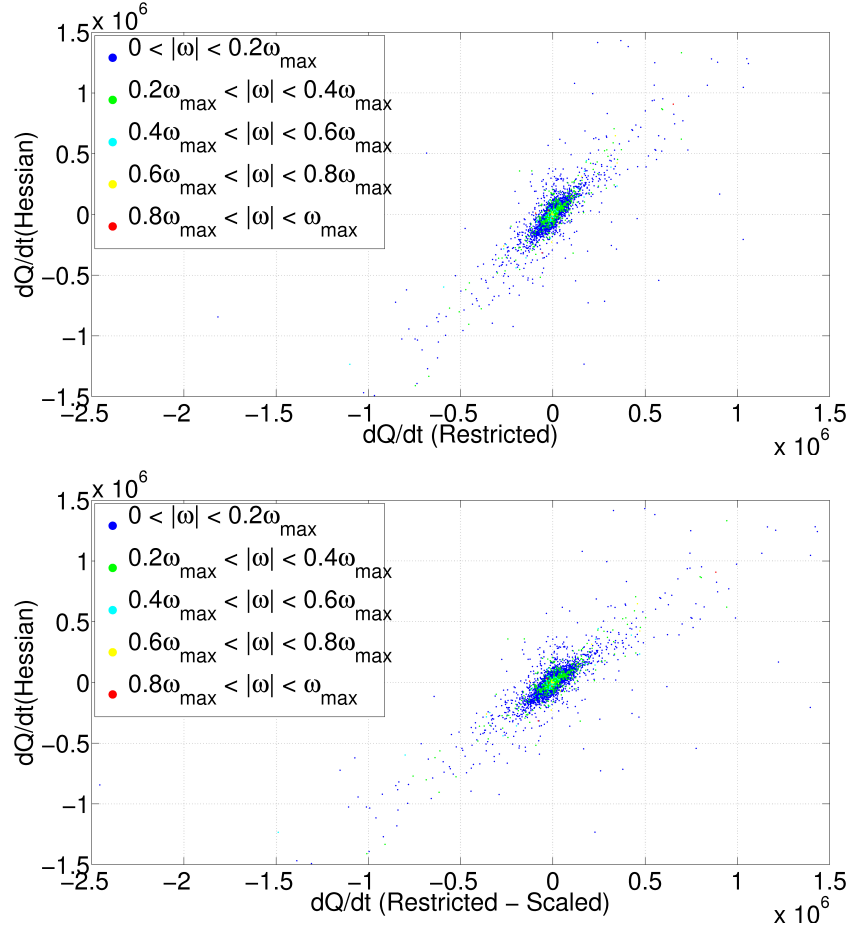


Figure 7.12: The top plot is Run B at $t = 0.6$, here we compare $\frac{dQ}{dt}(t)|_{Restricted}$ and $\frac{dQ}{dt}(t)|_{Hessian}$ (top) against $\frac{dQ}{dt}(t)|_{Hessian}$ and $\frac{dQ}{dt}(t)|_{Scaled}$ (bottom) observing a reduction in the slope of the distribution bringing $\frac{dQ}{dt}(t)|_{Scaled}$ closer to $\frac{dQ}{dt}(t)|_{Hessian}$.

Simulation	Time	r_+	$\beta_{R\omega}^+$	$\beta'_{R\omega}^+$
B	0.3	0.8328	1.0244	1.0043
B	0.4	0.7691	0.6621	1.0031
B	0.5	0.6642	0.7253	0.9936
B	0.6	0.8807	0.7046	1.0066

Table 7.7: This table compares the values of r , $\beta_{R\omega}^+$, $\beta'_{R\omega}^+$ for run B.

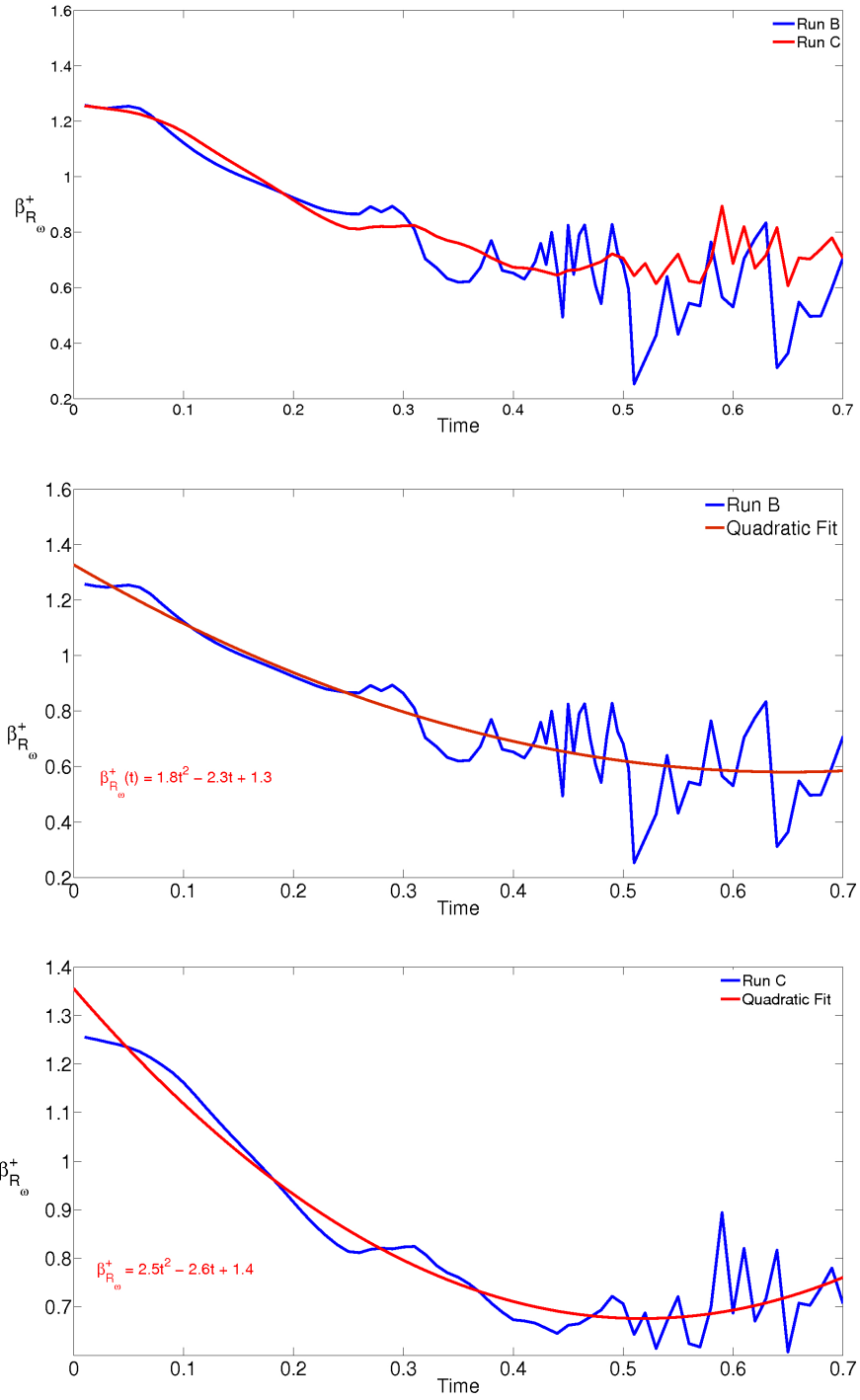


Figure 7.13: (top) A comparison between run B and run C is made for the value of $\beta_{R_\omega}^+$. (middle) A quadratic is fitted to $\beta_{R_\omega}^+$ for run B. (bottom) A quadratic is fitted to $\beta_{R_\omega}^+$ for run C.

Where N is the number of points in the ijk^{th} centred bin. $\overline{Q}^{\pm} = \overline{Q} \pm \frac{\Delta Q}{2}$ represents the upper and lower limit of the bin respectively where \overline{Q} is the mean and ΔQ is the bin width.

We have concluded that there are differences in the behaviour between the Hessian and restricted equations as illustrated in the comparison above and by the change in R-Q behaviour as previously discussed. If we consider the early times, as in figure 7.14 we see a similar picture to earlier observations in the R-Q phase space.

The Vieillefosse trajectories appear to be integrable, whereas the Hessian plot looks significantly more turbulent, the purpose of these plots is to reaffirm the differences seen in Chapter 6, between the Vieillefosse equations and the full equations.

7.4 Summary

The set of equations $\left(\frac{d\mathbf{Q}}{dt}, \frac{d\mathbf{R}_{\omega}}{dt}, \frac{d\mathbf{R}_S}{dt}\right)|_{Restricted}$ provide an approximation to $\left(\frac{d\mathbf{Q}}{dt}, \frac{d\mathbf{R}_{\omega}}{dt}, \frac{d\mathbf{R}_S}{dt}\right)|_{Hessian}$. However we have shown that the approximation can be improved for $\frac{d\mathbf{Q}}{dt}$ and $\frac{d\mathbf{R}_{\omega}}{dt}$ and as such the correlation between the RE and full equations can be improved. However further work on a suitable model is needed. If the variation in β_Q and $\beta_{R_{\omega}}$ could be approximated by another RE invariant or combination of invariants for the developing flow then this new model would be a closer match and would be suitable for use where a closure for the pressure is required. Therefore any new model would require \mathbf{Q} , \mathbf{R}_{ω} and \mathbf{R}_S as its foundation. The difference between the Hessian and Restricted evolution equations could possibly be expressed in terms of the five velocity moments $(\omega, S^2, I_4, \mathbf{R}_{\omega}, \mathbf{R}_S)$ or perhaps a combination of variables may prove more successful at explaining the difference. The solution will probably be most easily found by considering the variables driving

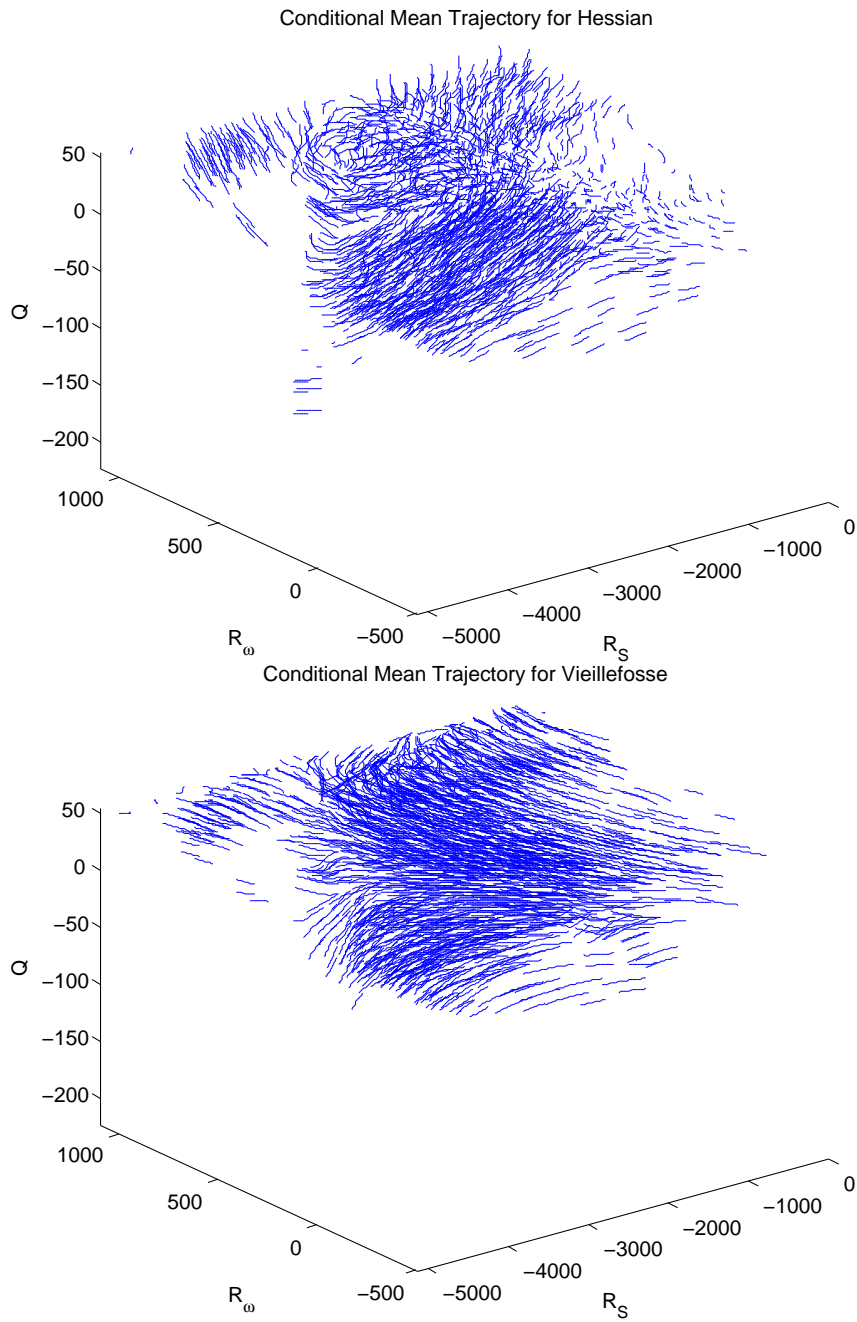


Figure 7.14: The above compares the Vieillefosse and Full equation trajectories at $t=0.3$ for dataset B. Here the paths appear to be much more regimented in the Vieillefosse assumption, with the full equations showing the swirling interactions we would expect from a developing flow.

the growth through the various development stages as described [30]. In chapter 8 we reflect on the work discussed within this thesis and provide a definition of an "Intense Event".

Chapter 8

Conclusions

The Vieillefosse model was revisited to investigate the difference between the local and non local effects of the pressure for a developing turbulent flow. Rather than doing this analysis on a forced, homogeneous, isotropic data set, the calculations start from smooth initial conditions that develop intense events characterised by large increases in the maximum vorticity and enstrophy. The goal was to understand how the usual statistics develop as well as lay the ground-work for an improved understanding of intermittent features.

The Hessian analysis began by comparing how the velocity moments develop and interact with each other. The classic tear-drop shape of the R-Q phase space was reproduced in figure 5.6. To provide a context for the later analysis, consideration was given to the velocity moments conditioned on regions of low to high intensity in figures 5.7 to 5.12. It was observed that the region of maximum vorticity at $t = 0.6$ is somewhat diminished when compared to $t = 0.3$ and the majority of the points on the Vieillefosse discriminant relate to regions of low vorticity whereas the regions of maximum dissipation predominantly act along the Vieillefosse discriminant.

Next the RE equations were compared to the pressure Hessian equations using conditional mean trajectories (CMTs). Starting at the early

time of $t = 0.3$, for all datasets, figures 6.3 (right) and 6.6 (top row) there is some tendency for the trajectories using the full Hessian to flow clockwise in the upper half $Q > 0$ plane as in the RE model, whilst along the Vieillefosse discriminant, the full Hessian trajectories cross it directly and tend to flow back around and be attracted to $R = Q = 0$. This strong deviation from the RE prediction could be because the structures are as far as possible from the vortex tube configurations that are associated with RE type statistics.

The tendency towards the RE trajectories continues at $t = 0.4 - 0.5$ for dataset A, figure 6.4 (right) and $t = 0.5$ dataset C, figure 6.6 (third row, right). In the lower right quadrant, the trajectories now clearly flow along the Vieillefosse discriminant, whilst within a distinct region with $0 < Q < 2000$ the trajectories circulate with a slight attraction to $(R, Q) = (0, 1000)$ and about $R = Q = 0$, the trajectories flow smoothly about this centre into the Vieillefosse discriminant. By $t = 0.6$ the full Hessian trajectories are almost indistinguishable from the RE trajectories.

The trends towards RE are faster for the higher Reynolds number in dataset B. In the lower right quadrant, the trajectories start to flow along the Vieillefosse discriminant at $t = 0.4$ as they begin to flow around the point $(R, Q) = (0, 500)$ with a slight attraction into that point in figure 6.6 (second row left). For $t = 0.5$ and $t = 0.6$, the full Hessian trajectories are close to the RE trajectories expectations. Thus, the trajectories for all the data sets in figures 6.5 and 6.6 (row 4) are similar those for the RE model given in figure 2.1 in Chapter 2. This analysis suggests that during the development phase there is a marked difference in the flow trajectories before and after a reconnection event.

8.1 Evidence for a Model

Consideration is then given to the work of Lüthi [54], where the traditional R-Q phase space is extended into three-dimensions. Here we compared the evolution equations for $\left(\frac{d\mathbf{Q}}{dt}, \frac{d\mathbf{R}_\omega}{dt}, \frac{d\mathbf{R}_S}{dt}\right)|_{Restricted}$ and $\left(\frac{d\mathbf{Q}}{dt}, \frac{d\mathbf{R}_\omega}{dt}, \frac{d\mathbf{R}_S}{dt}\right)|_{Hessian}$. It was observed that the Restricted equations have narrower probability distributions to the full Hessian equations, figures 7.1 to 7.3.

However it was shown that the RE prediction can be improved for $\frac{d\mathbf{Q}}{dt}$ and $\frac{d\mathbf{R}_\omega}{dt}$ by using them as an explanatory variable in a linear regression model. However further work on a suitable model is needed, as the underlying fluctuation between the two species needs to be modelled. That is, if the variation in β_Q and β_{R_ω} could be approximated by another RE invariant or combination of invariants for the developing flow then this new model would be a closer match and would be suitable for use where a closure for the pressure is required. Therefore any new model would require \mathbf{Q} , \mathbf{R}_ω and \mathbf{R}_S as its foundation. The difference between the Hessian and Restricted evolution equations could possibly be expressed in terms of the five velocity moments $(\omega, \mathbf{S}^2, \mathbf{I}_4, \mathbf{R}_\omega, \mathbf{R}_S)$ or perhaps a combination of variables may prove more successful at explaining the difference.

8.2 Role of the Intense Events

What is the role of the intense events? And what defines intense events? Is it just the reconnection, or should we be including the dynamics before and after the actual reconnection? For calculations that start from a smooth initial condition, intense events are usually characterised by large increases in the maximum vorticity or enstrophy. However associating these large increases with an event is difficult as the time over

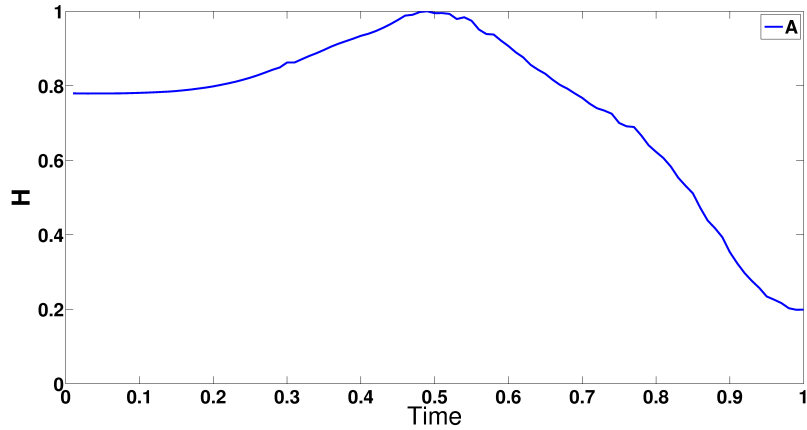


Figure 8.1: The global helicity, H for calculation A.

which the maximum vorticity or enstrophy grows is significantly longer than the time taken for a reconnection, defined in symmetric situations by changes in the circulation [55]. Therefore, in an asymmetric flow, if the reconnection event is due to a change in the topology, what measure can be used to identify this? Holm and Kerr [30] use the global helicity H , looking at the period $0.3 \leq t \leq 0.5$ in figure 8.1 you can see that there is a increase in the helicity during this period which coincides with the recycling of trajectories, figure 6.4 in Chapter 6.

In summary, the traditional quantities continue to grow long after the reconnection event has finished, as such an "Intense Event" is an event that causes a topological change identified by a peak in the global helicity. In a private communication R M Kerr has results that suggest that the best definition of an intense event in time is the global enstrophy production, stating that reconnection is only complete when this peaks, both globally and locally. As such the dynamics during periods of intense events are different to those experienced outside of these periods. An interesting topic of future work would be the consideration of how the flow can be modelled during these periods.

8.3 Further Work

Aside from the theoretical application of this study if provided with the opportunity I would like to consider the role of the pressure Hessian in the Lighthill equations. The Lighthill equations [1] describe how sound is produced aerodynamically.

There is renewed interest in the study of Aeroacoustics with many organisations looking on methods of reducing aircraft noise. The motivation for further study in this field would be uncovering structures that produce sound aerodynamically. The work on 'Recombination of vortex filaments and its role in aerodynamic noise' [56] would be a suitable starting point for continued study.

Bibliography

- [1] Lighthill, M.J. On sound generated aerodynamically,1. General Theory, Proc. Roy. Soc. London, A211, 564-587, 1952.
- [2] P. Vieillefosse, Internal motion of a small element of fluid in an inviscid flow, Physica A 125, 150 (1984).
- [3] L. Chevillard, C. Meneveau, Intermittency and universality in a Lagrangian model of velocity gradients in three-dimensional turbulence. C. R. Mecanique 335, 187-193 (2007)
- [4] W. T. Ashurst, A. R. Kerstein, R. M. Kerr, C. H. Gibson, Alignment of vorticity and scalar gradient with strain rate in simulated Navier-Stokes turbulence. 1987 Phys. Fluids 30 2343.
- [5] R. M. Kerr, "Histograms of helicity and strain in numerical turbulence." Phys. Rev. Let. **59**, 783 (1987).
- [6] B. Lüthi, Some Aspects of Strain, Vorticity and Material Element Dynamics as Measured with 3D Particle Tracking Velocimetry in a Turbulent Flow. PhD Thesis 2002.
- [7] C. L. M. H. Navier (1822), "Memoire sur les lois du mouvement des fluides", Mem. Acad. Sci. Inst. France, 6, 389-440.
- [8] P. Vieillefosse, Local interaction between vorticity and shear in a perfect incompressible fluid, J. Phys. (Paris) 43, 837 (1982).
- [9] Orszag, S. A., Fluid Dynamics, 1977.

- [10] Brissaud, A., Frisch, U., Leorat, J., Lesieur, M., Mazure, A., Pouquet, A., Sadourny, R. and Sulem, P.L.m Ann Geophys. 29(1973) 539.
- [11] Morf, R. H., Orszag, S. A. and Frisch, U. Phys. Rev. Lett. 44 (1980) 572.
- [12] E.D. Siggia, “Invariants for the one-point vorticity and strain rate correlations” Phys. Fluids **24**, 1934 (81).
- [13] J.D. Gibbon, “A quaternionic structure in the three-dimensional Euler and ideal magneto-hydrodynamics equation.” Physica D **166**, 17 (2002).
- [14] R. M. Kerr, “Higher order derivative correlations and the alignment of small-scale structures in isotropic numerical turbulence.” *J. Fluid Mech.* **153**, 31 (1985).
- [15] E.D. Siggia, “Numerical study of small scale intermittency in three-dimensional turbulence” J. Fluid Mech. **107**, 375 (81).
- [16] H. Tennekes and J. L. Lumley, A First Course in Turbulence, MIT Press, 1972.
- [17] M. S. Chong, A. E. Perry and B. J. Cantwell, A general classification of three-dimensional flow fields, Phys. Fluids A 2 (5) 1990.
- [18] Yi Li and Charles Meneveau, Material deformation in a restricted Euler model for turbulent flows: Analytic solution and numerical tests, Phys. Fluids 19, 015104 (2007).
- [19] M. Chertkov, A. Pumir, and B. I. Shraiman, Lagrangian tetrad dynamics and the phenomenology of turbulence, Phys. Fluids 11, 2394 1999 .
- [20] S. S. Girimaji and S. B. Pope, A diffusion model for velocity gradients in turbulence, Phys. Fluids A 2 (2) 1990.

- [21] Oscar Gonzalez and Andrew M. Stuart, A First Course in Continuum Mechanics, CUP,(2008).
- [22] L. Chevillard, C. Meneveau, L. Biferale and F. Toschi, Modeling the pressure Hessian and viscous Laplacian in Turbulence: comparisons with DNS and implications of velocity gradient dynamics, Phys. Fluids 20, 101504 (2008).
- [23] S. A. Orszag and G. S. Patterson, Numerical Simulation of Three-Dimensional Homogeneous Isotropic Turbulence, PRL 28 (2), 1972.
- [24] Rogallo, R. S. 1981, Numerical Experiments in Homogeneous Turbulence. NASA Technical Report TM81315.
- [25] Mitsuo Yokokawa, Ken'ichi Itakura, Atsuya Uno, Takashi Ishihara, and Yukio Kaneda. 2002. 16.4-Tflops direct numerical simulation of turbulence by a Fourier spectral method on the Earth Simulator. In Proceedings of the 2002 ACM/IEEE conference on Supercomputing (Supercomputing '02). IEEE Computer Society Press, Los Alamitos, CA, USA, 1-17.
- [26] J. Jiménez, A. A. Wray, P. G. Saffman and R. S. Rogallo, The structure of intense vorticity in isotropic turbulence, J. Fluid Mech. 255 (65-90) 1993.
- [27] U.Frisch, Turbulence, The legacy of A. N. Kolmogorov,CUP, 1995.
- [28] Jackson R. Herring and Robert M. Kerr, Development of enstrophy and spectra in numerical turbulence, Phys. Fluids A 5 (11) 1993.
- [29] M. Lesieur, Turbulence in Fluids 4th Edition, Springer.
- [30] D. D. Holm and R. M. Kerr Helicity in the formation of Turbulence, Phys. Fluids 19, 025101 (2007)

- [31] S. Tavoularis, J.C. Bennett, and S. Corrsin, “Velocity-derivative skewness in nearly isotropic turbulence,” *J. Fluids Mech* **88**, 63 (1994).
- [32] Qian Jian, Skewness Factor of Turbulent Velocity Derivative, *ACTA MECHANICA SINICA*, Vol. 10, No. 1 1994.
- [33] A.K.M.F Hussain, “Coherent Structures - reality and myth.” *Phys. Fluids*. **26**, (10) (1983).
- [34] Stephen. K Robinson, “Coherent Motions in the turbulent boundary layer.” *Annu. Rev. Fluid. Mech.* **23**, 601-39 (1991).
- [35] A. Tsinober, *An Informal Introduction to Turbulence*, Kluwer Academic Publishers, 2001.
- [36] A. Tsinober, M. Ortenberg and L. Shtilman, On depression of nonlinearity in turbulence, *Phys. Fluids* 11 (8) 1999.
- [37] B. Galanti and A. Tsinober, Self-amplification of the field of velocity derivatives in quasi-isotropic turbulence, *Phys. Fluids* 12 (12) 2000.
- [38] B.J. Cantwell, Exact solution of a restricted Euler equation for the velocity, *Phys. Fluids A* 4, 782 (1992).
- [39] T. S. Lund and M. M. Rogers, “An improved measure of strain state probability in turbulent flows” *Phys. Fluids* **6**, 1838 (2002).
- [40] K. Ohkitani and Seigo Kishiba, Nonlocal nature of vortex in an inviscid fluid. *Phys. Fluids* 7, 411-421 (1995).
- [41] T. Gotoh and T. Nakano, Role of Pressure in Turbulence, *Journal of Statistical Physics*, Vol 113, Nos 516 2003.
- [42] K. Ohkitani, Kinematics of vorticity: Vorticity-strain conjugation in incompressible fluid flows, *Physical Review E*, Vol. 50, 6 (1994).

- [43] J. T. Beale, T. Kato and A. Majda, Remarks on the Breakdown of Smooth Solutions for the 3-D Euler Equations, *Commun. Math. Phys.* **94**, 61-66 (1984)
- [44] K. K. Nomura and G. K. Post, “The structure and dynamics of vorticity and rate of strain in incompressible homogeneous turbulence” *J. Fluid Mech.* **377**, 65 (1998).
- [45] A. Ooi, J. Martin, J. Soria, and M. S. Chong, “A study of evolution and characteristics of the invariants of the velocity-gradient tensor in isotropic turbulence” *J. Fluid Mech.* **381**, 141 (1999).
- [46] E. Jeong and S. S. Girimaji, Velocity-Gradient Dynamics in Turbulence: Effect of Viscosity and Forcing, *Theoret. Comput. Fluid Dynamics*(2003) **16**: 421-423.
- [47] J. Martin, A. Ooi, M. S. Chong, and J. Soria, “Dynamics of the velocity gradient tensor invariants in isotropic turbulence” *Phys. Fluids* **10**, 2336 (1998).
- [48] M. S. Chong, J. Soria, A. E. Perry, J. Chacin, B. J. Cantwell and Y. Na, Turbulence structures of wall-bounded shear flows found using DNS data, *J. Fluid, Mech.*, vol. 357 (225-247) 1998.
- [49] Brachet, M.E., Meiron, D.I., Orszag, S.A., Nickel, B.G., Morf, R.H., Frisch, U., 1983. Small-scale structure of the TaylorGreen vortex. *J. Fluid Mech.* **130**, 411-452.
- [50] Herring, J. R., Kerr, R. M., Rotunno, R., 1994: Ertel’s potential vorticity in unstratified turbulence. *Journal of the Atmospheric Sciences*, **51**, 35-47.
- [51] C. Cartes, M. D. Bustamante, M. Brachet, Generalized Eulerian-Lagrangian description of Navier-Stokes dynamics, *Phys. Fluids* **19**, 077101 (2007).
- [52] D. D. Holm and R. M. Kerr Transient Vortex Events in the Initial Value Problem for Turbulence, *Physical Review Letters*, Volume **88**, Number 24, 2002.

- [53] S. Kida and M. Takaoka, Vortex Reconnection, *Annu. Rev. Fluid Mech.* 1994.26: 169-89.
- [54] B. Lüthi, M. Holzner and A. Tsinober, Expanding Q-R space to three dimensions, *J. Fluid Mech.* vol 641, (497-507) 2009.
- [55] D. Visk, F. Hussain and R. M. Kerr, Compressible vortex reconnection, *J. Fluid. Mech* 304, (47-86) 1995.
- [56] Takaki, R. and Hussain, A.K.M.F, Recombination of vortex filaments and its role in aerodynamic noise, 5th Symp on Turbulent Shear Flows, Cornell Univ., USA, 3.19-3.25, August 7-9, 1985.